Non-Equilibrium Relaxation Dynamics in Disordered Superconductors and Semiconductors

Hiba Assi

Dissertation submitted to the Faculty of the
Virginia Polytechnic Institute and State University
in partial fulfillment of the requirements for the degree of

Doctor of Philosophy
in
Physics

Uwe C. Täuber, Chair
James R. Heflin
Michel J. Pleimling
Eric R. Sharpe

March 10, 2016
Blacksburg, Virginia

Keywords: Relaxation Dynamics, Non-Equilibrium Statistical Physics, Magnetic Flux Lines, Glassy Systems, Coulomb Glass

Non-Equilibrium Relaxation Dynamics in Disordered Superconductors and Semiconductors

Hiba Assi

(ABSTRACT)

We investigate the relaxation properties of two distinct systems: magnetic vortex lines in disordered type-II superconductors and charge carriers in the Coulomb glass in disordered semiconductors.

We utilize an elastic line model to simulate magnetic flux lines in disordered type-II superconductors by performing Langevin molecular dynamics simulations. We study the non-equilibrium relaxation properties of flux lines in the presence of uncorrelated point-like disorder or extended linear defects analyzing the effects of rapid changes in the system's temperature or magnetic field on these properties. In a previously-equilibrated system, either the temperature is suddenly changed or the magnetic field is abruptly altered by adding or removing random flux lines to or from the system. One-time observables such as the radius of gyration are measured to characterize steady-state properties, and two-time correlation functions such as the vortex line height autocorrelations are computed to investigate the relaxation dynamics in the aging regime and therefore distinguish the complex relaxation features that result from the different types of disorder in the system. This study allows us to test the sensitivity of the system's non-equilibrium aging kinetics to the selection of initial states and to make closer contact to experimental setups.

Furthermore, we employ Monte Carlo simulations to study the relaxation properties of the two-dimensional Coulomb glass in disordered semiconductors and the two-dimensional Bose glass in type-II superconductors in the presence of extended linear defects. We investigate the effects of adding non-zero random on-site energies from different distributions on the properties of the correlation-induced Coulomb gap in the density of states and on the non-equilibrium aging kinetics highlighted by the autocorrelation functions. We also probe the sensitivity of the system's equilibrium and non-equilibrium relaxation properties to instantaneous changes in the density of charge carriers in the Coulomb glass or flux lines in the Bose glass.

This work was supported by the U.S. Department of Energy, Office of Basic Energy Sciences, Division of Materials Sciences and Engineering, under Grant No. DE-FG02-09ER46613.

I dedicate this work to:
My beloved parents, Mahmoud and Sawsan,
my loving sisters,
and habibi Ali
whose love, encouragement, and prayers helped make this dream come true.

Acknowledgments

I would like to thank my PhD adviser, Prof. Uwe C. Täuber, for his support; invaluable advice; and continuous feedback that have helped me become a better researcher. I have learned immensely from him during my time as a student and I hope to continue to benefit from his extensive knowledge and expertise.

I also thank Prof. Michel Pleimling for his invaluable help during our collaborations and my other committee members Prof. Eric Sharpe and Prof. James Heflin for the advice they contributed towards my progress throughout my time as a graduate student. Thanks to my professors at Virginia Tech and Washington and Lee University from whom I have learned and acquired inspiration and encouragement, especially Prof. John Simonetti, Prof. Irina Mazilu; Prof. Dan Mazilu; and Prof. Thomas Williams.

Loving thanks to Chris Thomas whose memory keeps encouraging me throughout my journey. My gratitude extends to Betty Wilkins for her help in all administrative issues and similarly to Roger Link and Travis Heath for their tireless help with all computing issues and inquiries about the department's excellent computer clusters.

I would like to thank the following people: Dr. Ulrich Dobramysl for the continuous help he has offered me during his time at Virginia Tech and after, Harshwardhan Chaturvedi for his help and collaboration in the many hours we spent at the office, Shadi Esmaeili; Sheng Chen; John Villanova; Dr. Ben Intoy; and Dr. Nasrin Afzal for the exciting discussions and friendships we shared which made Robeson Hall a home away from home.

I would like to acknowledge my friends: Hanan Hasan; Silvia Cheng; Manal Zaher, and others at Virginia Tech who made this journey more enjoyable including Danya Hakky; Marwa Abdel Latif; Navish Wadhwa; Ehab Wahas; Zeid Ayssa.

My deepest gratitude goes to my parents, Mahmoud Assi and Sawsan Mohammad, whose love and guidance have made me the strong woman I am today and who have always encouraged me to pursue my dreams however challenging they appear. Thanks also to my sisters, Tahani; Amani; Alaa; Walaa; and Aya, who I dearly value and from whom I have drawn my strength to pursue this path. I lastly thank my husband Ali for his love and selfless support during my graduate studies and for giving me a warm and loving home.

Contents

Foreword

Given that the world we live in is dominated by non-equilibrium systems, tremendous progress has been made in the area of non-equilibrium statistical mechanics on both the theoretical and experimental fronts. The study of non-equilibrium systems is richer beyond steady states since the dynamics becomes time-dependent and often loses time translation invariance. The slow dynamics and the breaking of time translation invariance are properties of the rich phenomenon of physical aging that emerges in the relaxation of such systems. Physical aging is often utilized to compare various systems by studying the relaxation rates and the aging scaling exponents.

Disordered systems display intriguing equilibrium and out-of-equilibrium relaxation dynamics due to the correlations that are induced by the systems' underlying interactions and interplay between the different energy scales that govern the dynamics. Disorder has a prominent impact on the systems' microscopic properties and it often slows down relaxation allowing for the observation of aging properties. This dissertation addresses two distinct disordered systems: magnetic flux lines in type-II superconductors with different types of pinning defects and charge carriers in the Coulomb glass in doped semiconductors. Numerical studies are performed in both systems to investigate the effects of abrupt changes in experimental parameters on the steady states and non-equilibrium relaxation properties. Therefore, this dissertation is split into two parts:

The first part studies the dynamics of magnetic flux lines in disordered type-II superconductors. Dissipation-free current flow is the most desirable property of these materials in technological applications, which implies that an effective pinning mechanism by spatial disorder is required in these materials. By employing an elastic line model to represent these flux lines and performing extensive Langevin molecular dynamics simulations, we first aim to disentangle the contributions of the vortex-vortex repulsive interactions and pinning to disorder. We furthermore investigate the effects of sudden changes in the system's ambient temperature or magnetic field on the non-equilibrium aging kinetics in the presence of different types of pinning centers.

The second part investigates the Coulomb glass model in doped semiconductors, which consists of interacting charge carriers exposed to pinning defect sites. The interaction-induced correlations produce a soft gap in the density of states and highly influence the system's

non-equilibrium relaxation properties. We analyze the effects of adding random on-site energies from different distributions and of instantaneous changes in the charge carrier density on the relaxation dynamics in the Coulomb glass model in two dimensions.

Magnetic flux lines exposed to columnar disorder in type-II superconductors produce the Bose glass phase due to the lines' localization to these extended linear defects. Therefore, the Coulomb glass model can be adapted to describe the low-temperature properties of flux lines in the Bose glass and monitor the structural rearrangements of these lines, since the earlier study only allowed for monitoring the lines' height fluctuations in the accessible Langevin molecular dynamics simulation time scales.

As described above, this dissertation is divided into two parts. Each part starts with a thorough introduction that provides the theoretical background needed to understand the respective topic. The subsequent chapters describe the corresponding models and simulation algorithms with the utilized sample parameters and measured quantities to later present the results obtained from our extensive studies. Both parts end with detailed conclusions of our investigations and possible directions to pursue in future research.

Part I

Relaxation Properties of Vortex Lines in Type-II Superconductors

Chapter 1

Introduction

The first part of this dissertation addresses the relaxation properties of magnetic vortex lines in type-II superconductors. A deeper understanding of this type of materials is vital, especially due to their wide use in technological and commercial applications. This chapter presents a non-technical introduction on magnetic flux lines and the different types of pinning sites these lines are exposed to which highly influence the lines' relaxation. Furthermore, it discusses the properties of physical aging which is displayed by the relaxation dynamics of magnetic flux lines.

1.1 Type-I vs. Type-II Superconductors

Superconductivity was discovered in 1911 in the lab of H. Kamerlingh Onnes [1], where he observed the complete disappearance of electrical resistance in some materials when cooled below a critical temperature, characteristic of the material. Since this discovery, theoretical and experimental research has been flourishing in the quest of understanding this complex phenomenon. Perfect conductivity is the most desirable effect in superconductors, especially in their applications in high-current transmission lines, for instance. Another characterizing property of superconductors that was observed by Meissner and Ochsenfeld in 1933 is the expulsion of external magnetic fields when the material is cooled to the critical temperature [2]; this is referred to as the *"Meissner state"*.

The presence of the Meissner state implies that there exists a critical magnetic field which destroys superconductivity inside the material [3]. There are two types of superconductors when classified according to the critical magnetic field (see chapter 2). The more widely-known superconductors are type-I superconductors, which are characterized by a single critical magnetic field. Below this critical magnetic field, externally applied magnetic fields are screened by supercurrents and are hence completely expelled from the material's bulk. Type-II superconductors, which were discovered by Lev Shubnikov in 1935 [4, 5], show a

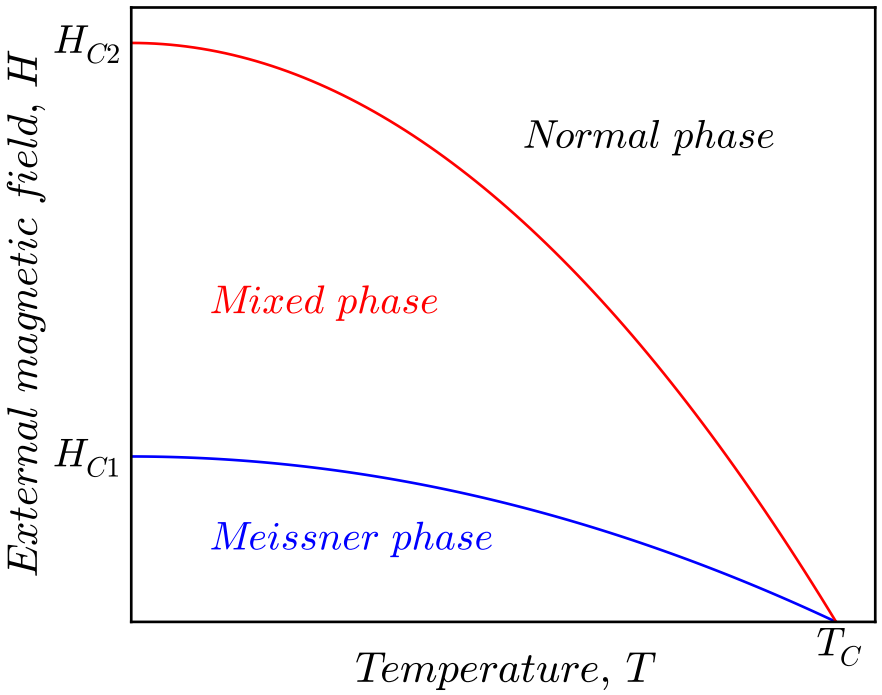

Figure 1.1: Mean-field phase diagram of type-II superconductors. Thermal fluctuations and spatial disorder greatly alter this diagram.

richer and more complex behavior which is displayed in their mean-field phase diagram in Fig. 1.1.

Type-II superconductors are characterized by two critical magnetic fields, as opposed to the single critical magnetic field for type-I superconductors. When the external magnetic field is below the lower critical field H_{C1}, the magnetic field is totally expelled and the material is in the Meissner phase. However, when the field strength is between H_{C1} and an upper critical field H_{C2}, the magnetic field partially penetrates the sample's surface, and a *mixed phase* of normal and superconducting regions is produced in the material's bulk.

When the externally applied magnetic field is between H_{C1} and H_{C2}, it partially penetrates the sample in quantized tubes of flux, called magnetic flux or *vortex* lines. Each vortex line consists of a normal-conducting core that carries one flux quantum $\phi_0 = hc/2e$ of magnetic field, and this core is screened by supercurrents. At the upper critical magnetic field H_{C2}, the cores overlap and the material becomes covered with these normal-conducting cores and superconductivity is lost (more details will be presented in chapter 2).

1.2 Vortex Matter and Pinning Centers

When an electrical current is applied to a type-II superconducting material, each vortex will have a finite velocity as a product of the Lorentz force, which in turn stems from the interplay between the applied current and the magnetic field lines penetrating the vortex core. This will cause the vortices to move through the sample, which induces an electric field and therefore a dissipation in the electrical energy. The most desirable property of these materials is the zero dissipation in the current flow, so one has to prevent vortex motion to eliminate the resulting Ohmic resistance and hence restore the dissipation-free property. Optimal pinning mechanisms are needed to prevent flux flow in the presence of applied currents [6].

Different types of disorder are utilized to prevent flux flow, since these defect sites act as potential wells that attract the normal-conducting vortex cores as a way to decrease loss in condensation energy. The most used pinning sites are those created by uncorrelated point-like disorder and extended linear (columnar) defects. Both types of disorder can be naturally occurring in the sample or artificially introduced by different techniques. Point-like disorder is present in ceramic high-T_C superconductors in the form of oxygen vacancies, or one can synthesize them by exposing the sample to electron irradiation [7] for instance. Similarly, columnar defects can be naturally occurring in the form of line dislocations, or can be artificially introduced by irradiating the material with high-energy ions (such as Sn, Pb, or Iodine) or by simply growing them using MgO nanorods [8] for instance.

In the disorder-free system and at low temperatures, vortices form a hexagonal *Abrikosov* lattice that is characterized by its long-range crystalline order. The presence of weak point defects destroys this order and instead produces a disordered vortex glass phase [9–13] or a Bragg phase state that has a quasi long-range positional order [14–19]. In contrast, the presence of columnar defects results in the emergence of the strongly pinned Bose glass phase [13, 20–23] since vortex lines become attached to the the entire length of these linear pinning sites. Hence, the Bose glass phase is another low-temperature thermodynamic state that emerges due to the presence of disorder, but it is quite distinct from the vortex glass phase. Due to the vortex line localization in the presence of columnar defects, this type of disorder has experimentally proven to be more efficient at pinning than the uncorrelated point-like disorder [24].

Vortex lines are also subject to thermal fluctuations and long-range repulsion: The repulsion between different vortices is a product of the repulsion between the supercurrents that screen the vortices' cores, and thermal fluctuations are due to the thermally induced microscopic currents in the surrounding charge liquid. The vortex line tension; long-range repulsive interactions; thermal fluctuations; and pinning centers have comparable energy scales, and this makes the system of interacting vortex lines a complex and rich system that requires a deep and thorough analysis on the numerical and experimental fronts.

1.3 Experimental Methods

Many experimental techniques have been emerging in the aim of studying vortex matter in type-II superconducting samples. These techniques can be utilized towards a dynamical characterization of material samples and therefore their optimization to be better employed in technological applications. Vasyukov *et al.* used nano-SQUIDs in scanning probe microscopy [25] to image vortices in type-II superconductors, where they recorded magnetic fields down to 50 nT. Auslaender *et al.* utilized the tip of a magnetic force microscope (MFM) on a YBCO sample dragging the end of a single vortex across the sample surface to measure the vortex interaction with a local disorder potential, in the aim to eventually study the dynamics of vortices and their (de)pinning processes in the presence of different defects [26]. Experimental investigation of flux creep parameters in YBCO samples was performed by Abulafia *et al.* using an array of microscopic Hall sensors [27]. Structural properties of vortices in superconductors can be imaged through small-angle neutron scattering [28], a technique that directly measures the Fourier transform of the flux lines' height-height correlation function, and thus the lines' lateral fluctuations can be accessed through this technique.

These methods could perhaps be utilized to probe the relaxation processes of magnetic vortex lines in a disordered medium following quenches in temperature or magnetic field, and to distinguish the effects of different types of disorder on the dynamics of this complex system.

1.4 Physical Aging

When some complex materials undergo relaxation towards thermal equilibrium, they display properties that are characteristic of an important feature called *'physical aging'* [29]. Many glassy systems have been found to undergo physical aging [30] since Struik's careful investigation of this phenomenon in 40 different materials. Struik performed a thorough experimental study on various polymers examining their relaxation properties following some treatment, and he found that aging is a general feature that is similar among all these materials regardless of the specific details of the material. Physical aging happens when the system displays slow relaxation (in algebraic, not exponential time), and time translation invariance of any measured observable is lost. This latter property implies that measured quantities highly depend on the *waiting time* since the preparation of the sample. A more restrictive definition of physical aging requires the material's response function and two-time correlation functions to display *dynamical scaling* [31].

Physical aging has been observed in some experiments involving superconducting materials as well. Du *et al.* observed that the voltage response to an externally applied current in a superconducting 2H-$NbSe_2$ sample depended on the pulse duration, and that was an evidence of the occurrence of physical aging in disordered superconducting materials [32]. Another

occurrence of physical aging was recorded by Papadopoulou *et al.* when they measured the zero field cooled (ZFC) magnetization of $Bi_2Sr_2CaCu_2O_8$ [33] and found aspects of aging in their measurements.

The study of physical aging in vortex matter has also witnessed a flourishing progress on the numerical front as well as on the experimental front. Bustingorry, Cugliandolo, and Domínguez observed aging properties in the two-time correlation functions they measured employing Langevin molecular dynamics simulations of a three-dimensional model of vortex matter [34, 35]. Furthermore, Pleimling and Täuber employed an elastic line model and Monte Carlo simulations to study magnetic flux lines in type-II superconductors analyzing their non-equilibrium relaxation properties, starting from somewhat artificial initial conditions where straight flux lines were randomly placed in the sample [36]. The resulting complex aging features (with identical initial conditions and parameter values) were subsequently confirmed in a very different microscopic representation of the non-equilibrium vortex kinetics through Langevin molecular dynamics [37].

Investigating out-of-equilibrium relaxation properties of magnetic flux lines in type-II superconductors aims to distinguish universal characteristics that do not depend on the sample's parameters from material-specific characteristics. This will assist in material characterization and optimization for technological applications.

1.5 Overview

Chapter 2 provides a theoretical background on superconductivity highlighting Ginzburg-Landau theory, starting with outlining the Ginzburg-Landau equations and the important features that are needed to form a basis for the study of superconductivity. Then, it explains Abrikosov's solution to these equations, and how he found that the arrangement of vortices in a hexagonal lattice constitutes the minimum-energy configuration in a non-disordered system. The last section of this chapter covers the phenomenon of physical aging and dynamical scaling. Chapter 3 gives a brief overview of the course-grained elastic line model and the Langevin molecular dynamics simulation algorithm we employ in our numerical study. Furthermore, it specifies the material parameter values that we use and the quantities that are measured to analyze the system's non-equilibrium and aging properties. The last part of this chapter discusses finite-size effects and verifies that our numerical results are not merely due to the system size we choose.

Chapter 4 and chapter 5 shed light on the relaxation dynamics of vortex matter in disordered type-II superconductors starting from experimentally realizable initial conditions. This allows us to make a closer contact with experimental work and to probe the sensitivity of the non-equilibrium aging kinetics to the choice of initial conditions. Chapter 4 discusses the effects of sudden changes in the system's ambient temperature on the relaxation properties of interacting flux lines in a disordered sample. To characterize the effects of temperature

quenches on the internal fluctuations of magnetic flux lines, we measure the radius of gyration and the corresponding relaxation times in the cases when the system's temperature is kept fixed and when the system's temperature is instantaneously changed. Furthermore, we determine the time evolution of the fraction of pinned line elements in both cases to analyze the different (de)pinning mechanisms that the lines go through. We distinguish the relaxation properties in the presence of point-like disorder and columnar defects, and thereby confirm that each type of disorder yields quite distinct relaxation behavior.

A similar study involving the effects of magnetic field (translated to a vortex density) quenches on the aging kinetics of this complex system is presented in chapter 5, where we compare the effects of sudden increases or decreases in the vortex density to the case when the vortex density remains fixed. This study is accomplished by introducing new measured observables, mainly the two-time height-height autocorrelation function which encapsulates information about the local thermal fluctuations of the present magnetic vortex lines, and the mean-square displacement which gives insight into any global structures evolving in the system. We systematically disentangle the contributions due to repulsive vortex-vortex interactions and pinning to disorder to better understand the contributions of the different competing energy scales. We again find that the non-equilibrium relaxation properties of vortex matter strongly depend on the type of disorder present in the studied sample, and that pinning is made more efficient when combined with the repulsive interactions between different vortices.

Chapter 2

Theoretical Background

This chapter sets the theoretical background on which our numerical work in the next chapters relies. Section 2.1 introduces Ginzburg-Landau theory, which is a phenomenological framework that describes superconductivity. It explains the important features of this theory and the important parameters from which superconductivity stems. Subsequently, section 2.2 first highlights the conditions of classifying superconductors into type-I vs. type-II materials to then explain the emergence of magnetic vortices in type-II superconductors. The last section of this theoretical chapter covers the concept of physical aging and the important properties that will be useful when presenting our work in later chapters.

2.1 Ginzburg-Landau Theory of Superconductivity

The earliest microscopic theory on superconductivity was formulated by John Bardeen, Leon Cooper, and John Robert Schrieffer in 1957 [38, 39]. This theory is referred to as the BCS theory, and it mainly describes superconductivity as the product of the condensation of Cooper pairs into a boson-like state. In 1950, Vitaly Ginzburg and Lev Landau introduced a phenomenological theory that describes superconductivity without assuming any microscopic effects, in contrast with BCS theory. The two theories appeared fundamentally different at first, but Gor'kov in 1957 showed that Ginzburg-Landau theory can be derived as a limit of BCS theory near a critical temperature [40]. Due to the physically desirable macroscopic nature of Ginzburg-Landau theory, we now turn our attention to focus on this theory in the current work.

Ginzburg and Landau [41], building on Landau's theory on second-order phase transitions [42], introduced a complex wavefunction ψ as an order parameter describing the superconducting electrons. They then expressed the material's free energy as a series of powers of ψ and $\nabla\psi$ utilizing some phenomenological parameters as expansion coefficients, where the

free energy F of the material in its superconducting state is defined as

$$F = F_N + \int d^3x \left[\alpha|\psi|^2 + \frac{\beta}{2}|\psi|^4 + \frac{1}{2m}|(-i\hbar\vec{\nabla} - \frac{q}{c}\vec{A})\psi|^2 + \frac{|\vec{B}|^2}{2\mu_0} \right] , \tag{2.1}$$

where F_N is the material's free energy in its normal state, α and β are phenomenological parameters that depend on the system's temperature, $m = 2m_e$ and $q = -2e$ are the effective particle's mass and charge respectively (where m_e is the electron's mass and e is the elementary charge), and $\vec{A}$ is the electromagnetic vector potential that yields the magnetic field $\vec{B} = \vec{\nabla} \times \vec{A}$.

2.1.1 The Ginzburg-Landau Differential Equations

In Ginzburg-Landau theory, one obtains the equation of motion for the order parameter ψ by minimizing the free energy (2.1) with respect to ψ to arrive at the first of the two Ginzburg-Landau differential equations

$$\alpha\psi + \beta|\psi|^2\psi + \frac{1}{2m}(-i\hbar\vec{\nabla} - \frac{q}{c}\vec{A})^2\psi = 0 \ . \tag{2.2}$$

The second Ginzburg-Landau differential equation is obtained by minimizing the free energy (2.1) with respect to the electromagnetic vector potential $\vec{A}$; and the product of this differentiation is the supercurrent density

$$\vec{j} = \frac{q}{m}\Re(\psi^*(-i\hbar\vec{\nabla} - \frac{q}{c}\vec{A})\psi) \ . \tag{2.3}$$

It is worth noting that Equation (2.2), apart from the nonlinear term $\beta|\psi|^2\psi$, has the form of a time-independent Schrödinger equation for a quantum particle in a magnetic field.

2.1.2 Motivation of Superconductivity

The supercurrent density is non-zero only when the order parameter ψ is non-zero, as indicated by (2.3), and therefore the material is superconducting only when ψ is non-zero. In the absence of the electromagnetic field $\vec{A}$ and any gradients in ψ, the free energy in (2.1) becomes

$$F - F_N = \left[\alpha|\psi|^2 + \frac{\beta}{2}|\psi|^4 \right] \cdot V \ , \tag{2.4}$$

where V is the sample's volume, and therefore the free energy becomes a polynomial of order four in the order parameter ψ. If the temperature-dependent parameter β is negative, the

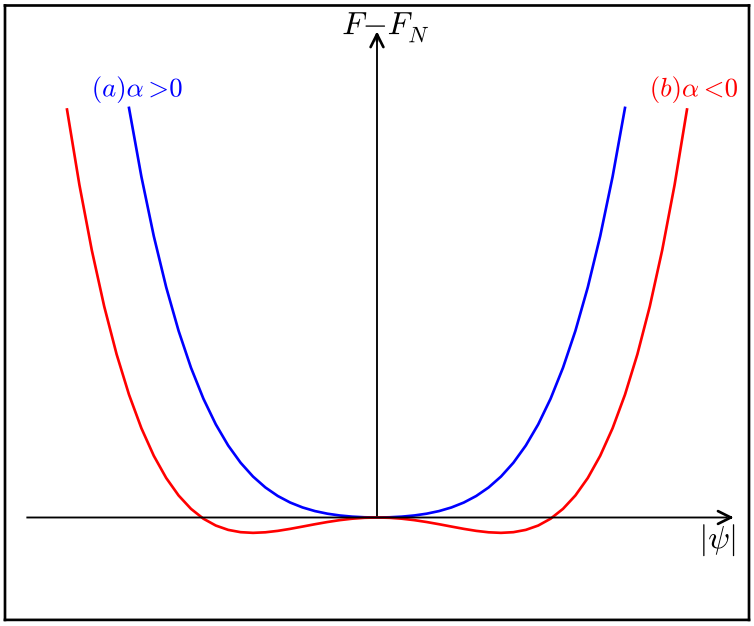

Figure 2.1: Ginzburg-Landau free energy as a function of the order parameter ψ for (a) $\alpha > 0$ and (b) $\alpha < 0$. (b) shows the emergence of two degenerate minima at $|\psi| = |\psi_\infty|$ for the case when $\alpha < 0$.

free energy becomes unbounded from below and the system is then unstable. Therefore, β has to be positive and two cases arise, based on the sign of the other temperature-dependent parameter α, as displayed in Figure 2.1.

As illustrated in figure 2.1, the free energy for $\alpha > 0$ is a parabola with a minimum at $\psi = 0$, which corresponds to the normal state. On the other hand, the free energy takes the shape of a Mexican hat for $\alpha < 0$, with minima at two points satisfying $|\psi|^2 = |\psi_\infty|^2 = -\frac{\alpha}{\beta}$. The notation ψ_∞ is used because the order parameter ψ approaches this value at infinitely deep locations inside the superconductor. Therefore, the order parameter and subsequently the supercurrent density is non-zero only if $\alpha < 0$.

The parameter α is expected to be proportional to $T - T_C$ (with T_C being the system's critical temperature), and hence expanding α in a Taylor series about $T = T_C$ and keeping only the leading term yields

$$\alpha(T) \approx \alpha_C \frac{1}{T_C}(T - T_C) \ . \tag{2.5}$$

Furthermore, when expanding β in a Taylor series around $T = T_C$

$$\beta(T) \approx \sum_{n=0}^{\infty} \beta_n (\frac{T - T_C}{T_C})^n \ , \tag{2.6}$$

it becomes evident that β_0 has to be dominant over all the larger-order terms for the theory to be stable.

Writing the order parameter as $\psi = (-\frac{\alpha}{\beta} + \psi_f)e^{i\theta}$, the kinetic term in the free energy (2.1) picks up a term that is simply

$$-\frac{q^2}{2mc^2}\frac{\alpha}{\beta}|\vec{A}|^2 \ . \tag{2.7}$$

This term is made of constant pre-factors to the electromagnetic field $\vec{A}$, and is therefore considered to be an effective mass that the photon acquires. This feature is analogous to the effective mass that the Higgs field acquires in the *Anderson-Higgs* mechanism in high-energy physics.

2.1.3 London Penetration Depth and Coherence Length

Writing the order parameter as $\psi = |\psi|e^{i\theta}$, the third term of the integrand in the free energy (2.1) becomes

$$\frac{1}{2m}\left[\hbar^2(\vec{\nabla}|\psi|)^2 + (\hbar\vec{\nabla}\theta - \frac{q}{c}\vec{A})^2|\psi|^2\right] \ . \tag{2.8}$$

The first term in (2.8) gives the gradient in the magnitude of the order parameter ψ, and the second term yields the kinetic energy associated with ψ and the formed supercurrents. The phase angle θ, assuming a London gauge, is constant, and the second term in (2.8) hence becomes $q^2A^2|\psi|^2/2mc^2$, which is exactly the effective mass term obtained in (2.7). The kinetic energy density for a superconductor stemming from London's equations is

$$\frac{n_s}{2}mv_s^2 = \frac{A^2}{8\pi\lambda_{eff}^2} \ , \tag{2.9}$$

where $n_s = |\psi|^2$ is the local density of superconducting electrons, and $\vec{v}_s = -\frac{q\vec{A}}{mc}$ is the local average velocity in the presence of an applied field. Equating the effective mass term we obtained with the right-hand side of (2.9) results in the London penetration depth

$$\lambda = \sqrt{\frac{mc^2}{4\pi q^2|\psi|^2}} \ . \tag{2.10}$$

The London penetration depth is the characteristic length scale that describes the decay of the external magnetic field inside a superconducting material.

The second characteristic length that is needed to fully describe superconductivity is the coherence length, which can be obtained when magnetic fields are absent, *i.e.* $\vec{A} = 0$. In this case, (2.2) becomes

$$\psi + \frac{\beta}{\alpha}|\psi|^2\psi - \frac{\hbar^2}{2m\alpha}\vec{\nabla}^2\psi = 0 \tag{2.11}$$

and the coherence length is defined as the pre-factor in the third term of (2.11)

$$\xi = \sqrt{\frac{\hbar^2}{2m|\alpha(t)|}} \ . \tag{2.12}$$

The coherence length ξ defines the characteristic length scale for the variations in the order parameter ψ, and it corresponds to the size of one Cooper pair in the BCS theory.

2.2 Type-II Superconductors

2.2.1 The Ginzburg-Landau Parameter

It is now important to introduce the dimensionless Ginzburg-Landau parameter κ, which is defined as the ratio of the London penetration length λ (2.10) and the coherence length ξ (2.12)

$$\kappa = \lambda/\xi \ . \tag{2.13}$$

Superconductors are classified according to their Ginzburg-Landau parameter into type-I and type-II superconductors. When $\kappa < 1/\sqrt{2}$, the material is a type-I superconductor and is characterized by a first-order phase transition at the critical temperature, where superconductivity is completely lost above the critical field H_C.

On the other hand, type-II superconductors have $\kappa > 1/\sqrt{2}$ and exhibit a smooth transition from the superconducting state to the normal state for magnetic fields greater than the lower critical field H_{C1}. Furthermore, there is a negative surface energy associated with the creation of phase boundaries if $\kappa > 1/\sqrt{2}$, and hence free energy gain is obtained by creating normal-conducting regions inside the superconducting phase. Therefore, a mixed phase is produced and is sustained with magnetic fields above H_{C1} and below the upper critical field $H_{C2} = \sqrt{2}\kappa H_C$, at which point the normal-conducting regions overlap and superconductivity is completely lost.

2.2.2 Vortices in Type-II Superconductors

The free energy has terms that are dependent on the order parameter

$$F = \int d^3x \left[|\psi|^2(\alpha + \frac{\beta}{2}|\psi|^2) + \frac{1}{2m}|(-i\hbar\vec{\nabla} - \frac{q}{c}\vec{A})\psi|^2 \right] . \tag{2.14}$$

The first term of (2.14) is finite only with the requirement that

$$|\psi(r \to \infty)|^2 = -\frac{\alpha}{\beta} \equiv \rho^2 . \tag{2.15}$$

The condition displayed in (2.15) requires the magnitude of the order parameter at infinity to be fixed, and not its phase. This allows us to form an ansatz on the definition of the order parameter

$$\psi = \rho e^{i\theta} , \tag{2.16}$$

where $\rho \equiv |\psi|$ and θ is the phase of the order parameter at $r \to \infty$.

Outside the vortex core where the magnetic field lines are screened by supercurrents, the electromagnetic field $\vec{A} = 0$. Hence, the current density (2.3) in this limit becomes

$$\vec{j} = -\frac{q}{m}\Re(\psi^* i\hbar\vec{\nabla}\psi) \equiv \frac{2qh}{m}\frac{\rho^2}{r}\hat{e}_\theta . \tag{2.17}$$

This implies that supercurrents run only in the azimuthal direction, *i.e.* they rotate at $r \to \infty$. This rotation of the current at infinity is the theoretical motivation for the formation of vortices in type-II superconductors.

2.2.3 Fluxoid Quantization

The magnetic flux in a superconductor in the presence of an externally applied magnetic field is computed by

$$\Phi = \int \vec{B} \cdot d\vec{f} = \oint \vec{A} \cdot d\vec{s} . \tag{2.18}$$

Defining the supercurrent velocity as $m\vec{v}_s = \hbar\vec{\nabla}\theta - \frac{q}{c}\vec{A}$, (2.18) becomes

$$\Phi = \frac{\hbar c}{q}\oint \vec{\nabla}\theta \cdot d\vec{s} - \frac{mc}{q}\oint \vec{v}_s \cdot d\vec{s} . \tag{2.19}$$

Fritz London introduced the concept of a *fluxoid quantum* to denote the magnetic field associated with each normal region in the superconducting background [43]. A fluxoid is defined as

$$\Phi' = \Phi + \frac{mc}{q}\oint \vec{v}_s \cdot d\vec{s} = \frac{c}{q}\oint (m\vec{v}_s + \frac{q}{c}\vec{A}) \cdot d\vec{s} = \frac{\hbar c}{q}\oint \vec{\nabla}\theta \cdot d\vec{s} = k\frac{hc}{q} \ . \tag{2.20}$$

The last expression is obtained by noting that the integral in the first term in (2.19) is equal to $2\pi k$, where k is an integer. Noting that $|q| = 2e$ is the charge of one Cooper pair, the fluxoid quantum has the value

$$\Phi_0 = \frac{hc}{2e} = 2.07 \times 10^{-15} Wb \ . \tag{2.21}$$

One magnetic flux quantum Φ_0 is the magnetic field value that is contained in the normal-conducting core of one vortex.

2.2.4 The Abrikosov Vortex State

In 1957, Alexei Abrikosov introduced an approximate solution to the Ginzburg-Landau equations (2.2) and (2.3) [44]. His solution is valid for magnetic fields near the upper critical field H_{C2}, where the order parameter $|\psi|^2 << 1$. Ignoring the nonlinear term $|\psi|^2\psi$ in (2.2) and by minimizing the free energy, the linearized Ginzburg-Landau equations have solutions of the form

$$\psi_k = e^{iky} f(x) = exp\left[iky - \frac{(x - x_k)^2}{2\xi^2}\right] \ , \tag{2.22}$$

with k (a free parameter) denoting k_y and $x_k = k\Phi_0/2\pi H$.

We enforce a crystalline arrangement of the vortices since this will have lower energy than a random arrangement of vortices. To apply this restriction, k is required to be $k_n = nq$ producing a periodicity in the y direction of $\Delta y = 2\pi/q$. This also ensures periodicity in the location of the vortex cores at $x_n = nq\Phi_0/2\pi H$ of $\Delta x = q\Phi_0/2\pi H = \Phi_0/H\Delta y$.

From the periodicities in the x and y directions above, one can conclude that

$$H\Delta x\Delta y = \Phi_0 \tag{2.23}$$

is the magnetic flux quantum carried by each unit cell of the vortex lattice.

Therefore, a more general solution to the linearized Ginzburg-Landau equation is

$$\psi_L = \sum_n C_n e^{inqy} e^{-\frac{(x-x_k)^2}{2\xi^2}} \ , \tag{2.24}$$

where k is restricted here to be integer multiples of q, and this solution is periodic in y. Furthermore, (2.24) is periodic in x if the pre-factors C_n are chosen to be periodic in n. A triangular lattice is obtained when $C_{n+2} = C_n$ and $C_1 = iC_0$.

It is worth noting that the relative favorability of the various possible solutions is determined by the parameter

$$\beta_A = \frac{\langle \psi_L^4 \rangle}{\langle \psi_L^2 \rangle^2} \ , \tag{2.25}$$

which is the nonlinear contribution to the Ginzburg-Landau free energy. Abrikosov showed that the lower β_A is, the more favorable the corresponding solution is. Numerical calculations show that $\beta_A = 1.16$ for a triangular lattice [45]. It is worth noting that Abrikosov in his paper proved that a square lattice is the array that yields the lowest value of $\beta_A = 1.18$. Kleiner *et al.* [45] later corrected this by proving that the triangular array of vortices has the most favorable value of β_A among all solutions.

Another way to decide the favorability of the different solutions of the Ginzburg-Landau equation is by determining the separation a of the nearest neighboring vortices [3]. The presence of mutual vortex-vortex repulsive interactions implies that the lattice with the largest a is the most optimal configuration. The nearest neighbor distance in the triangular array, which is the arrangement when each vortex is surrounded by a hexagonal array of other vortices, is

$$a_\triangle = \left(\frac{4}{3}\right)^{1/4} \left(\frac{\Phi_0}{B}\right)^{1/2} = 1.075 \left(\frac{\Phi_0}{B}\right)^{1/2} \ . \tag{2.26}$$

In contrast, the distance between the four neighbors in the square array, favored by Abrikosov, is

$$a_\square = \left(\frac{\Phi_0}{B}\right)^{1/2} \ . \tag{2.27}$$

Therefore, $a_\triangle > a_\square$ which implies that the triangular array is more favored than the square array based on this simple argument. It is worth noting that experiments confirmed the triangular array [46–48] validating this theoretical analysis.

2.2.5 Vortex Line Energy

The vortex line tension is the line's free energy per unit length, ϵ_1, and it can be obtained by adding the contributions of the magnetic field energy and the kinetic energy

$$\epsilon_1 = \frac{1}{8\pi}\int\left[\vec{B}^2 + \lambda^2(\vec{\nabla}\times\vec{B})^2\right]df \ , \tag{2.28}$$

where the first term in (2.28) is due to the magnetic field energy and the second term is due to the kinetic energy $n_s\int\frac{m}{2}\vec{v}_s^2 df = \frac{m}{2n_sq^2}\int\vec{j}_s^2 df$.

Integrating (2.28) by parts gives

$$\epsilon_1 = \left(\frac{\Phi_0}{4\pi\lambda}\right)^2 K_0\left(\frac{\xi}{\lambda}\right) \ , \tag{2.29}$$

where $K_0(x)$ is the zeroth-order modified Bessel function.

Another way to express ϵ_1 is

$$\epsilon_1 \approx \left(\frac{\Phi_0}{4\pi\lambda}\right)^2 \ln\kappa \ , \tag{2.30}$$

since the zeroth-order modified Bessel function in (2.29) is logarithmic at short distances.

2.2.6 Vortex Line Interaction

To find the interaction energy between two vortices, we employ the concept of superposition between magnetic fields, with their cores being at positions $\vec{r}_1$ and $\vec{r}_2$

$$\vec{B}(\vec{r}) = \vec{B}_1(\vec{r}) + \vec{B}_2(\vec{r}) = \vec{B}(|\vec{r}-\vec{r}_1|) + \vec{B}(|\vec{r}-\vec{r}_2|) \ . \tag{2.31}$$

This causes an increase in the free energy, and the total increase per unit length is written as

$$\begin{aligned}\Delta F &= \frac{\Phi_0}{8\pi}\Big[B_1(\vec{r}_1) + B_1(\vec{r}_2) + B_2(\vec{r}_1) + B_2(\vec{r}_2)\Big] \\ &= \frac{\Phi_0}{8\pi}\Big[2B(0) + 2B(|\vec{r}_1-\vec{r}_2|)\Big] \\ &= 2\epsilon_1 + \frac{\Phi_0}{4\pi}B(|\vec{r}_1-\vec{r}_2|) \ .\end{aligned} \tag{2.32}$$

The second term of the third result in (2.32) yields the interaction energy $F_{12} = V(r)$, after the substitution of $B(r) = \frac{\Phi_0}{2\pi\lambda^2} K_0(\frac{r}{\lambda})$

$$V(r) = 2\left(\frac{\Phi_0}{4\pi\lambda}\right)^2 K_0\left(\frac{r}{\lambda}\right) . \tag{2.33}$$

If we introduce a new energy scale $\epsilon_0 = (\frac{\Phi_0}{4\pi\lambda})^2$, then the final representation of the vortex-vortex interaction is

$$V(r) = 2\epsilon_0 K_0\left(\frac{r}{\lambda}\right) . \tag{2.34}$$

The zeroth-order modified Bessel function is logarithmic at short distances and falls off as $r^{-1/2}e^{-r/\lambda}$ at large distances, and therefore the vortex-vortex interaction in (2.34) is essentially a logarithmic repulsive interaction that is exponentially screened at λ.

2.2.7 Vortex Motion

It is worth noting that the repulsive vortex-vortex interactions as well as any external currents produce a Lorentz force that acts on one vortex as

$$\vec{F} = \vec{j} \times \frac{\Phi_0}{c}\hat{e}_z , \tag{2.35}$$

where $\vec{j}$ is the total supercurrent density due to all the other vortices in the system.

The Lorentz force causes vortices to move within the sample at velocity $\vec{v}$ transverse to the current. This flux flow induces an electric field $\vec{E} = \vec{B} \times \frac{\vec{v}}{c}$, parallel to the direction of the driving current $\vec{J}$. The induced electric field acts as a resistive voltage, and therefore electric power is dissipated. In short, the motion of the normal-conducting cores in the superconducting region produces a dissipative force $\vec{F}_f = -\eta\vec{v}$, with η being the viscous drag coefficient. The rate of energy dissipation per unit length of a vortex is

$$W = -\vec{F}_f \cdot \vec{v} = \eta v^2 . \tag{2.36}$$

2.2.8 Flux Pinning

The goal in technological applications of type-II superconductors is to produce materials that carry high electric currents in the presence of strong magnetic fields without the dissipation of electric energy. To achieve this, flux flow should be minimized by pinning vortices to

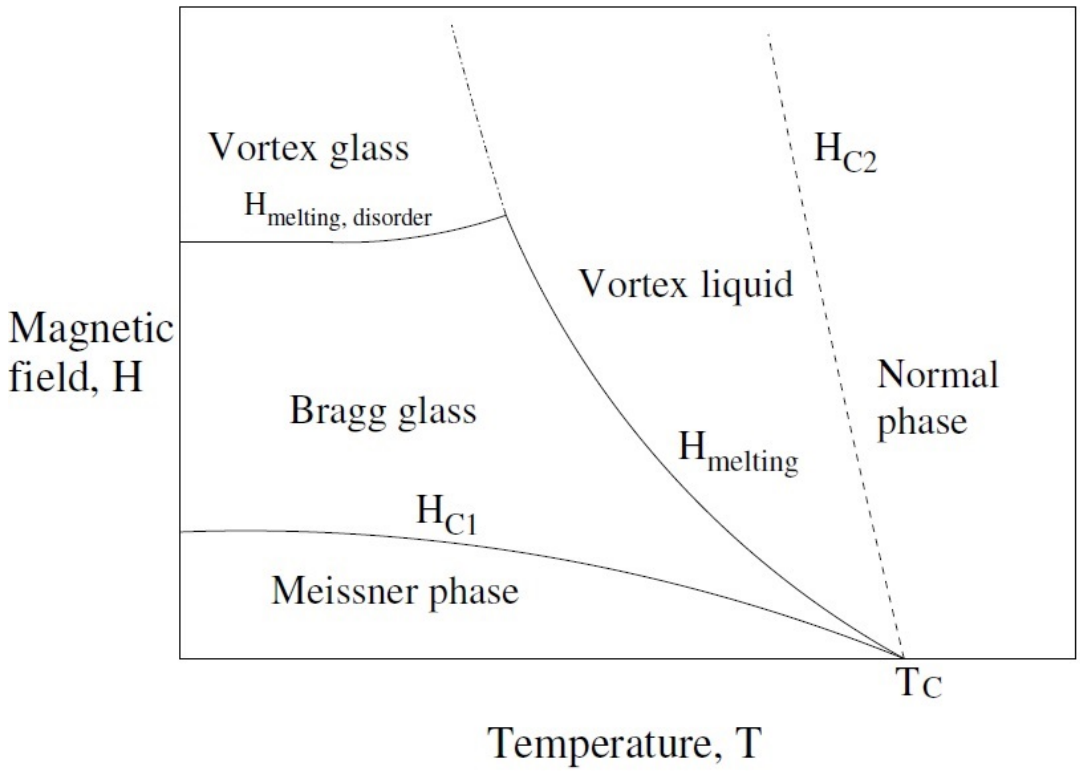

Figure 2.2: The phase diagram for type-II superconductors in the presence of point disorder [49]

defect sites. Defect sites locally suppress the density of superconducting charge carriers, so having the normal-conducting vortex cores at the defect sites minimizes the energy loss. Therefore, defect sites attract vortex cores and thereby localize vortices. The condensation energy density of Cooper pairs is $-\alpha^2/2\beta$ (obtained from the mean-field theory outlined in the sections above), and therefore the pinning energy has to be of the order $-V\alpha^2/2\beta$ for the defect sites to be effective at pinning the cores, where V is the volume of the overlap region between a vortex core and a pinning defect site.

There are different types of pinning centers that can either be naturally occurring in the sample or artificially introduced. The presence of any type of disorder highly alters the phase diagrams of type-II superconductors from the mean-field approximation that was displayed in Figure 1.1. Larkin and Ovchinnikov [50] showed that the presence of even a weak density of pinning centers destroys the long-range crystalline order of the low-temperature Abrikosov flux line lattice. The presence of weak point pinning centers destroys the crystalline order to form either a genuine disordered vortex glass phase [9–13] or a Bragg glass state that is characterized by quasi long-range positional order [14–19]. Large thermal fluctuations (of the order of the lattice constant a_0) have to be taken into account since they cause a melting transition from the vortex lattice to produce a vortex liquid phase [51, 52]. Furthermore, at small current densities, thermal fluctuations cause vortex lines to move due to the thermally-

induced jumps over pinning barriers; a phenomenon referred to as *flux creep* in type-II superconductors. In the presence of strong disorder, the thermally induced first-order melting transition of the vortex lattice at elevated temperatures [51, 53, 54] is thereby replaced by a disorder-driven continuous phase transition between frustrated ('glassy') low-temperature states and a fluctuating flux liquid phase.

The mean-field phase diagrams are therefore highly modified by the presence of point-like disorder and thermal fluctuations, as can be seen in Figure 2.2. This confirms the complexity of the system of vortex matter by highlighting the different thermodynamic phases that emerge due to flux pinning to these defect sites and thermal fluctuations.

In contrast with point-like disorder, the presence of correlated columnar defects results in the emergence of a novel low-temperature thermodynamic state distinct from the vortex glass phase, namely the strongly pinned Bose glass [13, 20–23]. Since vortex lines become then localized along the entire length of these linear pinning centers, the sample's tilt modulus diverges (transverse Meissner effect) [23, 55]. Indeed, columnar defects have experimentally proven more efficient at pinning than uncorrelated point-like disorder due to their extended nature [24].

2.3 Physical Aging

Aging refers to the change of an object's properties with time, even in the absence of any forces acting on the material. In our current work, we investigate *'physical aging'* which focuses on the relaxation of some complex materials towards thermal equilibrium. The first experimental work that carefully studied this phenomenon was performed by Struik [29].

Struik utilized glass-forming systems, PVC for instance, to study the relaxation dynamics of such materials towards equilibrium. He quenched the glass-forming PVC from the liquid phase (the system was prepared at a high-temperature) into the glassy phase (that occurs at a low-temperature where many equilibrium states exist) and far from equilibrium [31]. The system is forced to be far from equilibrium when the change in temperature rapidly occurs. He waited for certain *waiting time* s and then applied mechanical stress to eventually measure the system's linear response to this stress. He furthermore repeated the same experiment with different values of the waiting time and considered the resulting non-equilibrium relaxation dynamics. Struik observed a very *slow* change in the material's properties and that the response function was dependent on the values of s.

The response function depending on both the measurement time t and waiting time s means that *time translation invariance* is broken. Time translation invariance implies that when plotting the individual curves of the response function pertaining to each s against $t - s$, all the curves collapse onto a master curve.

After observing the absence of time translation invariance, Struik showed that the different

relaxation curves can be superimposed onto a master curve upon scaling them with respect to the waiting time s and equivalently shifting them along the time axis. This is referred to as *'dynamical scaling'*, a third property that characterizes the phenomenon of physical aging. To understand this further, lets consider the *two-time correlation function*

$$C(t,s;\mathbf{r}) = \langle \phi(\mathrm{t},\mathbf{r})\phi(\mathrm{s},\mathbf{0})\rangle - \langle \phi(\mathrm{t},\mathbf{r})\rangle \langle \phi(\mathrm{s},\mathbf{0})\rangle \ , \tag{2.37}$$

where $\phi(t,\mathbf{r})$ is the order parameter at time t and position $\mathbf{r}$, and $t \geq s$ are the two times since the quench. Furthermore, the *autocorrelation function* defined as

$$C(t,s) \equiv C(t,s;\mathbf{0}) \tag{2.38}$$

can be split into a stationary and an aging part [31]

$$C(t,s) = C_{st}(t,s) + C_{age}(t,s) \ , \tag{2.39}$$

with the stationary part satisfying $\lim_{\mathrm{t}\to\infty} \mathrm{C_{st}}(\mathrm{t},\mathrm{s}) = 0$. Furthermore, the aging part in (2.39) can be expressed in the scaling form [31]

$$C_{age}(t,s) = F_C\left(\frac{h(t)}{h(s)}\right) \ . \tag{2.40}$$

The time-reparametrization function $h(t)$ in the scaling function F_C in (2.40) is of the form [31]

$$h(t) = h_0 \exp\left[\frac{1}{A}\frac{t^{1-\mu}-1}{1-\mu}\right] \ , \tag{2.41}$$

where h_0 and A are constants, and μ is a free parameter. The aging part in (2.39) has been shown by experimental analysis of glassy systems to be expressed as

$$C_{age}(t,s) \approx F_C\left(\frac{t}{s^{\mu}}\right) \ . \tag{2.42}$$

The aging scaling exponent μ in (2.42) can be utilized to classify three types of aging behavior: subaging when $0 < \mu < 1$, *full aging* or *simple aging* when $\mu = 1$, and superaging when $\mu > 1$.

Our current focuses on full aging, characterized by $\mu = 1$, to describe purely relaxational dynamics. In this case, the autocorrelation function $C(t,s)$ follows the scaling form

$$C(t,s) = s^b f_C(t/s) \ , \tag{2.43}$$

where b is an aging scaling exponent. It is important to note that when $t/s \to \infty$ in the case of simple aging, the scaling function f_C is a power law

$$f_C(t/s) \sim (t/s)^{-\lambda_C/z}, \tag{2.44}$$

where λ_C is an autocorrelation exponent, z is a dynamic exponent, and the ratio λ_C/z is an independent scaling exponent that one has to investigate.

To summarize this section, physical aging is a phenomenon that a physical system undergoes when the relaxation process towards its stationary state(s) is characterized by a slow (non-exponential) dynamics, shows breaking of time translation invariance, and displays dynamical scaling. The properties of physical aging of magnetic flux lines in type-II superconductors will be studied in chapter 5, while those of charge carriers in the Coulomb glass in disordered semiconductors will be presented in chapters 10 and 11.

Chapter 3

Model and Simulation Description

This chapter was adapted with only minor changes from our publication:

H. Assi, H. Chaturvedi, U. Dobramysl, M. Pleimling, U. C. Täuber, "Relaxation dynamics of vortex lines in disordered type-II superconductors following magnetic field and temperature quenches", Phys. Rev. E (2015) 92, 052124. "Copyright (2015) by the American Physical Society."

3.1 Elastic Line Model

In our numerical study of magnetic vortex lines in type-II superconductors, we assume that the system is in the extreme London limit. This limit is approached when the London penetration depth λ is much greater than the coherence length ξ, and thus the Ginzburg-Landau parameter $\kappa >> 1/\sqrt{2}$. This limit means that the vortex cores are of negligible thickness and the vortex lines can be considered as elastic lines of infinitesimal thickness.

3.1.1 Effective Model Hamiltonian

We consider systems of N vortex lines in the London limit, and we hence employ a three-dimensional elastic line description [23, 56]. We describe vortices through their trajectories $\vec{r}_i(z)$, where $\vec{r}_i$ is the x, y position of line i or the position in the crystallographic ab plane, and z is the direction of the externally-applied magnetic field or the crystallographic c direction.

High-T_C superconducting materials are highly-anisotropic: The effective charge carrier masses M_{ab} and M_c, in the ab plane and c direction respectively, are different. The anisotropy parameter $\Gamma^{-1} = M_{ab}/M_c$ is the effective mass ratio.

The system's Hamiltonian is then written as a functional of the N interacting trajectories

$$H\left[\vec{r}_i\right] = \sum_{i=1}^{N} \int_0^L dz \left[\frac{\tilde{\epsilon}_1}{2} \left| \frac{d\vec{r}_i(z)}{dz} \right|^2 + U_D(\vec{r}_i(z), z) + \frac{1}{2} \sum_{j \neq i}^{N} V(|\vec{r}_i(z) - \vec{r}_j(z)|) \right], \tag{3.1}$$

where L is the system's length along the z direction. The system's free energy (3.1) consists of three competing energy terms: the elastic vortex line tension, an attractive potential describing the N_D disordered pinning sites, and the vortex-vortex repulsive interactions.

The elastic line stiffness or local tilt modulus is given by $\tilde{\epsilon}_1 \approx \Gamma^{-2}\epsilon_0 \ln(\lambda_{ab}/\xi_{ab})$, where λ_{ab} and ξ_{ab} respectively denote the London penetration depth and the coherence length in the ab crystallographic plane. Moreover, the in-plane vortex-vortex repulsive interactions are given by $V(r) = 2\epsilon_0 K_0(r/\lambda_{ab})$, with K_0 denoting the zeroth-order modified Bessel function, which essentially represents a logarithmic repulsion that is exponentially screened at the scale λ_{ab}.

We model the N_D point-like pinning centers as spatially randomly-distributed smooth potential wells of the form

$$U_D(\vec{r}, z) = -\sum_{\alpha=1}^{N_D} \frac{b_0}{2}\, p\delta(z - z_\alpha) \left[1 - \tanh\left(5 \frac{|\vec{r} - \vec{r}_\alpha| - b_0}{b_0} \right) \right], \tag{3.2}$$

where $p \geq 0$ represents the pinning potential strength, $\vec{r}_\alpha$ and z_α respectively denote the in-plane and z coordinates of pinning center α since we discretize the Hamiltonian (3.1) in the z direction.

On the other hand, extended columnar defects are set up by first randomly selecting the in-plane coordinates $\vec{r}_\alpha$, and then placing identical potential wells (3.2) at all z positions z_α. Henceforth, all lengths are measured relative to the pinning potential width b_0, and energies are measured in units of $\epsilon_0 b_0$ with $\epsilon_0 = (\phi_0/4\pi\lambda_{ab})^2$, where $\phi_0 = hc/2e$ is the magnetic flux quantum.

3.1.2 Langevin Molecular Dynamics

We employ a Langevin molecular dynamics algorithm to analyze the vortex kinetics. As mentioned above, we discretize the system into layers in the z direction, which is the direction of the external magnetic field. The spacing between these layers corresponds to the unit cell size c_0 along the crystal's c direction [56, 57]. The effective forces acting on vortex lines vertices are then computed as spatial derivatives of the discretized version of the Hamiltonian (3.1).

Correspondingly, we numerically solve the coupled overdamped Langevin equations by direct temporal integration [58] of

$$\eta \frac{\partial \vec{r}_i(t,z)}{\partial t} = -\frac{\delta H[\vec{r}_i(t,z)]}{\delta \vec{r}_i(t,z)} + \vec{f}_i(t,z)\,, \tag{3.3}$$

where η is the Bardeen-Stephen viscous drag parameter $\eta = \phi_0^2/2\pi\rho_n c^2 \xi_{ab}^2$ [59].

The fast microscopic degrees of freedom of the surrounding medium (*e.g.*, phonons) are captured by thermal stochastic forces, modeled as uncorrelated Gaussian white noise with a vanishing mean $\left\langle \vec{f}_i(t,z) \right\rangle = 0$. We impose the Einstein relation

$$\left\langle \vec{f}_i(t,z) \vec{f}_j(s,z') \right\rangle = 2\eta\, k_{\mathrm{B}} T\, \delta_{ij} \delta(t-s) \delta(z-z') \tag{3.4}$$

to guarantee that the system asymptotically relaxes to thermal equilibrium with a canonical probability distribution $\propto e^{-H/k_{\mathrm{B}}T}$ in the absence of any external driving current.

The flux lines are moving in a three-dimensional space with periodic boundary conditions in the xy plane and free boundary conditions in the z direction. We set the system size to $(16/\sqrt{3})\lambda_{ab} \times 8\lambda_{ab}$, since this aspect ratio ensures that the system of flux lines equilibrates to form a hexagonal Abrikosov lattice in the absence of disorder and driving currents.

3.2 Simulation Description

3.2.1 Material Parameters

We select our material parameters to closely simulate the actual values for the ceramic high-T_C type-II superconducting compound $YBa_2Cu_3O_7$ (YBCO), which is characterized by a critical temperature of about 90 K. All simulation lengths are measured in units of the pinning center radius, which we set to $b_0 = 35\mathring{A}$. The spacing between layers in the c direction is set equal to this basic scale $c_0 = b_0$. Furthermore, the in-plane London penetration depth and the superconducting coherence length are $\lambda_{ab} = 34 b_0 \approx 1200\mathring{A}$ and $\xi_{ab} = 0.3 b_0 \approx 10.5\mathring{A}$, respectively. This emulates the high anisotropy of YBCO, with an effective mass ratio $\Gamma^{-1} = 1/5$.

Furthermore, all simulation energies are measured in units of $\epsilon_0 b_0$, where ϵ_0 is the line energy per unit length: $\epsilon_0 \approx 1.92 \cdot 10^{-6}\,\mathrm{erg\,/\,cm}$. The vortex line tension energy scale is then $\tilde{\epsilon}_1/\epsilon_0 \approx 0.189$. The depth of the pinning potential wells is fixed at $p/\epsilon_0 = 0.05$. We perform all our simulation runs at temperatures $T = 10 \ldots 40\,\mathrm{K}$, where $T = 10\,\mathrm{K}$ corresponds to $k_{\mathrm{B}}T/\epsilon_0 b_0 = 0.002$ in our simulation units. This range of temperatures is chosen so that the system stays at an ambient temperature much below the critical temperature of

YBCO. Finally, we set the Bardeen-Stephen viscous drag coefficient $\eta = \phi_0^2/2\pi\rho_n c^2\xi_{ab}^2 \approx 10^{-10}\,\mathrm{erg}\cdot\mathrm{s}\,/\,\mathrm{cm}^2$ to one (for the normal-state resistivity of YBCO near T_c, $\rho_n \approx 500\,\mu\Omega\,\mathrm{cm}$, see Table 1 in Ref. [60]). The simulation time steps are fixed by the fundamental temporal unit $t_0 = \eta b_0/\epsilon_0 \approx 18\,\mathrm{ps}$ and all times in our simulations are measured in units of t_0.

We consider systems composed of between $N = 10$ and $N = 21$ vortices, with each vortex associated with one magnetic flux quantum $\phi_0 = hc/2e = 2.07 \times 10^{-15}\,\mathrm{Wb}$. Throughout our analysis, the number of layers is $L = 640$, with each layer representing a unit cell of the YBCO crystal, and the number of pinning sites per layer is fixed at $N_D/L = 1710$.

3.2.2 Simulation Protocol

Earlier work by our research group focused on studying the non-equilibrium relaxation dynamics of magnetic flux lines starting from random initial conditions [36, 37]. The aim of our work presented here was to impose more experimentally realizable initial conditions, compare the results of this new addition to our earlier results, and to bridge theoretical and experimental work. To accomplish this, we investigated the effects of sudden changes in the system's ambient temperature or the magnitude of the externally-applied magnetic field. In both cases, we start with N straight flux lines located at random positions in the sample, and let them relax up to a long time beyond any microscopic time scale τ_{mic} to ensure that they reached some steady state.

A magnetic field quench is implemented in our simulations by adding flux lines at random positions in the system (up-quench) or removing randomly selected vortices from the system (down-quench). We start with straight flux lines positioned at random in the sample, and let the system relax up to an initial relaxation time $r = 10^5$. We then instantaneously increase the magnetic field by adding 5 straight flux lines to the 16 originally present and essentially relaxed vortices; or instantaneously decrease the field by removing 5 random lines from 21 relaxed initial vortices. Subsequently, we let the resulting system relax up to a waiting time s, at which a snapshot of the system is taken; the waiting time s is measured after the quench. The system's ambient temperature is fixed at $T = 0.002$ for this part. A time-line of this protocol is drawn below:

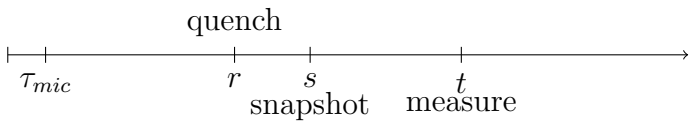

At later times $t > s$, different two-time correlation functions are evaluated. Since r is much larger than the different waiting times s and measurement time t, it is crucial to take this elapsed time period into account when considering the initial lines that have relaxed for a duration r. We therefore introduce the times $\sigma = r + s$ and $\Gamma = r + t$.

When the external magnetic field is altered in experimental samples, flux lines enter or leave the sample from its boundaries. Since our numerical study is limited to a fairly small number of vortices, introducing physical surfaces through the removal of our implemented periodic boundary conditions would render our system dominated by the ensuing boundary effects. We rather consider our simulation domain as a representative sample of the bulk region in a much larger physical system. Also, the formation or deletion of vortices from the sample's boundaries occurs on time scales much faster than considered in this study of comparatively slow relaxation kinetics.

Temperature quenches are accomplished by letting the initial configuration of $N = 16$ flux lines relax up to a similar initial relaxation time ($t = 10^5$) at which the temperature is suddenly raised from 0.002 to 0.008 or lowered from 0.008 to 0.002. Throughout our analysis of magnetic field and temperature quenches, the number of layers is $L = 640$ and the number of pinning sites per layer is fixed at $N_D/L = 1710$.

3.2.3 Measured Quantities

Different quantities are measured in our study to analyze the steady-state properties and the aging properties of the system. To gain some insight into the aging dynamics of vortex matter, two two-time correlation functions are computed. The first one is the *height-height autocorrelation function* $C(t, s)$

$$C(t,s) = \left\langle \left[\vec{r}_{i,z}(t) - \overline{\vec{r}}_i(t)\right] \left[\vec{r}_{i,z}(s) - \overline{\vec{r}}_i(s)\right] \right\rangle , \tag{3.5}$$

where $\vec{r}_{i,z}(t)$ are the in-plane coordinates of line i at layer z at time t, and $\overline{\vec{r}}_i(t) = \langle \vec{r}_{i,z}(t) \rangle$ is the mean lateral position of line i at time t. Here, observable quantities are averaged over all line elements as well as many noise histories and disorder realizations: The brackets $\langle a \rangle$ indicate the average over noise and disorder realizations, where $a = \frac{1}{NL} \sum_{i=1}^{N} \sum_{z=1}^{L} a_{i,z}$ denotes the average of the local variable $a_{i,z}$ over all line elements present in the system.

$C(t, s)$ thus measures the thermal fluctuations of line elements around their corresponding mean lateral line position. We remark that the term 'height-height autocorrelation function' for the transverse vortex fluctuations derives from viewing the flux lines as fluctuating one-dimensional interfaces described by a unique local height function that measures the deviation of $\vec{r}_{i,z}(t)$ from the respective line's mean.

The other two-time correlation function we compute is the *mean-square displacement* $B(t, s)$

$$B(t,s) = \left\langle [\vec{r}_{i,z}(t) - \vec{r}_{i,z}(s)]^2 \right\rangle . \tag{3.6}$$

This correlation function measures the average square distance between the position of a line element at s and the position of the same line element at a later time t. The mean-square displacement gives insight into the system's global structure and any features forming/decaying in the system.

Both two-time correlation functions were similarly measured in Refs. [36] and [37], where Monte Carlo and Langevin molecular dynamics simulations, respectively, were performed to characterize the complex non-equilibrium relaxation of initially straight and randomly placed vortex lines in the presence of point-like disorder.

Thermal spatial fluctuations are quantified by means of the vortex line *radius of gyration* $r_g(t)$

$$r_g(t) = \sqrt{\left\langle \left[\vec{r}_{i,z}(t) - \bar{\vec{r}}_i(t)\right]^2 \right\rangle} \,, \tag{3.7}$$

which is basically the root mean-square displacement from the lines' mean lateral position at time t.

Another one-time observable that we measure in our simulations is the fraction $\varphi(t)$ of pinned line elements when disorder is present. To this end, we first find the number of line elements that reside within a fixed small cut-off distance from a certain pinning center at a given time t. Then we divide this count by the total number of line elements present in the sample to yield $\varphi(t)$. Throughout our study, the cut-off distance is set equal to the pinning center radius, $r_c = b_0$. The total number of line elements can by computed by multiplying the number of layers $L = 640$ in the z direction with the number N of vortex lines present in the system.

3.2.4 Finite-Size Effects

In our work, we restrict ourselves to a low magnetic field or vortex density regime, and only consider systems composed of between $N = 10$ and $N = 21$ vortices. This naturally constitutes a tiny system compared to typical experimental samples of disordered type-II superconductors in external magnetic fields. It is therefore crucial to analyze the effects of this small vortex density, especially when we remove lines as the magnetic field suddenly decreases. We consequently ran simulations in systems with different numbers of flux lines, but keeping the density of pinning centers the same in all cases.

As demonstrated in Fig. 3.1, the data for the vortex radius of gyration $r_g(t)$, mean-square displacement $B(t, 0)$, and the fraction $\varphi(t)$ of pinned line elements that correspond to systems of different number of flux lines collapse onto a common curve. Therefore, we conclude that these differently-sized systems follow similar relaxation processes confirming that finite-size effects do not play a prominent role in this computational study of dilute systems of flux lines in a dissipative medium. It is worth noting that the physics in denser vortex systems could of course be quite different.

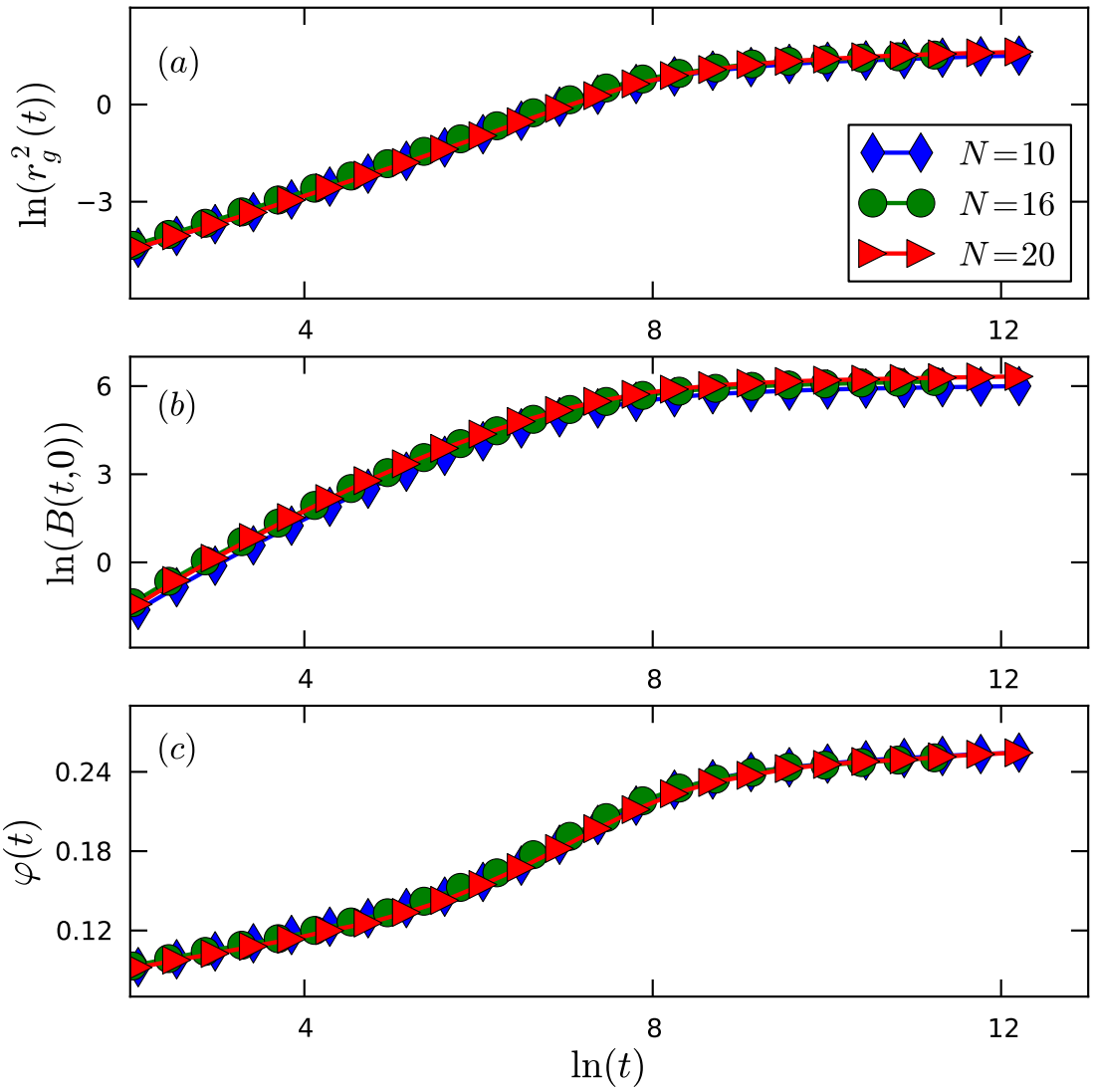

Figure 3.1: Relaxation of the (a) gyration radius, (b) mean-square displacement, and (c) fraction of pinned line elements for (dilute) systems with different number of interacting vortex lines in the presence of point-like pinning centers, averaged over 100 disorder and noise realizations.

Chapter 4

Temperature Quenches

This chapter was adapted with only minor changes from our publication:

H. Assi, H. Chaturvedi, U. Dobramysl, M. Pleimling, U. C. Täuber, "Relaxation dynamics of vortex lines in disordered type-II superconductors following magnetic field and temperature quenches", Phys. Rev. E (2015) 92, 052124. "Copyright (2015) by the American Physical Society."

We devote this chapter to a discussion of the effects of temperature quenches on the relaxation properties in systems of interacting flux lines subject to either point-like or columnar disorder.

We first consider sudden changes in the ambient temperature of the system of interacting vortex lines, with the goal to analyze the effects of instantaneous increases in temperature on the system's relaxation dynamics. At $t = 10^5$ in our simulation, we instantaneously increase the temperature from $T = 0.002$ to $T = 0.008$ in a system of $N = 16$ interacting flux lines in the presence of either type of disorder. We then compare the relaxation of the radius of gyration $r_g(t)$ and the fraction of pinned line elements $\varphi(t)$ when the temperature stays fixed with the scenario wherein it is suddenly raised. We remark that the error bars displayed in some of the figures in this section, however small they appear, always represent the standard error of the mean of the computed quantities.

We observe that the relaxation of these observables in the considered systems can invariably be mapped to an exponential function of the form $a\, e^{-t/\tau} + c$, where τ determines a characteristic relaxation time. The measured values for the relaxation times τ in different scenarios are summarized in Table 4.1. We note that the exponential relaxation of observables in our vortex model system following sudden temperatures quenches implies that physical aging features would not be discernible on time scales larger than the relaxation time τ.

In systems with point-like disorder (see also Ref. [61]), the measured relaxation time of the radius of gyration at high temperature is shorter than that at low temperature, see Table 4.1. This confirms that thermal fluctuations facilitate the roughening of vortices in the presence

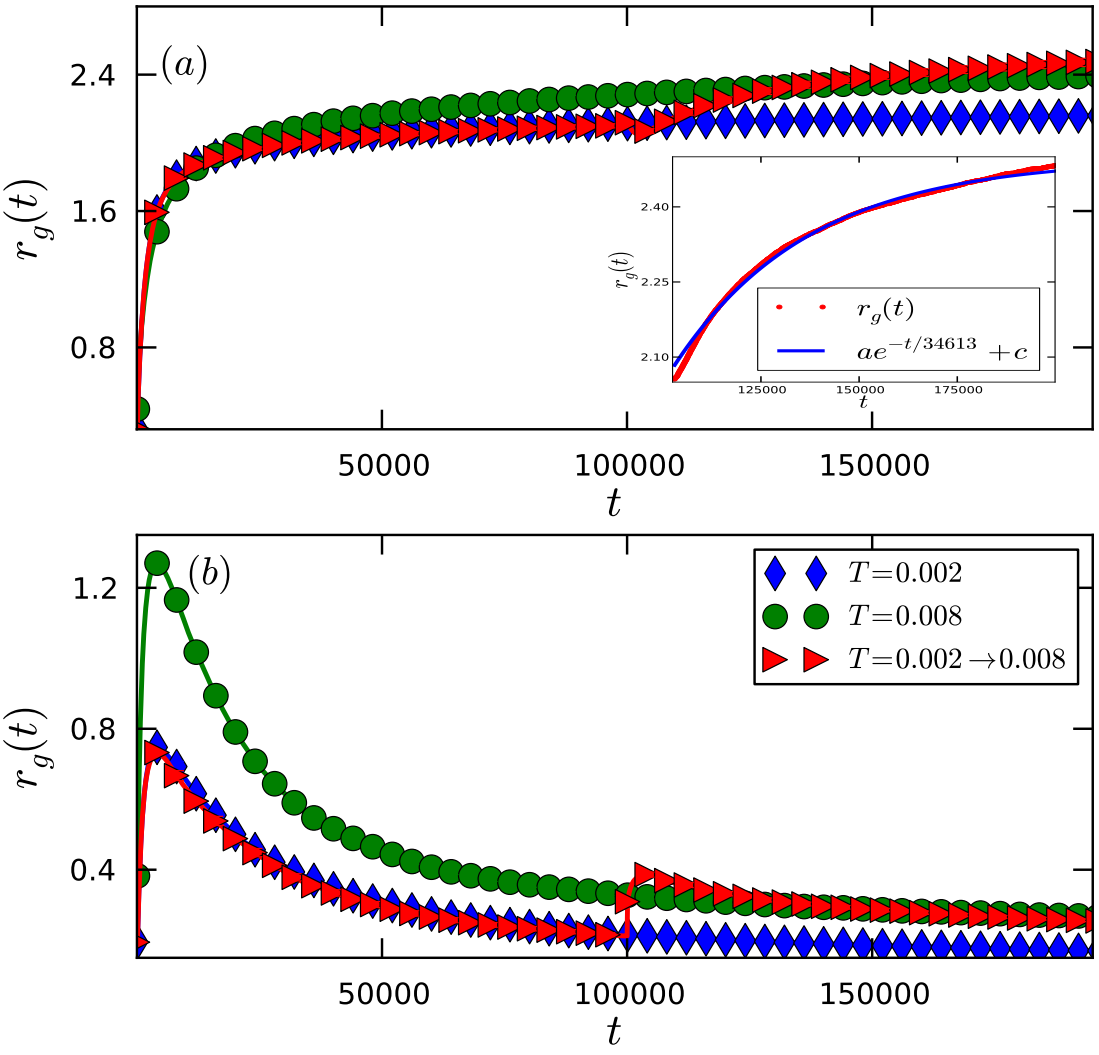

Figure 4.1: Relaxation of the gyration radius in systems of interacting vortex lines with (a) point disorder or (b) columnar defects, when the temperature is either held fixed or instantaneously raised (data averaged over 1000 realizations). The inset in (a) shows the gyration radius following the sudden temperature increase in the presence of point disorder, and a fit to an exponential function.

Defect type	$T = 0.002$	$T = 0.008$	$T = 0.002 \to 0.008$	
	r_g			φ
(a) Point-like	$5.9 \cdot 10^4$	$5.3 \cdot 10^4$	$3.5 \cdot 10^4$	$3.1 \cdot 10^4$
(b) Columnar	$3.5 \cdot 10^4$	$4.9 \cdot 10^4$	$\tau_1 = 1.6 \cdot 10^3$ $\tau_2 = 5.7 \cdot 10^4$	$3.3 \cdot 10^4$

Table 4.1: Measured characteristic relaxation times for the gyration radius r_g and the fraction of pinned line elements φ in systems of interacting vortex lines with (a) point-like and (b) columnar defects (data averaged over 1000 realizations).

of point-like disorder. Following a sudden increase in temperature, the radius of gyration first decreases a little as a few flux line segments become thermally depinned, and subsequently increases monotonically, as shown in Fig. 4.1a. We checked that this increase in $r_g(t)$ is well described by an exponential function of the form $a\, e^{-t/\tau} + c$, with relaxation time $\tau = 3.5 \cdot 10^4$ (the other parameters are $a \approx -1.73$ and $c \approx -0.09$) as observed in the inset in Fig. 4.1a. Thus, as expected, point defects enhance thermal wandering of flux lines in this disordered landscape.

In contrast, systems with columnar defects actually require a longer relaxation time for the radius of gyration at higher temperatures than that at lower temperatures, see Table 4.1, asserting that thermal fluctuations resist the straightening of vortex lines as they become localized at columnar pinning centers. When we instantaneously increase the temperature in this system, the gyration radius after the quench shows a marked fast increase, even beyond the relaxation curve for a system at constant higher temperature, followed by a much slower decrease, see Fig. 4.1b. The initial increase in r_g can likely be attributed to the creation of double-kinks in the system that are not similarly generated in relaxation processes at fixed temperature, while the final decrease is due to the decay of these metastable configurations.

A double-kink refers to a flux line configuration where the vortex is simultaneously pinned to two adjacent columnar defects. This is a long-lived state which will eventually decay to either a free vortex, or, more probably, to a straight flux line bound to a single defect column. We find that both the initial increase and the final decrease in the gyration radius again fit an exponential of the form $a\, e^{-t/\tau} + c$, but with different relaxation times (and signs of the coefficient a): In Fig. 4.1b, the fast relaxation time from the initial non-equilibrium steady state at $T = 0.002$ to the metastable state with vortex double-kinks is $\tau_1 = 1.6 \cdot 10^3$, while the much longer relaxation time from this intermediate state to the final non-equilibrium steady state at $T = 0.008$ is $\tau_2 = 5.7 \cdot 10^4$.

Note that the data for the gyration radius for both the temperature up-quench scenario as well as at a fixed high temperature in Figs. 4.1a and 4.1b will eventually approach the same curve in the long-time limit, which has not yet been reached in our simulation time window.

The differences between the systems' responses to temperature up-quenches in the presence of point and columnar pinning centers, respectively, can be attributed to the very distinct

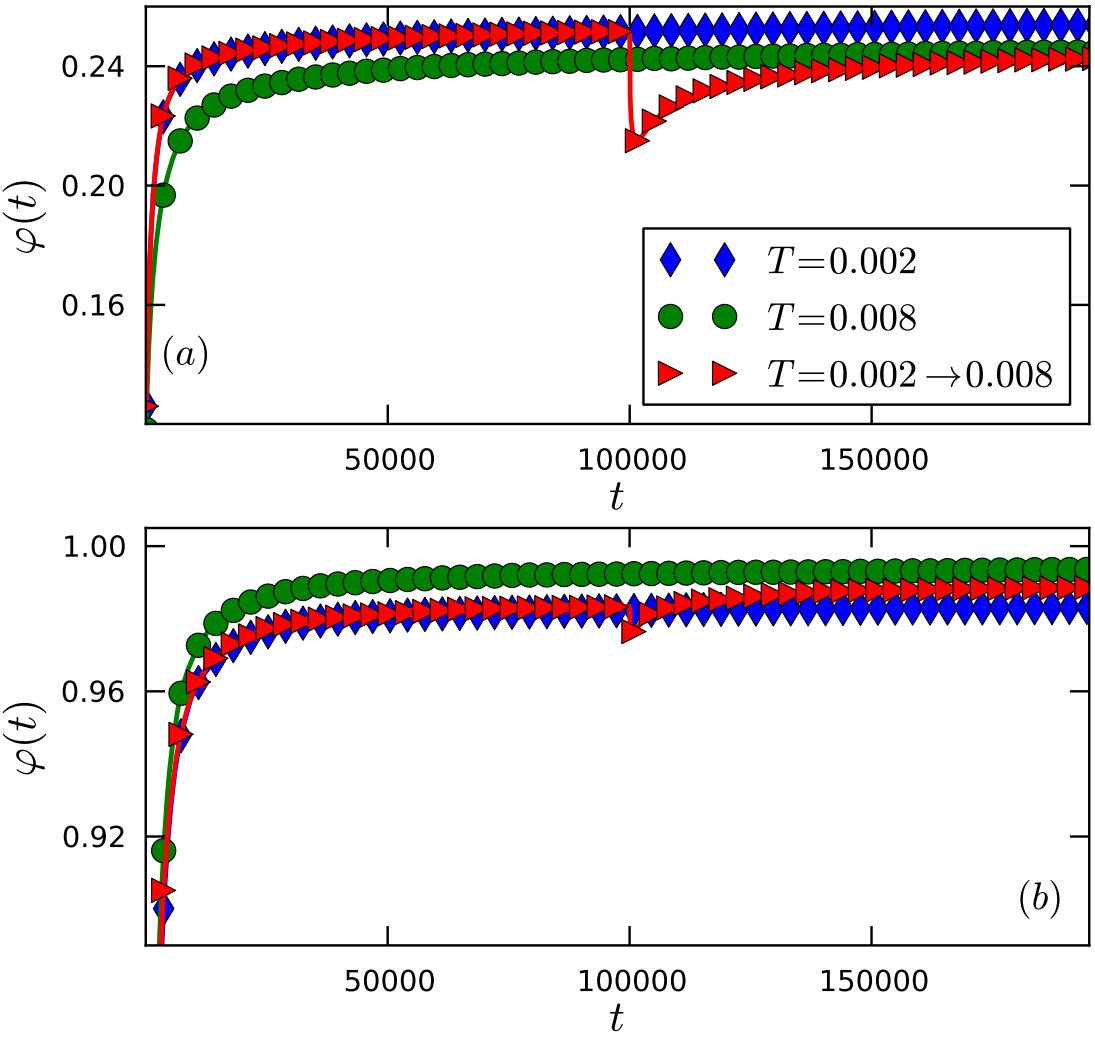

Figure 4.2: Relaxation of the fraction of pinned line elements in systems of interacting vortex lines with (a) point disorder or (b) columnar defects, when the temperature is either held fixed or instantaneously raised (data averaged over 1000 realizations).

(de-)pinning behavior that we shall again discuss later in the context of sudden magnetic field changes.

When the temperature is suddenly raised in systems with uncorrelated point disorder, some line elements become thermally depinned. The vortices are initially straightened owing to their line tension. Subsequently an increasing number of line elements finds favorable pinning sites, causing a monotonic growth in their transverse spatial fluctuations measured by r_g.

In samples with columnar defects, following a temperature up-quench some line elements migrate away from certain columnar pinning centers, which renders them subject to thermal wandering. Yet they soon become pinned to neighboring defect lines causing the subsequent decrease in the lateral spatial vortex line fluctuations, akin to systems relaxing at fixed temperature.

This scenario is confirmed by the relaxation data for the fraction of pinned line elements $\varphi(t)$ in Fig. 4.2. As observed in Fig. 4.2a, in the presence of point disorder only a minority ($\approx 25\%$) of line elements are actually pinned right before the temperature quench. A sudden increase in temperature releases a significant fraction of these pinned line elements causing a decrease in φ as well as the small dip in r_g. Later, the vortices become attached to and hence stretched between point-like pins causing a subsequent increase in φ, accompanied with a monotonic increase in the lines' spatial fluctuations.

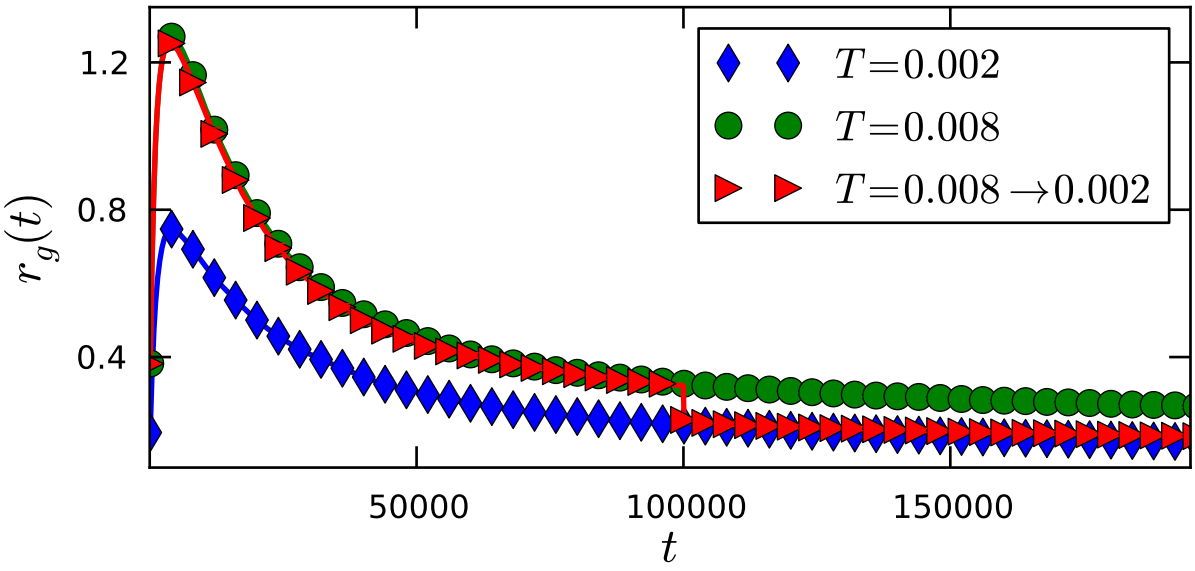

Figure 4.3: Relaxation of the gyration radius in a system of interacting vortex lines with columnar pinning centers, when the temperature is held fixed or instantaneously lowered (data averaged over 1000 realizations).

In the presence of columnar defects, on the other hand, Fig. 4.2b shows that almost all line elements are bound to pinning centers just before the temperature quench is applied. The

sudden temperature increase causes a tiny number of these line elements to depin from their localizing columns. However, they are soon to be pinned again, but partly in metastable double-kink configurations. This explains the non-monotonic pattern we observe in the spatial fluctuations with a rapid increase of r_g followed by a slow decrease.

Finally, the fraction of pinned line elements $\varphi(t)$ following the temperature quench in the presence of both types of disorder once again fits an exponential of the form $a\,e^{-t/\tau} + c$, yet with different relaxation times: $\tau = 3.1 \cdot 10^4$ for point disorder, whereas $\tau = 3.3 \cdot 10^4$ for columnar defects, see Table 4.1. This confirms that enhanced thermal fluctuations at elevated temperatures resist the straightening of flux lines as they attempt to bind to columnar defects; in stark contrast, thermal effects facilitate line roughening when vortices become pinned to uncorrelated point-like disorder.

We also analyzed the effects of a sudden drop in temperature, where we reduced the system's ambient temperature at $t = 10^5$ from $T = 0.008$ to $T = 0.002$ in our simulation runs. The subsequent vortex relaxation kinetics displays some noticeable differences as compared with the previous up-quenches: Following the temperature decrease, the gyration radius decreases and the fraction of pinned line elements increases in samples with both types of disorder, and non-monotonic behavior is observed in neither of these quantities, as depicted for r_g in Fig. 4.3. When the temperature suddenly drops, more line elements simply become pinned to either point-like or extended defects, which causes a concomitant decrease in the transverse spatial fluctuations of the vortex lines.

Chapter 5

Magnetic Field Quenches

This chapter was adapted with only minor changes from our publication:

H. Assi, H. Chaturvedi, U. Dobramysl, M. Pleimling, U. C. Täuber, "Relaxation dynamics of vortex lines in disordered type-II superconductors following magnetic field and temperature quenches", Phys. Rev. E (2015) 92, 052124. "Copyright (2015) by the American Physical Society."

We now proceed to study the effects of sudden changes in the external magnetic field, *i.e.*, vortex density, while keeping the ambient temperature fixed at $T = 0.002$ in all simulation runs for the various systems described in this chapter.

5.1 Non-Interacting Vortex Lines

5.1.1 Non-interacting Vortex Lines without Disorder

The dynamics of non-interacting directed lines in the absence of disorder can be directly mapped to the one-dimensional Edwards-Wilkinson interface growth model (which is in turn equivalent to a free noisy diffusion equation). The two-time height-height autocorrelation function (3.5) in the correlated regime is found to be [62]

$$C(t,s) = C_0 s^{1/2} \left(\left[\frac{t}{s} + 1 \right]^{1/2} - \left[\frac{t}{s} - 1 \right]^{1/2} \right) . \tag{5.1}$$

Indeed, if a simple aging scenario applies, one expects the general scaling form for the height-height autocorrelation function [31]

$$C(t,s) = s^b f_C(t/s) \tag{5.2}$$

with a scaling function f_C. In the free diffusive Edwards-Wilkinson regime, the scaling exponent is $b = 1/2$ [36,62]. In our Langevin molecular dynamics study, we first analyze this case of free non-interacting vortex lines and start with the fixed magnetic field scenario to validate our numerical code. The two-time mean-square displacement (3.6) follows a similar scaling form to (5.2).

Since the present flux lines relax for a long initial time $r = 10^5$, which is much larger than the waiting times s and measurement time t, we need to take this elapsed time r into account when analyzing the behavior of these lines, and therefore new times $\sigma = r + s$ and $\Gamma = r + t$ are introduced.

As shown in Fig. 5.1, our data for both $B(\Gamma, \sigma)$ and $C(\Gamma, \sigma)$ indeed satisfy dynamical scaling for all explored waiting times with the predicted scaling exponent $b = 1/2$, after properly accounting for the long initial relaxation time r, see Sec. 3.2.2.

When we follow our magnetic field quench scenario, and suddenly reduce the vortex density after letting the system relax for an extended time period, we obtain the very same relaxation results for both $B(\Gamma, \sigma)$ and $C(\Gamma, \sigma)$, which is to be expected since the lines are not interacting.

Similarly, when we instantaneously increase the magnetic field, $B(\Gamma, \sigma)$ and $C(\Gamma, \sigma)$ measured for those vortices that were present initially are not significantly different from those quantities obtained at fixed flux density, as the relaxation processes for these non-interacting vortex lines are statistically the same in both situations. However, the subpopulation of newly added lines displays a similar, but less perfect collapse for $C(t, s)$ than that displayed in Fig. 5.1b since these lines were not present for the previous long relaxation time r, and thus are not yet as relaxed as the initial lines. On the other hand, $B(t, s)$ obtained just for the added lines exhibits perfect dynamical scaling with the scaling exponent $b = 1/2$.

In summary, we confirm the expected Edwards-Wilkinson aging scaling for the non-equilibrium relaxation dynamics of non-interacting flux lines in the absence of disorder, regardless of sudden changes in their density. The following subsections highlight the effects of disorder on the relaxation dynamics of non-interacting, thus statistically independent vortex lines.

5.1.2 Non-interacting Flux Lines with Point Disorder

Keeping the repulsive vortex-vortex interactions switched off, we now introduce point defects into the system to study the effects of this type of spatially uncorrelated disorder on the relaxation dynamics.

First, we consider the situation of fixed magnetic field (vortex density), and study the same dynamical quantities as in the previous section, see also Refs. [36, 37]. The mean-square displacement $B(\Gamma, \sigma)$ does not display dynamical scaling with $b = 1/2$ as in the disorder-free case. Instead, dynamical scaling ensues for $B(\Gamma, \sigma)$ with the aging exponent $b \approx 0.725$, *c.f.*

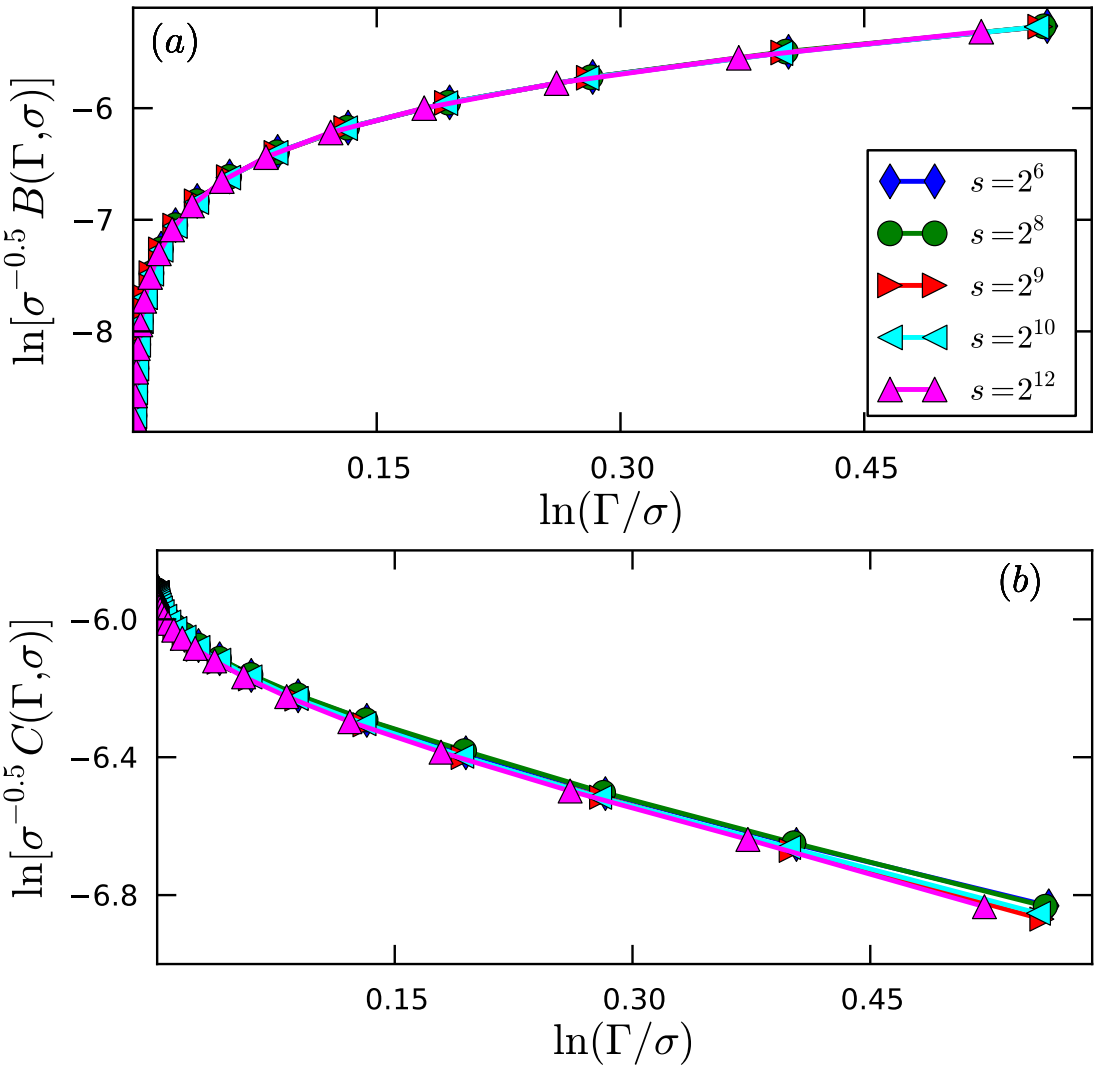

Figure 5.1: Relaxation of (a) the mean-square displacement and (b) the height-height autocorrelation function for non-interacting vortices in the absence of disorder and for fixed vortex density (data averaged over 800 realizations).

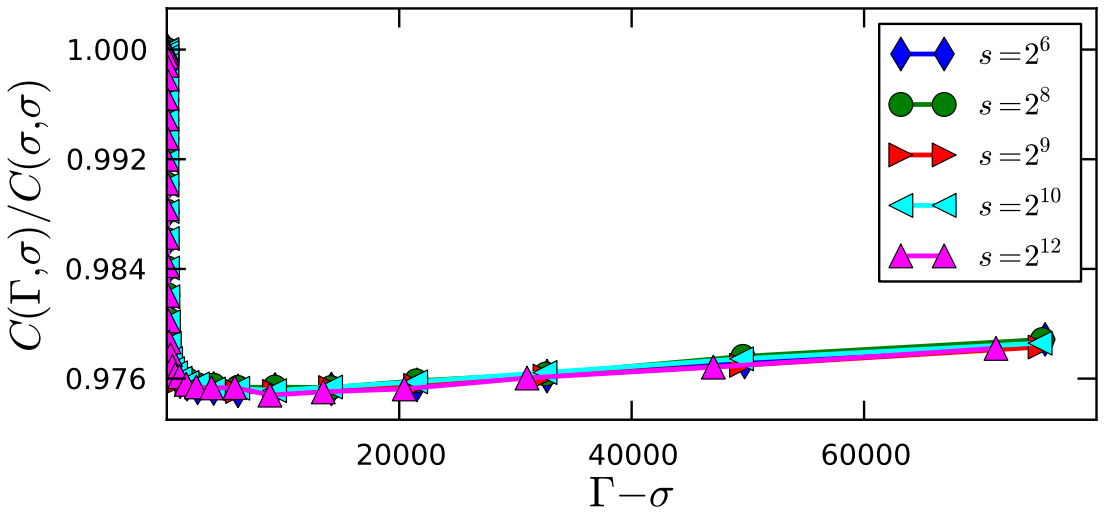

Figure 5.2: Relaxation of the normalized height-height autocorrelation function in a system of non-interacting flux lines subject to point-like disorder, when the number of flux lines stays fixed (data averaged over 800 realizations).

Fig. 6(d) in Ref. [37]. In contrast, dynamical scaling is not observed for the height-height autocorrelation function $C(\Gamma, \sigma)$. As shown in Fig. 5.2, the data for all waiting times s display identical time evolution, since the system has in fact fully equilibrated owing to the long relaxation period $r = 10^5$, and time translation invariance is restored. The height autocorrelation function shows a similar increase for all waiting times indicating that flux line elements keep exploring their surroundings in search of favorable pinning sites, which causes the lines to continuously roughen due to the uncorrelated nature of the point-like disorder in the system.

The results for a sudden magnetic field decrease (vortex density down-quench) turn out to not significantly differ from the situation with constant field. This is readily attributed to the fact that the lines are not interacting, and thus the remaining vortices after the quench are not at all affected by the removal of some lines from the sample.

More distinct features are observed upon an instantaneous increase of the magnetic field: First of all, the mean-square displacement $B(\Gamma, \sigma)$ of the initial lines does not display dynamical scaling anymore, but the data (not shown) reveal that this vortex subpopulation has rather recovered time translation invariance, since they all collapse onto a single curve when plotted against $\Gamma - \sigma = t - s$, while the added line subpopulation displays neither of these straightforward features. The height-height autocorrelation function $C(\Gamma, \sigma)$ of the initial lines shows time translation invariance, akin to the data in Fig. 5.2. On the other hand, $C(t, s)$ for the added lines, depicted in Fig. 5.3a, displays an initial decrease followed by an increase, with the minimum shifted to later $t-s$ values for longer waiting times s. The decrease happens when the added lines start noticing the presence of the pinning centers and

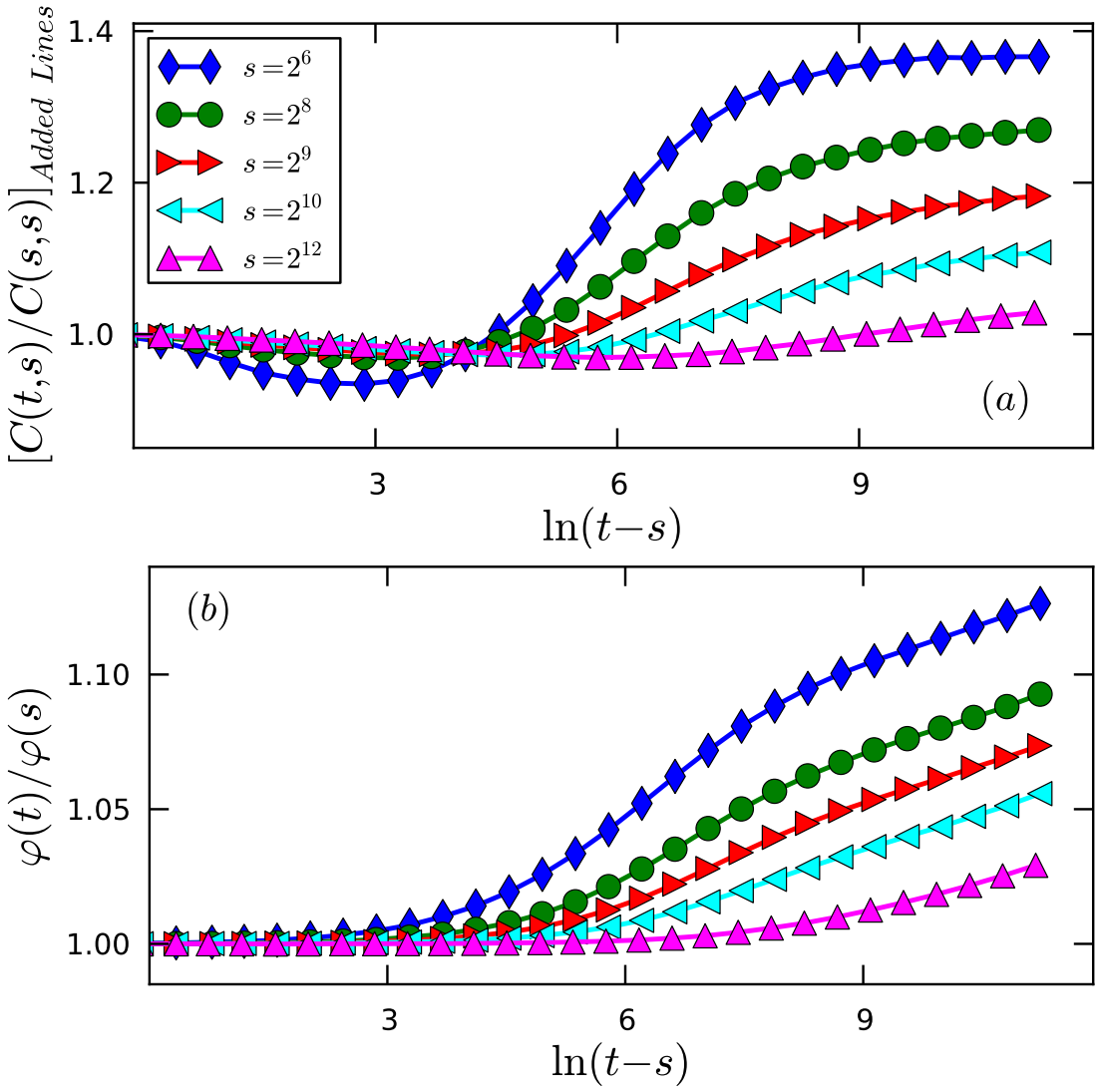

Figure 5.3: Relaxation of (a) the normalized height-height autocorrelation function of the newly added flux lines, and (b) the fraction of pinned line elements in a system of non-interacting vortices subject to point disorder, following a sudden increase in the magnetic field or vortex density (data averaged over 800 realizations).

become pinned to nearby defects, which decreases their transverse fluctuations. The subsequent increase is caused by the flux lines exploring more of the sample and thus becoming rougher as they optimize their pinning configurations.

Hence, the behavior of the added lines is highly influenced by disorder as demonstrated by their height autocorrelations. A one-time observable that also highlights the effects of the sudden increase in the magnetic field is the fraction of pinned vortex line elements φ. In the presence of point disorder, this fraction as shown in Fig. 5.3b displays a two-step increase, which can be attributed to the pinning dynamics of the newly added magnetic flux lines, as discussed in the context of Fig. 5.3a.

5.1.3 Non-interacting Vortices with Columnar Defects

We proceed to change the type of pinning centers present in the system to columnar defects, which are linearly extended pinning sites that are simulated as potential wells aligned along the z direction, and compare their effects on the relaxation kinetics of non-interacting vortices to that of uncorrelated point disorder.

We again first hold the magnetic field constant and consider the different two-time correlation functions studied above. The mean-square displacement $B(\Gamma, \sigma)$ is found to display dynamical scaling with the aging exponent $b = 1/2$, similar to Fig. 5.1a in the absence of disorder. It is worth recalling that when flux lines are completely pinned to columnar defects, their mean-square displacement becomes constant, of the order of b_0. We therefore conclude that the dynamics of $B(\Gamma, \sigma)$ in the accessible time window is clearly dominated by the still unattached lines in the system. The height-height autocorrelation function $C(\Gamma, \sigma)$ does not display dynamical scaling with any fixed scaling exponent. However, when considering the normalized $C(\Gamma, \sigma)$ with respect to the initial value $C(\sigma, \sigma)$ as depicted in Fig. 5.4a, we observe that the data for all different waiting times s perfectly collapse onto a single curve, which indicates that time translation invariance is restored and the system is well equilibrated. Next, we measure the fraction of pinned line elements in the system with columnar defects, see Fig. 5.4c. The data for different waiting times collapse onto a single graph, where the fraction of pinned line elements stays constant for an extended time period and only later, at $\ln(\Gamma - \sigma) \approx 7$, starts increasing. This indicates that $\Gamma \approx 1096 + \sigma$ represents a characteristic time scale when pinning to columnar defects becomes prominent in the system.

When vortices are removed from this system of non-interacting flux lines with columnar defects, the measured mean-square displacement, height autocorrelations, and fraction of pinned line elements all yield identical results to the situation when there is no sudden magnetic field change, as is to be expected in the absence of correlations.

Upon introducing additional flux lines into the system, the mean-square displacement of both the initial and the added lines subpopulations shows dynamical scaling for all waiting times with the same exponent $b = 1/2$ as in the fixed density and field down-quench scenarios.

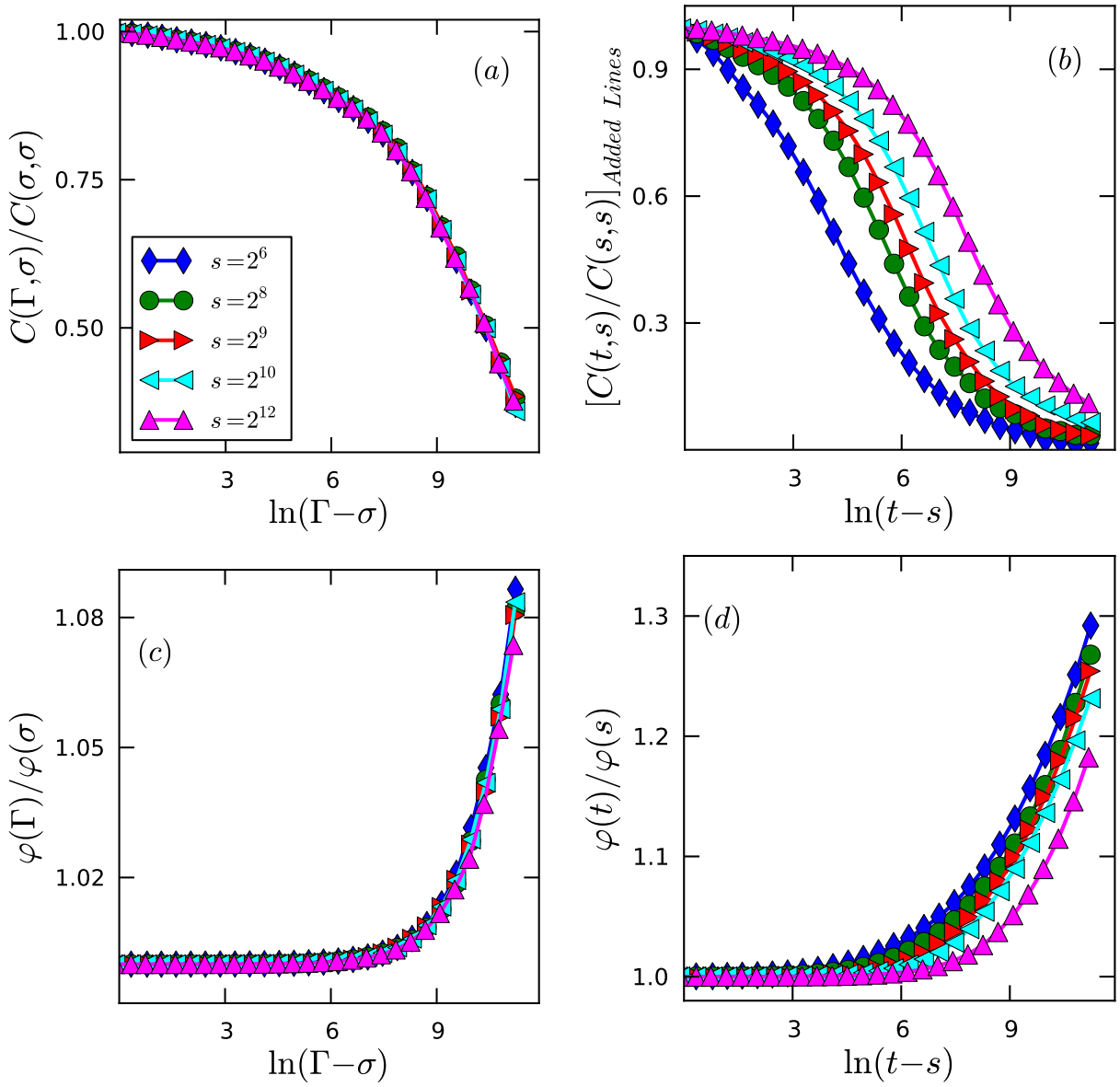

Figure 5.4: Relaxation of various observables in a system of non-interacting flux lines with columnar defects, (a,c) when the vortex density remains fixed; (b,d) after a sudden increase in the magnetic field: (a,b) normalized height-height auto-correlation function, (c,d) fraction of pinned line elements (data averaged over 800 realizations).

This confirms that sudden changes in the vortex density do not alter the global dynamics of non-interacting flux lines in the presence of columnar defects. The autocorrelation function $C(\Gamma, \sigma)$ for the initially present lines turns out very similar to that at fixed density, see Fig. 5.4a, whereas the data corresponding to the newly added lines cannot be collapsed according to a simple aging scaling form when plotted against the time ratio t/s. However, the graphs $C(t, s)$ for the added lines for various s do not just fall onto a single curve when plotted against $t - s$, as demonstrated in Fig. 5.4b. This indicates that this subpopulation of lines is not yet equilibrated for the range of waiting times s employed here. As the additional lines are inserted into the sample, depending on the elapsed waiting time s, they require different time periods t to explore the system and become attached to columnar pins. This is corroborated in the time evolution of the fraction of pinned line elements φ for different waiting times in Fig. 5.4d, which also does not yield data collapse.

The flux lines present in the sample, especially vortices that were suddenly added to the system, start exploring the surrounding pinning centers sooner for shorter waiting times, whence one observes an earlier increase in the fraction of pinned line elements for smaller s. For the long waiting times in Fig. 5.4d such as $s = 2^{12}$, the fraction of pinned line elements is fixed at a plateau value for an extended duration because the vortices already had enough time to relax towards favorable configurations after the field up-quench. The increase in $\varphi(t)$ happens at a much later time indicating that the line elements might be migrating between neighboring columnar pinning centers to become pinned to whole defect lines, whereupon their lateral line fluctuations diminish. The overall trend in the presence of columnar defects is that the dynamics is dominated by the few lines that remain unattached to any pins, and the tendency of each flux line to become fully localized to a single columnar pinning center, which in turn straightens the vortex lines.

The preceding discussions highlight the influence of different types of disorder on non-interacting vortex matter and the relaxation dynamics following magnetic field quenches. We expect that quite distinct relaxation kinetics will be observed when mutual vortex interactions are added to our consideration and collective behavior ensues, as will be explored in the following section.

5.2 Interacting Vortex Lines

5.2.1 Interacting Vortex Lines without Disorder

We start with the system of interacting flux lines without disorder. At a fixed magnetic field, we observe at least approximate dynamical scaling of $B(\Gamma, \sigma)$ as displayed in Fig. 5.5a, yet with a different exponent $b = 1.57$ from before. On the other hand, the height-height autocorrelation function in Fig. 5.5b shows a distinct two-step relaxation behavior, where a β relaxation with almost no changes in $C(\Gamma, \sigma)$ is followed by a very slow decay. This is

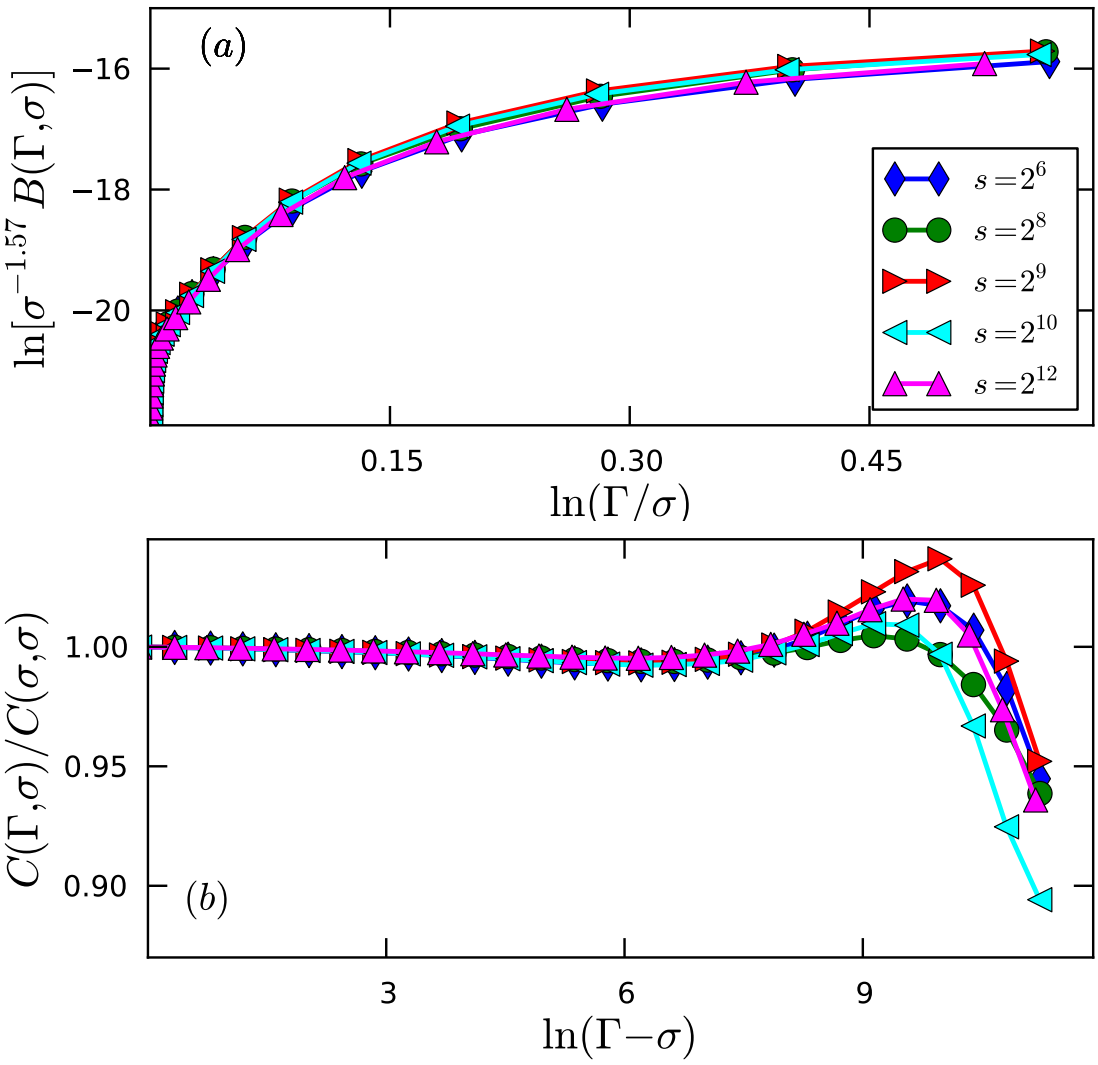

Figure 5.5: Relaxation of (a) the mean-square displacement and (b) the normalized height-height autocorrelation function in a system of interacting flux lines in the absence of disorder, when the number of flux lines stays fixed (data averaged over 800 realizations).

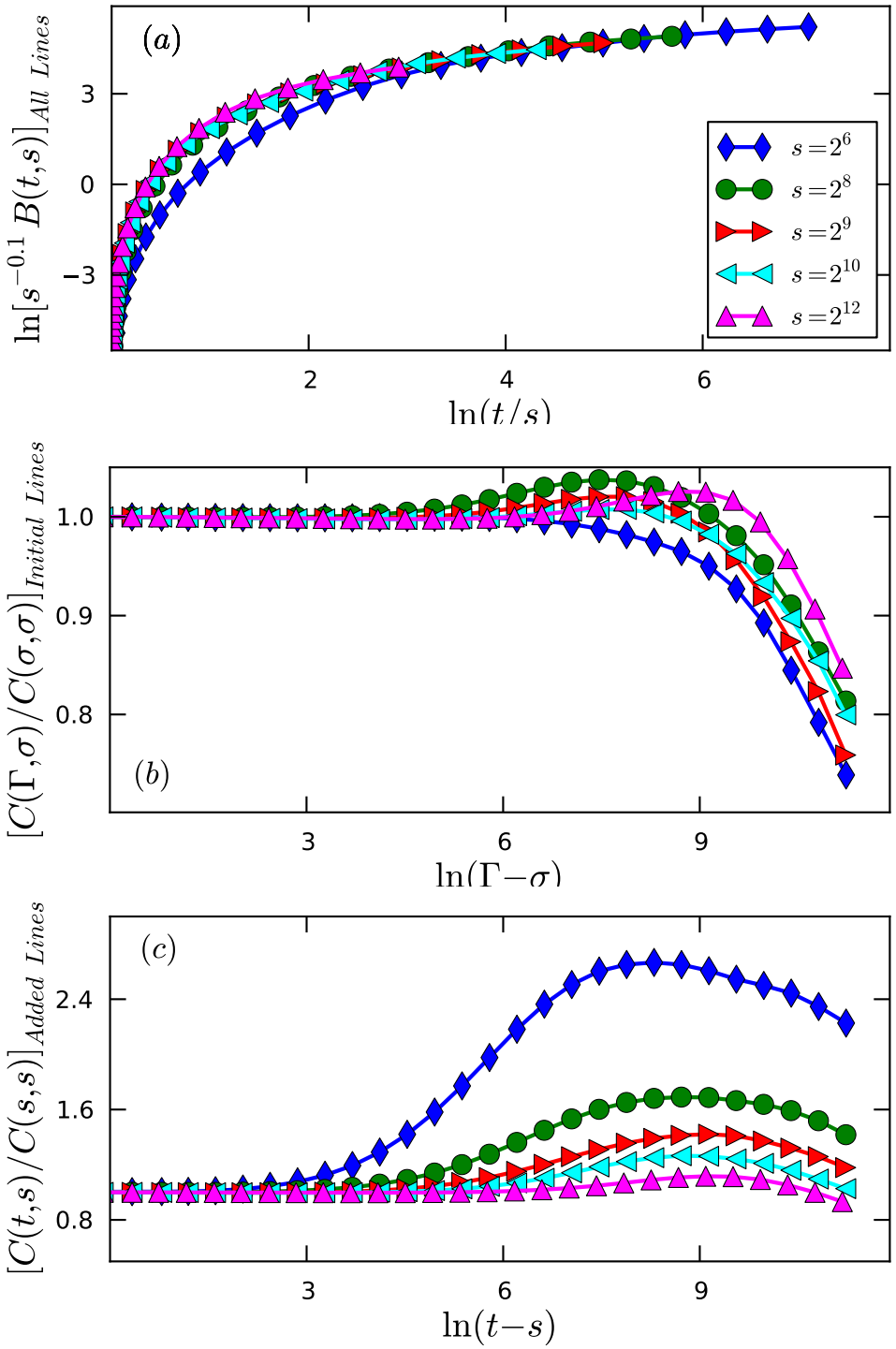

Figure 5.6: Relaxation of (a) the mean-square displacement of all the flux lines combined, the normalized height-height autocorrelation function of (b) the initially present vortices, and (c) the newly added lines in a system of interacting flux lines in the absence of disorder, following a sudden increase in the magnetic field (data averaged over 900 realizations).

referred to as α-β relaxation scenario, a characteristic feature of structural glasses [36, 63]. Furthermore, a local maximum in $C(\Gamma, \sigma)$ is observed for all waiting times s, which we attribute to the decay of metastable kink configurations. Such single kinks are step-like flux line structures that are stabilized by the screened logarithmic repulsive forces; hence they constitute interaction-induced features that are long-lived. The mean-square displacement $B(\Gamma, \sigma)$ loses the dynamical aging scaling property when lines are removed from the system, whereas $C(\Gamma, \sigma)$ displays similar behavior to that at fixed magnetic field, but with the local maxima absent for most waiting times. This indicates a destabilization of single-kink structures due to the decrease in the number of lines in the sample, which relieves the effective mutual cages generated by the repulsive interactions.

On the other hand, when the magnetic field is suddenly increased and vortices are added to the system, we observe the same time evolution in the mean-square displacement of the added lines, the initial lines, and all the lines combined. The data corresponding to all waiting times collapse onto a single curve with a long-time algebraic growth with the aging scaling exponent $b = 0.1$, see Fig. 5.6a. This dynamical scaling is manifest only when the initial relaxation time r is disregarded in our scaling formula for both the initial lines and the collection of all lines. The independence of these subpopulations from the initial relaxation time implies that the respective lines do not retain memory of their early dynamics and only experience changes upon the addition of new vortices, reflecting the mutual interactions and consequent dynamical correlations.

We observe a more diverse temporal evolution in the height-height autocorrelation functions. The initial lines in Fig. 5.6b show α-β relaxation for all waiting times s with the presence of local maxima similar to those in Fig. 5.5b. The data display a rather complicated dependence on the sequence of waiting times, which we cannot explain in detail but attribute to the rich and complex nature of the combined vortex system when these initially present and largely relaxed flux lines interact with newly added straight ones. Unlike the initial line subpopulation, the added vortex kinetics presented in Fig. 5.6c displays a plateau followed by an increase, which is in turn followed by a final decrease for all waiting times. The first increase indicates the time scale when the added lines start noticing the repulsive effect of the already existing vortices, whence lateral fluctuations are enhanced. At later times following this initial increase, $C(t, s)$ decreases again indicating that the lines have reached a steady state with well-established mutual interaction cages, and hence their fluctuations become reduced.

In the following subsections, we investigate and analyze the effects of disorder on samples of interacting vortex lines. We first address uncorrelated point-like defects and then proceed to extended columnar pins.

5.2.2 Interacting Flux Lines with Point Disorder

Considering first the case when the magnetic field does not suddenly change, our sample of interacting lines in the presence of point disorder (see Ref. [61]) shows dynamical scaling for $B(\Gamma, \sigma)$ with the aging exponent $b = 1.54$, similar to the scaling behavior displayed in Fig. 5.5a in the disorder-free interacting vortex system. This similarity suggests that the strong repulsive forces between the flux lines dominate over the effects of point-like pinning centers, which do not play a significant role in modifying the global relaxation dynamics of interacting vortices. Even though the height-height autocorrelation function does not show dynamical scaling, the data for the different waiting times collapse onto a single curve indicating that the system has effectively equilibrated, see Fig. 5.7a. The fraction of the pinned line elements $\varphi(t)$ depicted in Fig. 5.7c too shows evidence for equilibration for all waiting times considered in our simulations.

The data display a plateau followed by an increase in the pinned line element fraction at $\ln(\Gamma - \sigma) \approx 7$, which coincides with the time of marked decrease in $C(\Gamma, \sigma)$, confirming that $\Gamma \approx 1096 + \sigma$ represents a characteristic temporal scale when pinning to point-like defects causes significant flux line roughening.

When flux lines are suddenly removed from the system, $B(\Gamma, \sigma)$ of the remaining lines does not display dynamical scaling. Moreover, $C(\Gamma, \sigma)$ in Fig. 5.7b still shows the α-β relaxation scenario for all waiting times without the system ever becoming fully equilibrated as in Fig. 5.7a. The fraction of pinned line elements undergoes a more diverse temporal evolution for the different waiting times, as can be observed in Fig. 5.7d. For short waiting times $s \leq 2^8$, a minimum in φ occurs at $\ln(\Gamma - \sigma) \approx 6.2$. The initial decrease indicates that the sudden release of caging due to removed lines leads to depinning of some remaining vortices from point defects where the line elements were only held in place because of their interactions with the removed lines. This enables the remaining flux lines to explore a farther range of their surroundings, ultimately becoming bound to new and more point pins to eventually reach a steady-state fraction φ that is a little larger than the initial one. For intermediate-to-larger waiting times $s > 2^9$, this minimum in the pinned line element fraction is not visible and the data looks similar to the situation with fixed vortex density, see Fig. 5.7c; the only difference being that the quenched system has clearly not equilibrated yet.

Let us now explore the effects of a sudden increase in the magnetic field, where new straight flux lines are added to the a previously relaxed system of interacting vortices in the presence of point disorder, and analyze the resulting dynamics. Dynamical scaling of the mean-square displacement is lost for the newly added lines, the initially present vortices, and all the flux lines combined. However, the mean-square displacement as function of time looks similar among all these different subpopulations; an example is shown in Fig. 5.8a. Note that our choice of a putative aging scaling exponent $b \approx 0.8$ in Fig. 5.8a is merely to demonstrate the global dynamical evolution of $B(t, s)$ for the different vortex subpopulations.

On the other hand, the height-height autocorrelation function shows similar results for the

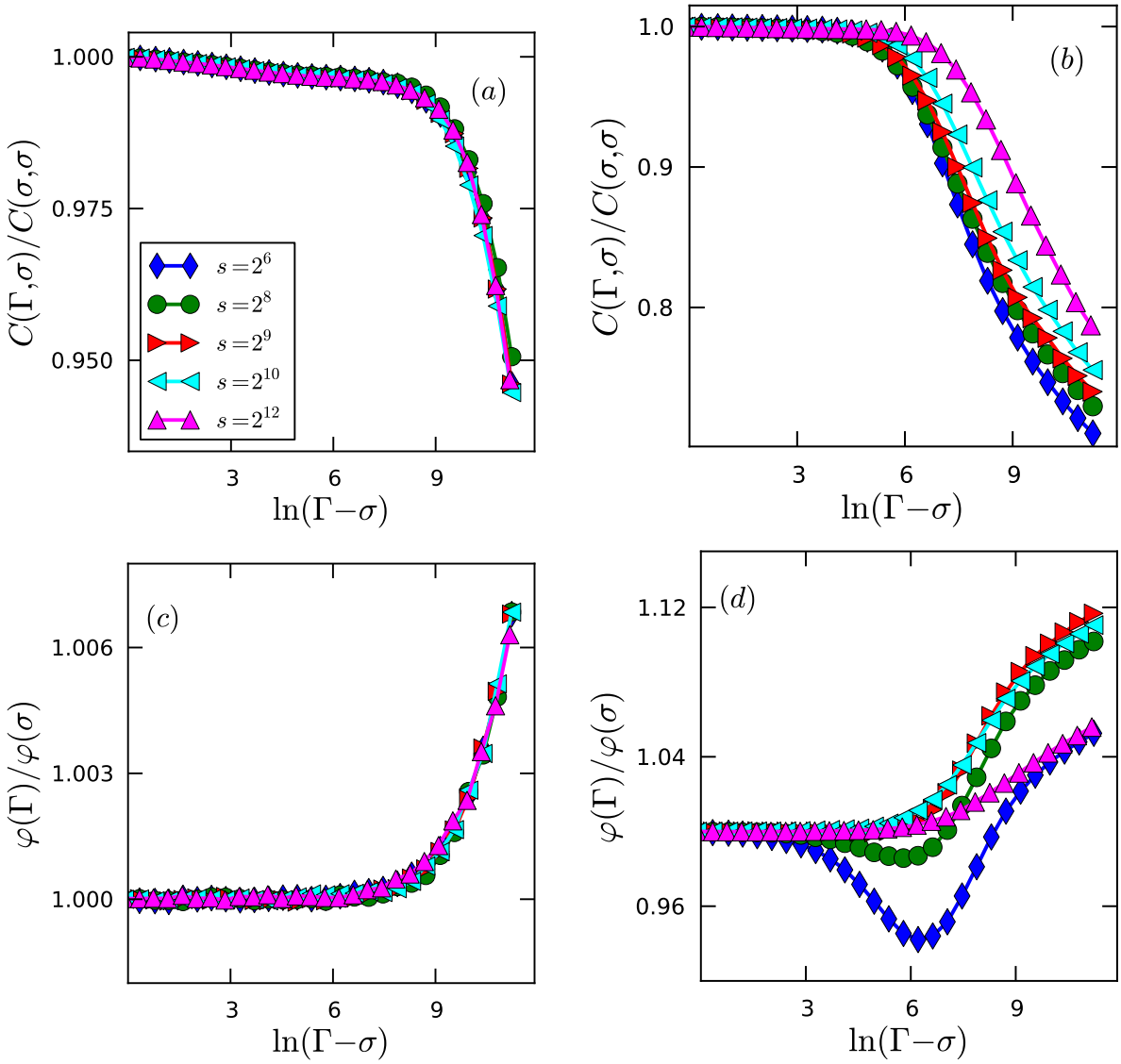

Figure 5.7: Relaxation of various observables in a system of interacting flux lines with point-like disorder when (a,c) the vortex density remains fixed, and (b,d) after a sudden magnetic field decrease: (a,b) normalized height-height autocorrelation function, (c,d) fraction of pinned line elements (data averaged over 800 realizations).

initial lines and the combination of all vortices, as shown in Fig. 5.8b, where α-β relaxation is evident as a characteristic feature in these flux line subpopulations that have already relaxed for a long time period, but are still not equilibrated. This lack of equilibration becomes manifest in the height-height autocorrelation function for just the subpopulation of added lines in Fig. 5.8c. For these newly introduced vortices, only very long waiting times $s \geq 2^{12}$ display α-β relaxation kinetics comparable to the situation at fixed magnetic field. However, data corresponding to $s < 2^{12}$ show an initial increase in $C(t, s)$ followed by a slow decrease. When new flux lines are inserted into the sample, the originally present vortices repel them and thus facilitate their pinning to the uncorrelated point disorder, which enhances transverse line fluctuations. At $\ln(t-s) \approx 7$, the added lines' height autocorrelation function decreases because the lines have found a (near) optimal pinning configuration. The fraction of pinned line elements behaves analogously to that in the case of a sudden vortex density decrease, Fig. 5.7d, with the mere difference that the minimum is less pronounced for a sudden magnetic field up-quench. Yet in this case, the sudden presence of additional caging potentials (rather than their release) and subsequent vortex rearrangement leads to the observed behavior of the pinned line element fraction.

5.2.3 Interacting Vortices with Columnar Defects

Finally, we analyze a sample of interacting flux lines in the presence of columnar defects, and compare the relaxation kinetics in this system with the preceding investigation of uncorrelated point disorder.

We first study the case when the magnetic field stays constant. We find that $B(t, s)$ shows dynamical scaling at long times with the aging scaling exponent $b = 0.8$, see Fig. 5.9. In contrast, no dynamical scaling is obtained for $C(\Gamma, \sigma)$ which displays a time evolution similar to that in Fig. 5.7a for point defects. The fraction of pinned line elements in the presence of columnar defects turns out to not significantly differ from that in the presence of point disorder at fixed vortex density.

When flux lines are removed from the sample, dynamical scaling is not observed for $B(\Gamma, \sigma)$, even at long times. Furthermore, time translation invariance in the normalized height-height autocorrelation function indicates an essentially equilibrated system that undergoes α-β relaxation. This behavior is accompanied by an increasing fraction of pinned line elements confirming that the remaining flux lines undergo similar relaxation dynamics as in the system at fixed magnetic field, namely a continuous straightening and hence reduced transverse fluctuations as the vortices find nearby columnar pinning centers.

Quite different features are observed when the magnetic field is increased instantaneously: The temporal growth of the mean-square displacement $B(t, s)$ of the newly introduced lines looks similar to samples with point-like disorder as shown in Fig. 5.8a. The similarity in the mean-square displacement in the presence of both point and columnar pinning sites underscores our earlier observation that introducing disorder into the interacting vortex

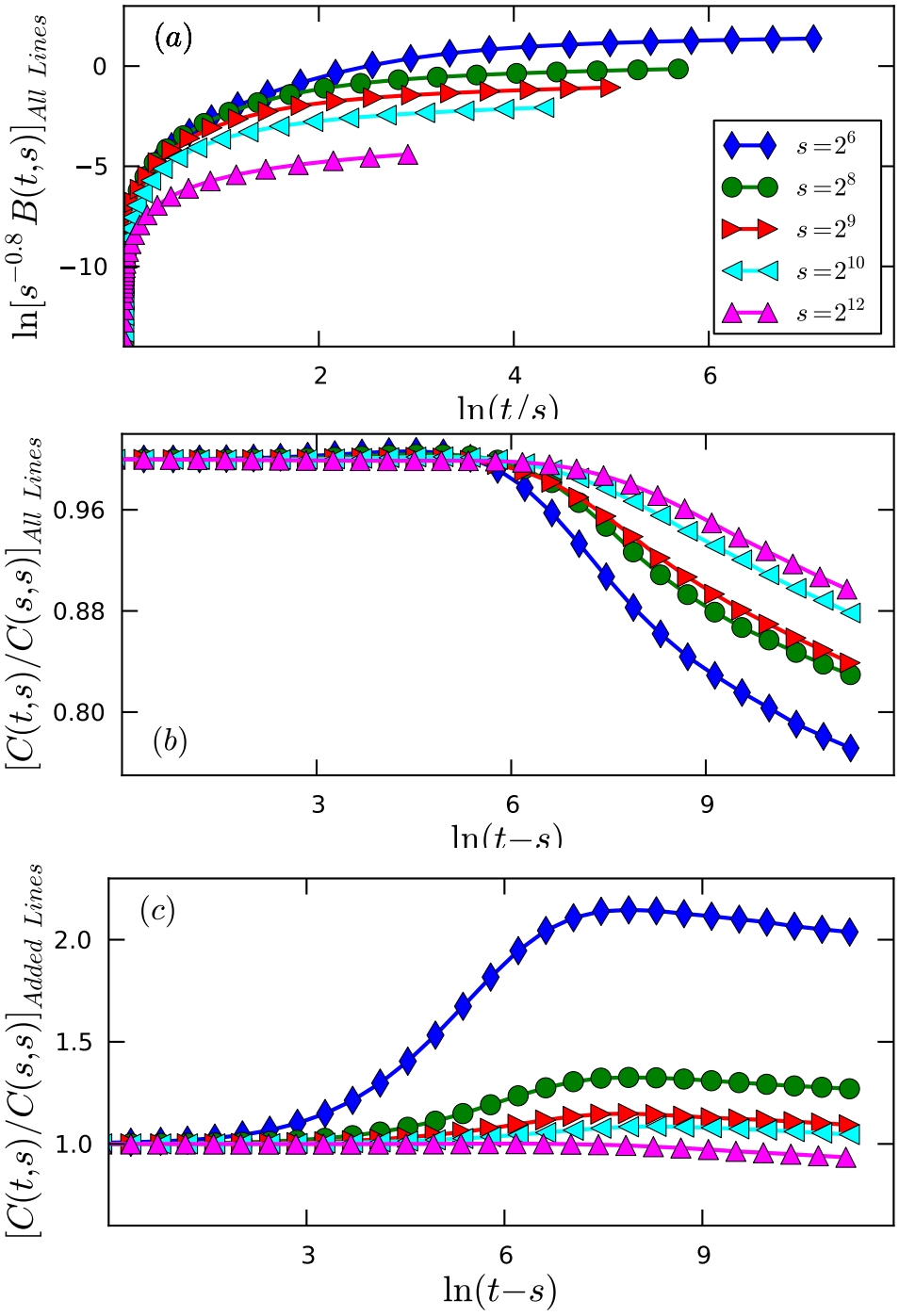

Figure 5.8: Relaxation of (a) the mean-square displacement, the normalized height-height autocorrelation function (b) of all the flux lines combined, and (c) of the subpopulation of newly added lines in a system of interacting vortices subject to point disorder, following a sudden increase in the magnetic field (data averaged over 800 realizations).

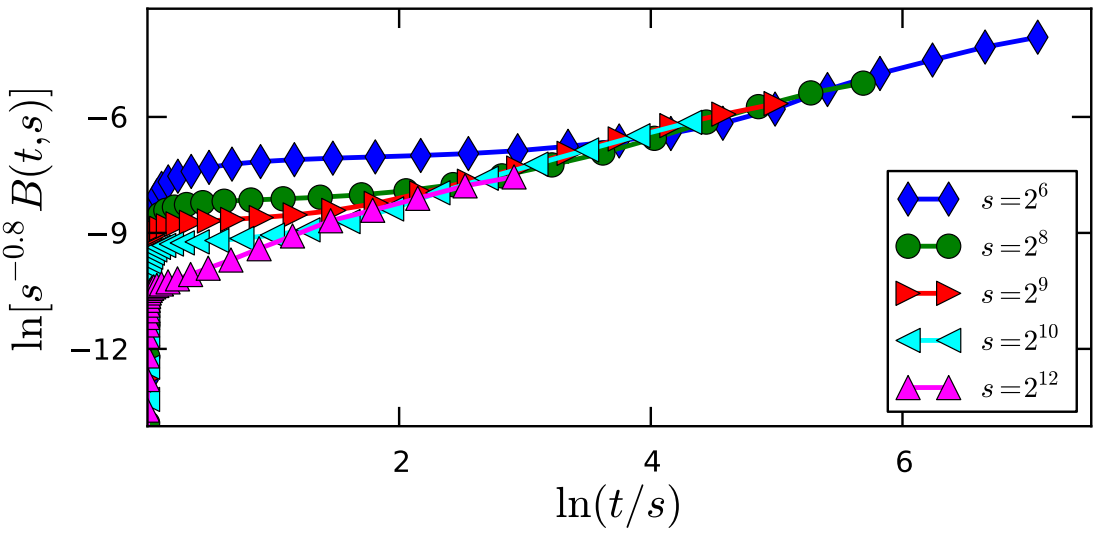

Figure 5.9: Relaxation of the mean-square displacement in a system of interacting flux lines with columnar defects, when the vortex density remains fixed (data averaged over 1500 realizations).

system has comparatively little effect on the global dynamics which is highly dominated by the strong repulsive forces between the flux lines. Analogous to the case when point disorder is present, all the different vortex subpopulations show similar results for the mean-square displacement.

On the other hand, the added vortices and the initially present flux lines are characterized by different height autocorrelations. The initial vortices as well as the combination of all lines display α-β relaxation for all waiting times s. The appearance of local maxima for some long waiting times indicate the decay of long-lived vortex double kinks in the system. However, the subpopulation of added lines displays different features in their height autocorrelations $C(t,s)$ for the different waiting times, see Fig. 5.10a. For short waiting times, *e.g.* $s = 2^6$, an initial decrease is followed by a pronounced maximum in $C(t,s)$. The initial decrease is set by the time scale when the added flux lines begin to notice the pinning centers, causing their local transverse fluctuations to decrease. The following increase indicates the characteristic time range when the additional vortices start feeling the repulsive interactions with the initially present flux lines and with one another; this produces enhanced fluctuations about their mean lateral positions. This increase continues until pinning effects start to again dominate the relaxation dynamics, rendering the lines straighter and thus reducing vortex line fluctuations. For longer waiting times, α-β relaxation becomes more prominent, with small local maxima present for waiting times $s = 2^8$ and $s = 2^9$. Moreover, the fraction of pinned line elements in Fig. 5.10b shows an increase followed by asymptotic saturation for all waiting times tested in our simulations.

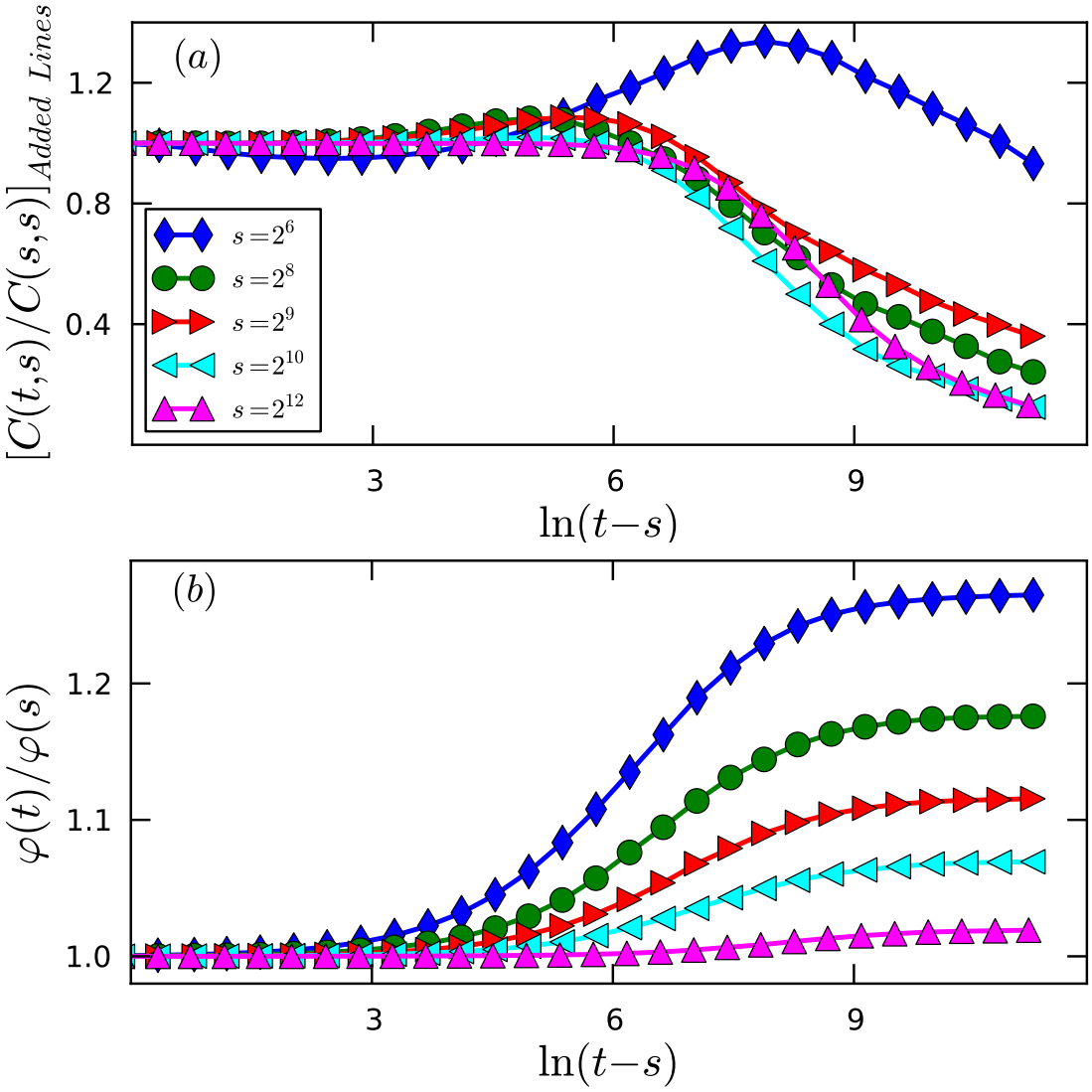

Figure 5.10: Relaxation of (a) the normalized height-height autocorrelation function of the newly added flux lines, and (b) the fraction of pinned line elements in a system of interacting vortices with columnar defects, following a sudden increase in the magnetic field (data averaged over 800 realizations).

Chapter 6

Conclusions

This concluding chapter was adapted from our publication, reference [64], with slight modifications to the text.

We have explored the effects of incorporating experimentally motivated initial conditions into the study of the non-equilibrium relaxation dynamics of magnetic flux lines in type-II superconductors. Random initial conditions were considered in our earlier work in Refs. [36, 37]. In the present study, we focused on the effects of sudden changes in temperature and magnetic field on the ensuing vortex relaxation properties. We investigated the differences between the relaxation kinetics of flux lines in the presence of uncorrelated point-like disorder and columnar defects. To this end, we modeled the magnetic vortices as directed elastic lines and employed a Langevin molecular dynamics algorithm to simulate the vortex kinetics.

We studied the relaxation of a system of interacting flux lines in the presence of disorder at fixed temperatures to confirm that higher temperatures induce enhanced thermal fluctuations that counteract the straightening of the vortex lines caused by their pinning to columnar defects, while in contrast these same fluctuations help lines to roughen when binding to uncorrelated point-like disorder. Furthermore, we investigated the relaxation processes following sudden changes in the ambient temperature. Systems subject to the two types of disorder show very distinct relaxation dynamics when the temperature is instantaneously increased due to the different (de-)pinning behavior from these defects. Some flux line elements become depinned from the uncorrelated point defects following a sudden increase in the sample's temperature confirming that this type of disorder enhances the thermal wandering of flux lines. However, samples with columnar defects display a non-monotonic behavior in spatial fluctuations due to the creation and subsequent decay of vortex double-kinks. These pronounced differences between systems with point-like and columnar defects are not present when the temperature is suddenly reduced, since this decrease simultaneously binds more line elements to the pinning centers, regardless of the type of disorder present in the sample.

We carefully investigated the effects of sudden changes in the magnetic field, *i.e.*, vortex density, on the relaxation processes of flux lines, and performed a systematic analysis to disentangle the contributions of the repulsive vortex-vortex interactions and pinning to the distinct point-like and columnar defects. We compared the cases when the magnetic field instantaneously increases or decreases to the situation when it stays fixed. We start with perfectly straight and randomly placed vortex lines and let the system relax for an extended relaxation time period, after which we maintain a fixed number of lines representing a constant magnetic field. Alternatively, we remove randomly selected lines from the initially relaxed vortices in the sample, or add perfectly straight new flux lines at random positions into the system of relaxed lines, to analyze the effects of a sudden decrease or increase in the magnetic field, respectively.

We validated our numerical studies by showing that our results for free, non-interacting vortex lines agree with the analytical predictions from the Edwards-Wilkinson interface growth model. We then introduced point-like and columnar pinning centers to a system of non-interacting flux lines. We found that the relaxation features in samples with columnar disorder are quite similar to the case when no disorder is present, especially in the behavior of global observables, as *e.g.*, visible in the dynamical scaling of the vortex mean-square displacement. This similarity indicates that the dynamics of vortex lines in the presence of columnar disorder is strongly dominated by the still unattached lines in the system. In the three studied cases without vortex interactions, sudden removal of flux lines results in the remaining lines showing similar relaxation behavior to the situation with a fixed vortex density, as expected since caging effects due to the repulsive vortex-vortex interactions are absent. On the other hand, when additional lines are introduced to these systems, the initially existing lines and the added lines show quite distinct features in their relaxation dynamics.

Thereafter, we added the repulsive screened logarithmic interactions into our consideration of systems without disorder, with uncorrelated point-like, or with extended columnar defects. Sudden decreases in the magnetic field result in the remaining lines displaying relaxation properties that differ from the situation when the magnetic field stays fixed, which confirms that caging effects due to vortex-vortex interactions constitute a prominent factor that highly affects the results of sudden changes in the magnetic field. Collective interaction effects are markedly enhanced when accompanied with disorder following sudden increases in the magnetic field, where the relaxation properties of the added lines clearly depend on the type of pinning centers. Point-like disorder enhances transverse spatial vortex line fluctuations by binding each to many pinning centers at once in the vortex glass phase, while columnar defects pin entire flux lines and straighten them in the distinct Bose glass phase. It is worth noting that when comparing the novel results in this study to our earlier work in Ref. [37] with random initial conditions, we discovered improved dynamical scaling in the vortex mean-square displacement in all situations considered here. Consequently, the currently utilized more realistic initial conditions help the system to equilibrate faster and thus acquire universal features.

The goal of this study is to methodically work towards observables and protocols that can be realized in experiments, while simultaneously providing detailed theoretical insight into the non-equilibrium relaxation kinetics of disordered vortex matter. Due to the complex nature of interacting vortex lines in the presence of disorder, we need to carefully and systematically analyze the contributions of the different energetic contributions to fully understand this intriguingly complicated dynamical system, as well as assess the relevance of different initial configurations. Hence the implementation of temperature and magnetic field quenches in our numerical simulations constitutes a crucially important advance that should hopefully provide valuable insights for future experiments. Indeed, temperature or magnetic field quenches and the subsequent measurement of one-time observables and two-time correlation functions could be utilized to formulate experimental methods to characterize material samples by means of the observed fluctuation spectrum. In future work, we plan to extend our study to include the effects of driving currents on the transient properties of driven flux line systems [61], where relaxation towards non-equilibrium steady states will ensue in contrast to the presently analyzed relaxation towards thermal equilibrium. A more detailed understanding of relaxation processes and the origin of deviation from scaling requires identifying the characteristic length scales in the system and their temporal growth, which we hope to pursue through the analysis of space-time observables.

Part II

Relaxation Properties in Disordered Semiconductors

Chapter 7

Background and Motivation

The second part of this dissertation addresses non-trivial equilibrium properties and non-equilibrium relaxation dynamics of the Coulomb glass model in disordered semiconductors and the Bose glass model in type-II superconductors in the presence of extended linear defects. This study serves as an extension to our investigations in the first part that mainly highlighted the height fluctuations of flux lines in type-II superconductors, while the model described here allows for monitoring the structural rearrangements of flux lines in the accessible simulation time scales.

This chapter presents a non-technical introduction on the Coulomb glass model and the soft gap that forms in the density of states around the chemical potential. Furthermore, it describes the Bose glass model that is brought about by adapting the Coulomb glass model utilizing the long-range logarithmic repulsive vortex-vortex interactions.

7.1 Coulomb Glass

The Coulomb glass model was introduced by Efros and Shklovskii in 1974 [65] describing localized charge carriers exposed to pinning defect centers in amorphous or doped crystalline semiconductors [65–67]. Since this model assumes that the localization length of charge carriers ξ is of the same order or smaller than the mean separation a_0 between acceptor and donor sites, the carriers can be described in classical terms to be confined to randomly distributed sites. Furthermore, the charge carriers rearrange themselves to minimize the total interaction energy and thus reach thermal equilibrium at low temperatures. The carrier distribution rearrangements occur by variable-range hopping which is influenced by the phonon-assisted quantum tunneling between the acceptor and donor sites and thermally-induced jumps over energy barriers.

Efros and Shklovskii argued that the Coulomb interaction between charge carriers causes the

system's density of states to display a soft gap near the chemical potential. This gap affects the charge carriers transport in the system and subsequently lowers the conductivity. Monte Carlo simulations performed on this model confirmed the existence of the Coulomb gap [68]. While Efros and Shklovskii predicted that the density of states near the gap follows a power law [65], Möbius; Richter; and Drittler proved the existence of deviations from the predicted mean-field results [69].

Experimental analysis of a two-dimensional silicon sample revealed non-trivial non-equilibrium relaxation properties: Jaroszynski and Popović drove the system out of equilibrium by altering the gate voltage and monitored the conductivity relaxation. They discovered that the relaxation rate of the sample depended on the waiting time [70, 71] before performing any measurements; this served as evidence for physical aging effects in such systems. Furthermore, Grempel *et al.* [72] found in their simulations of such samples that the autocorrelation function measurements for different waiting times can collapse onto a master curve for various temperatures; an evidence of aging effects and specifically dynamical scaling.

7.2 Bose Glass

As discussed in the first part of this dissertation, the most desirable property of type-II superconductors is the zero dissipation in current flow, hence one has to prevent vortex motion due to externally applied currents to eliminate the resulting Ohmic resistance and hence restore the desirable dissipative-free property. Optimal pinning mechanisms are utilized in these materials to prevent flux flow in the presence of applied currents. Among the different pinning configurations used, columnar defects have experimentally proven to be more efficient than uncorrelated point-like disorder [24]. At low temperatures, magnetic flux lines become attached to the entire length of these linear pinning sites. This results in the emergence of the strongly pinned *Bose glass phase* [13, 20–23] due to the localization of flux lines to these defect sites. The Bose glass phase in type-II superconductors and the Coulomb glass model in semiconductors share many similarities [20, 23, 32, 73, 74].

The Bose glass can be mapped to the Coulomb glass by considering the magnetic flux lines localized to the columnar defects as particles pinned to point defects in a two-dimensional plane. The flux line becomes the world line of the boson, with the original z direction mapping to an imaginary time axis. Furthermore, the flux line's elasticity constant maps to the boson particle's mass; the Bose glass' ambient temperature maps to $\hbar$; and thus the Bose glass' thickness is mapped to $\hbar/T$, which in turn implies that a finite thickness is mapped to a finite temperature [74].

The interacting flux lines in the Bose glass "hop" from their occupied defect sites to surrounding unoccupied sites. This leads to the formation of double-kinks or "superkink" excitations which are tongue-like double-kinks, each extending from one pinning site to another with a nearly equal energy [20, 23]. Therefore, flux lines are not required to hop to nearest neigh-

boring defect sites, which is similar to the variable-range hopping feature in the Coulomb glass.

Due to the remarkable similarities between the Coulomb and Bose glasses and the resulting mapping described above, one expects the Bose glass to display similar properties to those in the Coulomb glass. Analogous to the Coulomb glass, the Bose glass is composed of long-range interacting "particles" and spatial disorder, and hence this model's density of states was confirmed to similarly display a soft gap [73, 74], and the non-equilibrium relaxation dynamics display intriguing and rich aging and scaling properties [75, 76].

7.3 Overview

Chapter 8 provides a theoretical background on the Coulomb glass model in disordered semiconductors and the Bose glass model in type-II superconductors in the presence of extended linear defects. This theoretical chapter also discusses the Coulomb gap that forms in the density of states near the chemical potential due to the interaction-induced correlations. Chapter 9 presents an overview of the model we employ and the Monte Carlo algorithm we utilize to carry out our numerical investigations. Furthermore, it describes the simulation protocol we perform, specifies the material parameter values we use, and presents the quantities we measure to analyze the system's equilibrium properties and non-equilibrium and aging properties.

Chapter 10 demonstrates the effects of adding non-zero random on-site energies on the equilibrium and non-equilibrium relaxation properties in the Coulomb and Bose glass models. Chapter 11 analyzes the effects of sudden changes in the density of charge carriers in the Coulomb glass model or magnetic flux lines in the Bose glass model on the density of states properties and the non-equilibrium relaxation dynamics.

Chapter 8

Theoretical Background

This chapter provides a brief theoretical introduction that is needed for our numerical work in the next chapters. Section 8.1 introduces the Coulomb glass model in disordered semiconductors with the corresponding system's Hamiltonian. Subsequently, section 8.2 addresses the Coulomb gap that forms due to the interaction-induced correlations and the resulting gap exponent. In section 8.3, we adapt this model utilizing a logarithmic interaction to address the Bose glass model in type-II superconductors with columnar disorder. We end this chapter with a brief non-technical discussion of the effects of the Coulomb gap formation on both the Coulomb and Bose glass models.

8.1 Coulomb Glass Model

The Coulomb glass model was introduced by Efros and Shklovskii in 1974 [65] to describe localized charge carriers exposed to pinning defect centers in amorphous or doped crystalline semiconductors [65–67]. Since this model assumes that the localization length of charge carriers ξ is of the same order or smaller than the mean separation a_0 between acceptor and donor sites, the carriers are said to be confined to the randomly distributed sites. Furthermore, the carriers rearrange themselves to minimize the total interaction energy and thus reach thermal equilibrium at low temperatures. The carrier distribution rearrangements occur by variable-range hopping which is influenced by the phonon-assisted quantum tunneling between the acceptor and donor sites and thermally-induced jumps over energy barriers.

The system's Hamiltonian is given by [65–67]

$$H = \sum_i n_i \varphi_i + \frac{e^2}{2\kappa} \sum_{i \neq j} \frac{(n_i - K)(n_j - K)}{|\mathbf{R}_i - \mathbf{R}_j|}\,, \tag{8.1}$$

where e is the electron's charge, κ is the dielectric constant, and $\mathbf{R}_i$ and n_i respectively denote the position vector and occupancy of site i ($i = 1, ..., N$ with N being the total number of defect sites). φ_i represents the ith site's bare site energy, and thus the first term in (8.1) quantifies the random site energies assigned to each site accessible to carriers. On the other hand, the second term in (8.1) corresponds to the repulsive Coulomb interactions. A uniform relative charge density

$$K = \sum_i \frac{n_i}{N} \tag{8.2}$$

is introduced to maintain global charge neutrality, where K is equal to the total carrier density per site or the system's filling fraction. When we consider cases with all on-site energies $\varphi_i = 0$, the respective system's Hamiltonian in (8.1) is characterized by particle-hole symmetry: $K = 0.5 + k$ and $K = 0.5 - k$ are equivalent.

Therefore, the energy difference between two sites ΔE_{ij} is

$$\Delta E_{ij} = \epsilon_j - \epsilon_i - \frac{e^2}{\kappa R_{ij}}\,, \tag{8.3}$$

with the interacting site energies

$$\epsilon_i = \varphi_i + \frac{e^2}{\kappa} \sum_{j \neq i} \frac{n_j - K}{R_{ij}}\,. \tag{8.4}$$

It is worth noting that if we replace the sites occupation numbers with the Ising spin variables $\sigma_i = 2n_i - 1 = \pm 1$, the Coulomb glass model would map into the random-site, random-field antiferromagnetic Ising model with long-range exchange interactions [68].

Efros and Shklovskii [66] noted that the strong anticorrelations stemming from the long-range repulsive Coulomb forces create a soft gap in the density of states (DOS). This gap occurs near the chemical potential μ_c which separates low-energy ($\epsilon < \mu_c$) filled states and higher-energy ($\epsilon > \mu_c$) empty states. In section 8.2, we summarize Efros and Shklovskii's argument for the formation of this gap and we highlight the gap's properties and the effects it implicates.

8.2 Coulomb Gap

8.2.1 Gap Formation

Efros and Shklovskii [66] introduced a self-consistent argument for the depletion that forms in the distribution function $g(\epsilon)$ of site energies at the chemical potential:

At temperature $T = 0$ and in equilibrium, the transfer energy from site a to site b (in dimensionless units) is

$$\Delta E_{ab} = \epsilon_b - \epsilon_a - \frac{1}{R_{ab}} > 0\,, \tag{8.5}$$

where ϵ_a is the energy of charge carrier at site a and R_{ab} is the separation distance between sites a and b. The inequality in (8.5) indicates that the hop is supposed to increase the system's energy since the system is in equilibrium.

Furthermore, assuming that the DOS at the chemical potential is finite $g(\mu_c) = g_0$, they only consider site energies within a small width ϵ from the chemical potential, i.e. $\epsilon_b - \epsilon_a < 2\epsilon$. The number of sites in this energy interval is

$$N = 2\epsilon g(\mu_c)\,. \tag{8.6}$$

Considering two nearby sites with the same energy interval as above, one occupied site a and another unoccupied site b separated by $R_{ab} \sim (V/N)^{1/d}$ (where N is the total number of sites, V and d are the sample's volume and dimensionality respectively), the inequality in (8.5) becomes

$$\epsilon_b - \epsilon_a - A\left(\frac{\epsilon g(\mu_c)}{V}\right)^{1/d} > 0\,, \tag{8.7}$$

where A is a constant of proportionality, and hence the inequality is reduced to

$$A\left(\frac{\epsilon g(\mu_c)}{V}\right)^{1/d} < 2\epsilon\,. \tag{8.8}$$

Noting again that ϵ is an arbitrary value, we conclude that (8.8) can be violated with a small enough value of ϵ. Given that the only assumption made was that the DOS at the chemical potential $g(\mu_c)$ is finite, this contradiction implies that $g(\mu_c) = 0$ and therefore a gap in the DOS forms.

It is worth noting that even though the systems investigated in the current study are neither at temperature $T = 0$ nor in equilibrium, the Coulomb gap still appears and is very pronounced. The only difference is that non-zero temperatures have the effect of "washing out" or reducing the suppression of the Coulomb gap.

8.2.2 Gap Exponent

An important feature of the Coulomb gap (in systems with potentials $\Phi \propto r^{-\sigma}$, where $r \geq 1$) to study is the asymptotic behavior of the DOS near the chemical potential $g(\epsilon \to \mu_c)$. In the vicinity of μ_c, the DOS follows a power law $g(\epsilon) \sim |\epsilon - \mu_c|^\gamma$ for $\sigma < d$ [65–69,77–82] where γ is the "*gap exponent*". This can be confirmed by the following mean-field argument [66,73]:

First, lets generalize the potential to an arbitrary potential $\Phi(R_{ab})$, hence (8.5) becomes

$$\Delta E_{ab} = \epsilon_b - \epsilon_a - \Phi(R_{ab}) > 0\,, \tag{8.9}$$

and lets again only consider sites within energy interval ϵ around the chemical potential, i.e. $\Phi(R_{ab}) < \epsilon_b - \epsilon_a < 2\epsilon$.

Energetically favorable hops would occur between sites separated by distance

$$R_{ab} \propto \tilde{\Phi}(\epsilon)\,, \tag{8.10}$$

with $\tilde{\Phi}(\epsilon) = \Phi^{-1}(\epsilon)$. The number of sites that are in this favorable interval is thus given by

$$n = \frac{N}{V} \propto R_{ab}^{-d}\,. \tag{8.11}$$

Since ϵ is chosen to be a small value, one can obtain the density of states by computing $g(\epsilon) \propto dn/d\epsilon$ and therefore

$$g(\epsilon) = A \frac{|\tilde{\Phi}'(x)|}{\tilde{\Phi}(x)^{d+1}}\bigg|_{x=\epsilon}\,, \tag{8.12}$$

where $\Phi'(x) = d\Phi(x)/dx$ and A is a constant of proportionality that absorbs constants from the derivative.

Given a long-range repulsive potential of the form

$$\Phi(R_{ab}) \sim R_{ab}^{-1}, \tag{8.13}$$

equation (8.12) implies that the gap exponent according to mean-field considerations is

$$\gamma = d - 1\,. \tag{8.14}$$

The preceding mean-field argument assumes single-particle hops and that all sites are evenly distributed within the energy interval ϵ, whereas multi-particle hops play an important role in the system and sites often cluster [68]. Therefore, (8.14) represents a lower bound for γ beyond mean-field theory [83].

8.3 Bose Glass Model

The Coulomb glass model with the $1/r$ potential was adapted by replacing the Coulomb potential with a logarithmic potential to access the static and dynamical properties of flux creep in type-II superconductors with extended linear disorder [23]. These correlated defects that are aligned in the magnetic field's direction serve as pinning centers for fluctuating magnetic flux lines. At low temperatures and sufficiently low driving currents J, the magnetic flux lines undergo a continuous localization transition [20, 21] producing the so-called localized Bose Glass phase.

In the Bose glass phase, pinned flux lines are straight and parallel and thus the system can be mapped into a two-dimensional plane that is composed of "particles" pinned to point defects. Furthermore, magnetic vortex lines transport between columnar pinning sites analogously to the variable-range hopping through the formation and thereafter decay of double-kinks between different sites [73].

8.3.1 Logarithmic Potential Adaptation

The Coulomb glass model above can be adapted to describe the low-temperature properties of magnetic flux lines in type-II superconductors in the presence of strong correlated columnar disorder [23,73,74]. These magnetic vortices become localized at the material's linear defects

in the Bose glass phase and subsequently thermal transverse fluctuations are suppressed. Therefore, the three-dimensional system becomes essentially two-dimensional by considering the cross-section of the superconductor where a pinning site is the location of the intersection of the superconductor's "slice" and a columnar defect. Therefore, the charge carriers in the Coulomb glass model are replaced with the magnetic flux lines pinned to columnar defects in the Bose glass model.

The mutual repulsive Coulomb interaction between two occupied sites is now replaced with a modified Bessel function

$$V(r) = 2\epsilon_0 K_0(r/\lambda)\,, \tag{8.15}$$

which is essentially a long-range logarithmic potential screened on the London penetration length λ. The Bose glass model's Hamiltonian is then

$$H = \sum_i n_i\varphi_i + \epsilon_0 \sum_{i\neq j}(n_i - K)(n_j - K)K_0\left(\frac{|\mathbf{R}_i - \mathbf{R}_j|}{\lambda}\right), \tag{8.16}$$

where $\epsilon_0 = (\phi/4\pi\lambda)^2$ represents the system's energy scale with the magnetic flux quantum $\phi = hc/2e$. In the current study, we only consider a dilute low-magnetic field regime where all distances between sites are $R_{ij} = |\mathbf{R}_i - \mathbf{R}_j| \ll \lambda$ and thus $K_0(x) \propto -\ln(x)$.

Therefore, the energy difference between two sites in the Bose glass model ΔE_{ij} is

$$\Delta E_{ij} = \epsilon_j - \epsilon_i - 2\epsilon_0 K_0\left(\frac{R_{ij}}{\lambda}\right), \tag{8.17}$$

with the interacting site energies

$$\epsilon_i = \varphi_i + 2\epsilon_0 \sum_{j\neq i}(n_j - K)K_0\left(\frac{R_{ij}}{\lambda}\right), \tag{8.18}$$

where (similar to the Coulomb glass model) φ_i and n_i respectively denote the ith site random on-site energy and occupation number, and K is the total vortex density per site.

The long-range repulsive vortex-vortex interactions in the Bose glass model produce a soft gap in the density of states, similar to that observed in the Coulomb glass model. In both models, the soft Coulomb gap in the DOS brings about significant effects on the respective system's properties.

8.4 Coulomb Gap Effects

1. **Coulomb Glass**

   The existence of the correlation-induced Coulomb gap in the DOS significantly impedes the charge carrier mobility [65] effectively lowering the conductivity: The gap exponent γ alters the temperature dependence of the conductivity and the system's variable-range hopping length. In d dimensions, the conductivity scales as $\sigma \sim \exp(-T^{-p})$ where

   $$p(\gamma) = \frac{\gamma + 1}{\gamma + d + 1} \tag{8.19}$$

   in the thermally-induced transport regime at low temperatures T. For a constant DOS, $\gamma = 0$ and thus one recovers the Mott's variable-range hopping exponent $p = 1/4$ in three dimensions and $p = 1/3$ in two dimensions. However, in the presence of the Coulomb gap, (8.14) would give a larger p: $p = 1/2$ in three and two dimensions, confirming that the Coulomb gap effectively lowers the low-temperature conductivity.

2. **Bose Glass**

   Similar to the impeded transport of charge carriers in the Coulomb glass model, the Coulomb gap in the Bose glass model strongly suppresses flux creep. The impeded flux transport hence leads to the very favorable effect of a reduced resistivity $\rho \sim \exp(-J^{-p}/T)$ [73].

Chapter 9

Model and Simulation/Algorithm Description

We employ Monte Carlo (MC) simulations to investigate the Coulomb glass model in disordered semiconductors and the Bose glass model in type-II superconductors with correlated columnar defects. Chapter 8 describes both models in detail, while this chapter specifies the MC algorithm we utilized to study both models; the system parameters we considered; and the quantities we measured.

9.1 Model Description

Monte Carlo simulations are utilized to study the Coulomb and Bose glass models in $d = 2$ dimensions. The simulation system is initiated by randomly placing N pinning defect sites within a square lattice and charge carriers/flux lines occupy KN sites. The site occupancy is restricted to $n_i = 0$ or 1 due to the strong intra-site correlations. An example of the layout in one of our simulations is displayed in fig. 9.1.

Then, charge carriers/flux lines attempt to hop from their corresponding occupied sites to unoccupied sites. The transition rate from site a to site b is determined by

$$\Gamma_{ab} = \tau_0^{-1} e^{-2R_{ab}/\xi} \min[1, e^{-\Delta E_{ab}/k_B T}] \,, \tag{9.1}$$

where τ_0 denotes a microscopic time scale, $R_{ab} = |\mathbf{R}_b - \mathbf{R}_a|$ is the distance between the two sites, ξ represents the spatial extension of the charge carrier wave function or thermal wandering of the magnetic flux lines, ΔE_{ab} given by (8.3) for the Coulomb glass model or (8.17) for the Bose glass model is the difference between the energies of the two sites in question. Therefore, the success of hops is determined by two factors in (9.1):

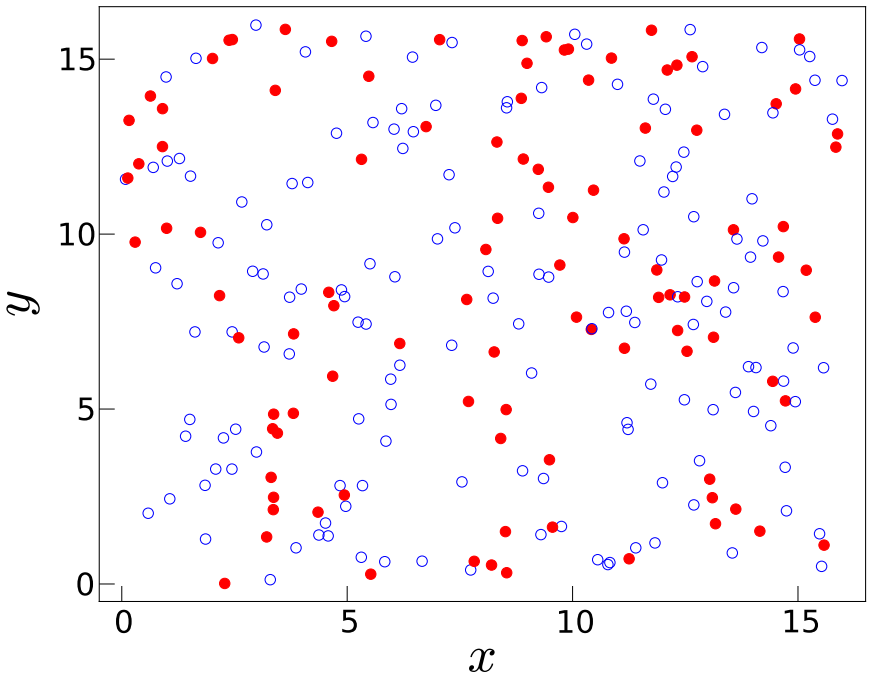

Figure 9.1: An example layout in one of our simulations of the two-dimensional Coulomb glass. Open circles denote unoccupied pinning sites and filled circles denote occupied sites.

- An exponential term describing the strongly distance-dependent phonon-mediated tunneling in semiconductors, and vortex superkink proliferation in type-II superconductors.
- A Metropolis term describing thermally-activated jumps through energy barriers.

9.2 Monte Carlo Algorithm

One Monte Carlo (MC) time step in our simulations occurs as following:

1. Choose a random occupied defect site a.
2. Choose a random unoccupied defect site b with probability $r_1 = e^{-2R_{ab}/\xi}$.
3. Pick a random number $0 \leq r_2 \leq 1$, and only accept site b if $r_2 < r_1$.
4. Pick a random number $0 \leq r_3 \leq 1$, and attempt a charge carrier hopping from a to b. The probability of the transition success is given by the Metropolis term, $r_4 = \min[1, e^{-\Delta E_{ab}/T}])$.

5. Move the charge carrier from defect site a to site b if $r_3 < r_4$. If the hopping attempt fails, return to the first step.

9.3 Simulation Description

9.3.1 Simulation Protocol

The first system we study as a continuation to the work in Refs. [75, 76] is the initial high temperature quench with completely random initial conditions. The simulation lattice with the corresponding number of defect sites and carriers is prepared, and the system relaxes for a sufficiently long initial relaxation time for both models.

The second system we consider involves an abrupt change in the number of charge carriers, where carriers are randomly added or removed from the sample. This serves as an attempt to bridge our computational work with experimental research and to better understand the system's sensitivity to the choice of initial conditions. For this part, we let the system relax for a long time beyond any microscopic time scale τ_0. At $t = 5 \times 10^4$ MCS, the number of charge carriers is instantaneously increased from $K = 0.5$ to $K_{final} = 0.54$ or lowered from $K = 0.5$ to $K_{final} = 0.46$. Then, we let the resulting system relax up to a waiting time s measured after the quench. A snapshot of the system is taken at s and the two-time correlation function defined in section (9.3.3) is measured at later times $t > s$. A similar study of flux line density quenches is performed to extend our investigation in the first part of this dissertation to analyze structural rearrangements of flux lines in the Bose glass phase.

9.3.2 System Parameters

All simulation distances are measured in units of the average distance between neighboring defect sites $a_0 = 1$. Simulation energies in the Coulomb glass model are measured in units of the typical Coulomb energy $E_C = e^2/\kappa a_0$, whereas energies in the Bose glass model are in units of $E_{bose} = 2\epsilon_0 K_0(a_0/\lambda)$.

The spatial extension of the charge carrier wave function is chosen to be $\xi = a_0$ [72, 84] following the careful investigation of different values of ξ in Ref. [75]. In the Bose glass model, the penetration length is set to $\lambda = 8a_0$.

We consider cases with zero random on-site energies ($\varphi = 0$) and others where the on-site energies are taken from a Gaussian or a flat distribution of zero mean and different widths w.

All other simulation parameters are chosen in accordance with the findings in Ref. [75], where:

- The simulation lattice length is $L = 16$, since the study of various lengths proved the absence of measurable finite-size effects.
- The system's ambient temperature is $T = 0.02$, since the temperature range that yields reasonable dynamics is $0.01 < T < 0.03$. The system's kinetics slowed down too much below $T = 0.01$ and no aging was observed above $T = 0.03$.
- The filling fraction is kept within the range $0.4 < K < 0.6$ since the dynamics in systems with filling fractions $K < 0.4$ or $K > 0.6$ freezes out in the accessible simulation time scales.

Periodic boundary conditions are utilized, and each simulation configuration shown was analyzed with 1000-6000 independent simulation runs.

9.3.3 Measured Quantities

The density of states $g(\epsilon)$, with the interacting site energies ϵ given by (8.4) for the Coulomb glass model and (8.18) for the Bose glass model, is measured by finding the number of sites that is located in each energy bin, with the bin size chosen as 0.01. We also study the soft gap that forms in the DOS and the speed of its formation over time given different simulation configurations. Mean-field calculations predict the DOS to display a power law near the chemical potential μ_C, which directs us to measure the gap exponent γ and compare it to the mean-field predictions.

The non-equilibrium relaxation dynamics and response to the high-temperature quench and the charge carrier/magnetic flux line density abrupt changes are analyzed using the two-time carrier density autocorrelation function

$$C(t,s) = \frac{\langle n_i(t) n_i(s) \rangle - K^2}{K(1-K)} = \frac{\sum_i n_i(t) n_i(s) - NK^2}{NK(1-K)}\,, \tag{9.2}$$

where $n_i(t)$ is the occupation number of defect site i at time t, s is the waiting time, N is the total number of defect sites, and K is the filling fraction. Furthermore, $\langle ... \rangle$ denotes an average over all sites, then an average is taken over many realizations.

Chapter 10

Random On-site Energy Effects

Via Monte Carlo simulations, we studied the emergence of the soft gap in the density of states (DOS) in the Coulomb and Bose glass models in two dimensions. We compared the gap's properties and non-equilibrium relaxation dynamics of systems without random on-site energies to those with on-site energies from different distributions. Section 10.1 discusses the effects of adding non-zero on-site energies on the density of states and the Coulomb gap's characteristics in the Coulomb and Bose glass models, while section 10.2 highlights such effects on the non-equilibrium relaxation dynamics and the aging scaling exponents.

10.1 Coulomb Gap Properties

10.1.1 Coulomb Glass Model

Gap Formation

We first investigated the Coulomb gap formation in the Coulomb glass model under random initial conditions without random on-site energies, where a fixed number of charge carriers is exposed to randomly distributed defect sites. In the following, there are $N = 256$ random sites available to $KN = 0.5 \times 256 = 128$ charge carriers. At the beginning of our simulations before any hops occur, the density of states displays the shape shown in fig. 10.1a. The DOS has a maximum at the chemical potential μ_c and it shows the system's initial distribution. At $t = 20$ MCS, a local minimum in the DOS already forms as a clear indication for the occupation of some low-energy states due to the charge carriers hopping between sites.

The DOS in fig. 10.1b is totally suppressed at the chemical potential μ_c and the Coulomb gap is pronounced. This confirms the occupation of the low-energy states by the present charge carriers, which is pictured by the peak located at $\epsilon \leq \mu_c$, and the separation of those

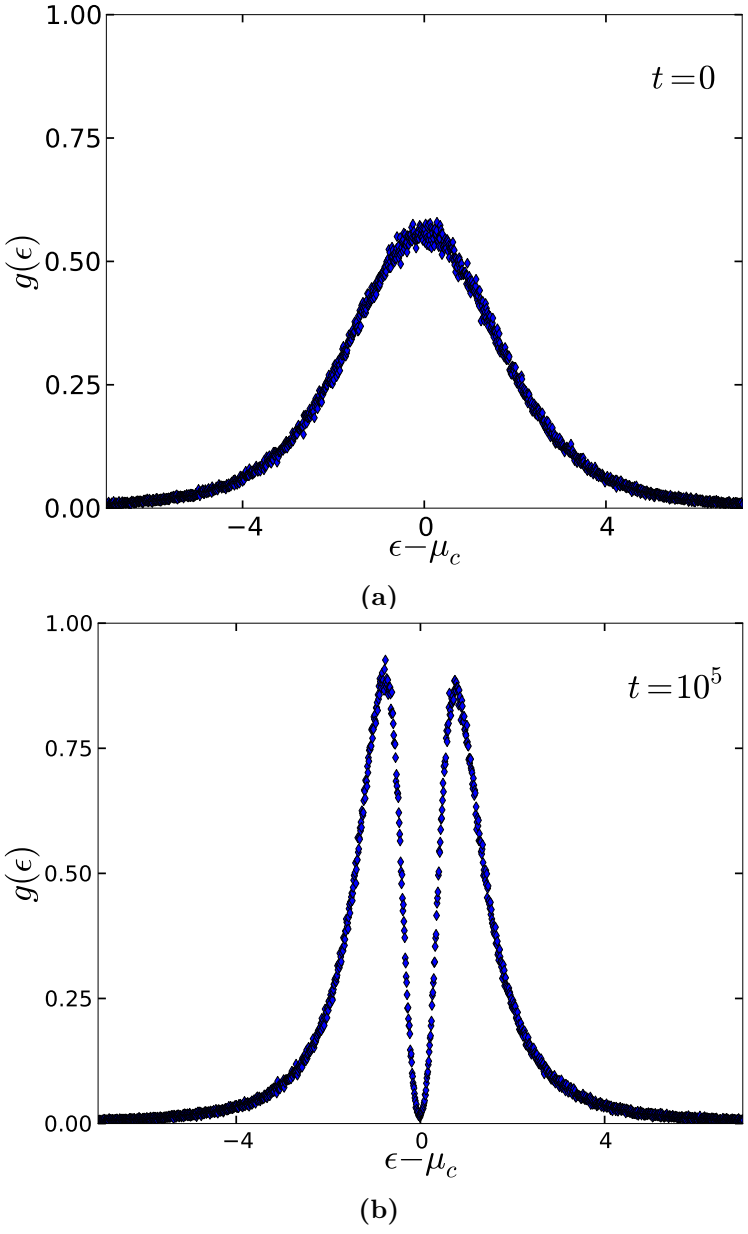

Figure 10.1: Density of states in the two-dimensional Coulomb glass model at (a) $t = 0$ MCS, and (b) $t = 10^5$ MCS in the absence of random on-site energies (data averaged over 6000 realizations).

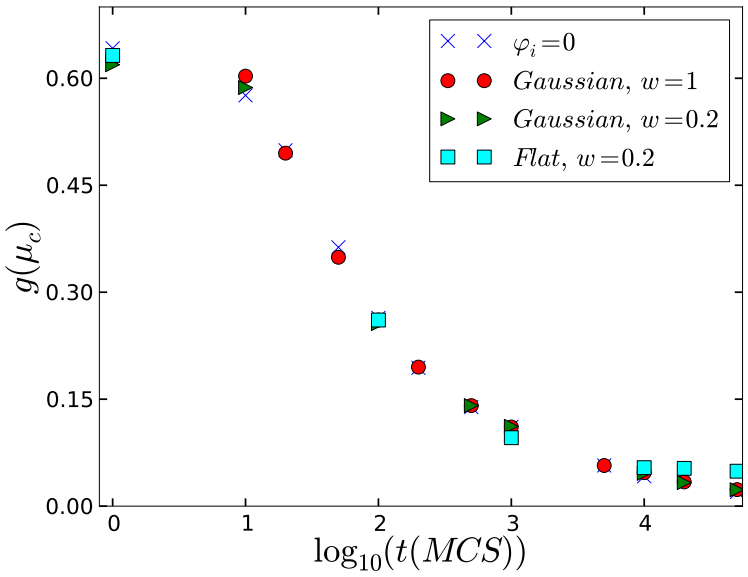

Figure 10.2: Relaxation of the density of states over time/ Coulomb gap formation in the two-dimensional Coulomb glass model in the presence of random on-site energies from different distributions (data averaged over 6000 realizations).

from the unoccupied higher-energy states at $\epsilon \geq \mu_c$.

Speed of Gap formation

We monitored the evolution of the DOS in time in the absence of on-site energies to gauge the effect of the inclusion of such energies on the speed of the gap's formation. To this end, we studied systems without on-site energies and others with random on-site energies chosen from a flat and a Gaussian distribution of different widths.

As discussed above and confirmed by fig. 10.2, the gap in the DOS starts to form within $t \sim 20$ MCS, and the value of $g(\mu_c)$ decreases as time progresses until a total suppression is (almost) observed. It is worth noticing that $g(\mu_c)$ is very close to zero, but not totally suppressed, in all the cases studied here of the two-dimensional Coulomb glass model. The three-dimensional system is proven in Refs. [75, 76] to display a faster total suppression of the Coulomb gap than the two-dimensional system.

Fig. 10.2 confirms that the inclusion of random on-site energies from a Gaussian distribution of different widths, here $w = 1$ and $w = 0.2$ are utilized, does not affect the speed of the gap's formation and it does not affect the suppression of the DOS at the chemical potential at long times. On the other hand, one observes that on-site energies from a flat distribution of zero mean and width $w = 0.2$ might be slowing down the suppression of the DOS at μ_c.

To further analyze the effects of energies from this flat distribution on the speed of the gap

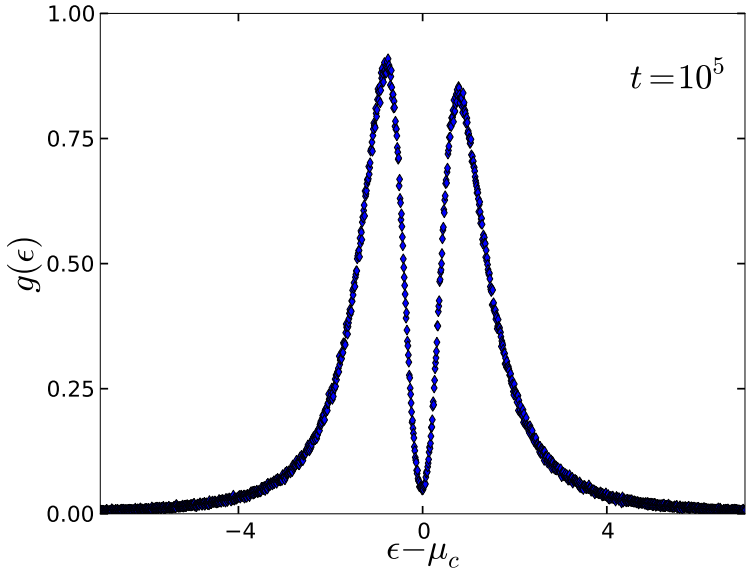

Figure 10.3: Density of states in the two-dimensional Coulomb glass model with random on-site energies from a flat distribution (zero mean, width $w = 0.2$) at $t = 10^5$ MCS (data averaged over 6000 realizations).

formation, we closely monitored the DOS evolution over time.

Comparing fig. 10.3 to fig. 10.1b without on-site energies at the same time ($t = 10^5$) asserts that on-site energies influence the arrangement of charge carriers and their pinning behavior to the present defect sites, thereby eliminating the symmetry of the DOS around $\epsilon = \mu_c$ for half-filling and more importantly delaying the time of the total suppression of the DOS at $\epsilon = \mu_c$.

Gap Exponent

To better understand the effect of non-zero random on-site energies on the Coulomb gap, we studied the asymptotic behavior of the density of states near the chemical potential. As discussed in chapter 8, the DOS near the chemical potential diminishes via a power law $g(\epsilon) \sim |\epsilon - \mu_c|^\gamma$ for $\sigma < d$ [65–69,77–82], where γ is the gap exponent. Mean-field arguments compute the gap exponent as $\gamma = d - 1$ for the Coulomb repulsive interactions of the form $1/r$. This implies that the mean-field gap exponent for the Coulomb glass model in two dimensions is $\gamma = 1$.

We monitored the asymptotic behavior of the density of states near the chemical potential for the cases characterized by the absence and later presence of different on-site energies and observed that a power law behavior is displayed in the DOS near μ_c, shown in fig. 10.4.

As indicated in the legend of fig. 10.4, the computed effective gap exponent for the system

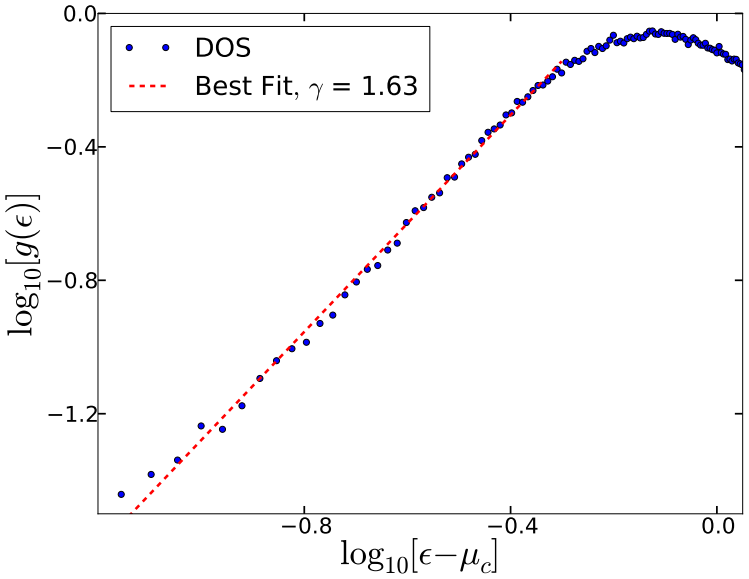

Figure 10.4: Logarithmic plot of the density of states in the two-dimensional Coulomb glass model at $t = 10^5$ MCS in the absence of random on-site energies. The dashed line represents the best power law fit (data averaged over 6000 realizations).

without random on-site energies is found to be $\gamma = 1.63$, which differs from the mean-field predicted $\gamma = 1$. As discussed in chapter 8, it is to be expected for the exponent computed in these simulations to be different from that predicted by mean-field arguments.

We computed the gap exponent in cases with different on-site energy distributions, and the values we found are summarized in table 10.1.

	(a) $\varphi_i = 0$	(b) Gaussian, $w = 1$	(c) Gaussian, $w = 0.2$	(d) Flat, $w = 0.2$
γ	1.63 ± 0.018	1.53 ± 0.014	1.74 ± 0.015	1.26 ± 0.019

Table 10.1: Measured Coulomb gap exponent γ for the two-dimensional Coulomb glass model (a) without random on-site energies, and in the presence of (b,c) Gaussian or (d) flat on-site energy distributions of different widths centered at zero. Exponents are computed from the best power law fit at $t = 10^5$ MCS (data averaged over 6000 realizations).

The Gaussian random on-site energy distribution does not noticeably affect the gap exponent, but the flat distribution energies have a more pronounced influence on the value of the computed exponent. Including random on-site energies from this flat distribution decreases the gap exponent and renders it closer to the mean-field predictions. Sharp energy distributions are less effective due to the interaction-induced correlations, and one obtains the same DOS results as in the case when $\varphi_i = 0$ (we confirmed this with flat and Gaussian distribu-

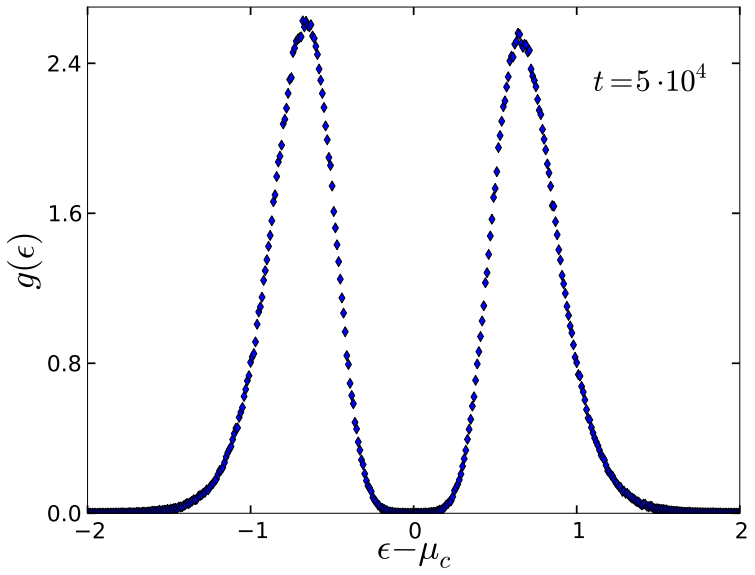

Figure 10.5: Density of states in the two-dimensional Bose glass model at $t = 5 \cdot 10^4$ MCS in the absence of random on-site energies (data averaged over 6000 realizations).

tions of zero mean and width $w = 0.001$). In contrast, broader distributions of widths on the same scale as the correlation-induced Coulomb gap's width have a more pronounced effect on the density of states around the chemical potential.

A lower effective gap exponent than the case without on-site energies implies a lower p (eq. 8.19), which in turn translates to an increased conductivity and thus charge carrier transport since conductivity scales as $\exp(-T^{-p})$.

10.1.2 Bose Glass Model

We similarly monitored the density of states in the Bose glass model in two dimensions and analyzed the Coulomb gap's properties that forms in this system. A very pronounced difference with the Coulomb glass model is that the Coulomb gap forms quicker and is suppressed faster, i.e. $g(\mu_c) = 0$ in less time, in about 50 MCS. The faster formation of the gap and its suppression at μ_c can be observed in fig. 10.5.

The Coulomb gap forms much faster and is broader than that displayed by systems with Coulomb repulsive interactions. Analyzing the evolution of $g(\mu_c)$ in time confirms this observation and the direct effect of the addition of random on-site energies from various distributions.

Speed of Gap formation

Comparing the speed of formation of the Coulomb gap in systems with logarithmic interaction displayed in fig. 10.6 to that in systems with Coulomb interactions in fig. 10.2 proves that the logarithmic interactions drive the gap to form much faster.

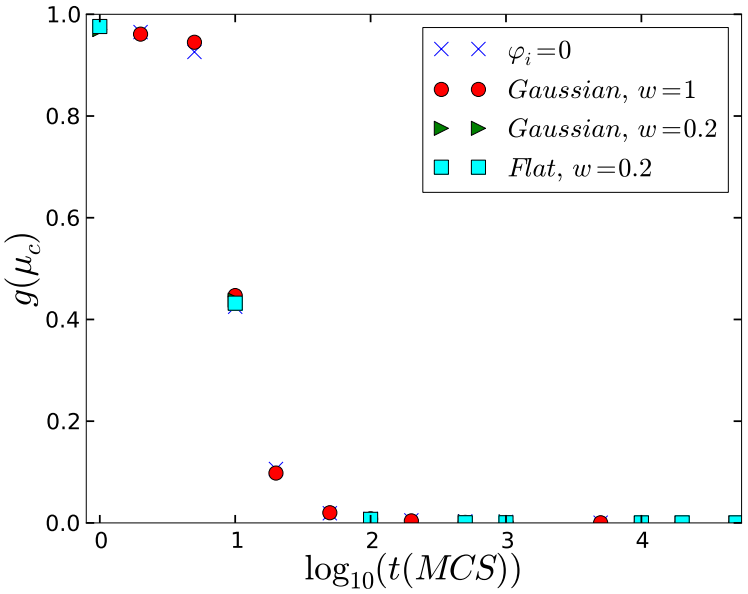

Figure 10.6: Relaxation of the density of states over time/ Coulomb gap formation in the two-dimensional Bose glass model in the presence of random on-site energies from different distributions (data averaged over 6000 realizations).

Aside from the faster formation of the gap, it is also strongly suppressed for systems without on-site energies and energies from flat and Gaussian distributions alike. Therefore, one concludes that the inclusion of on-site energies from different distributions does not change the overall properties and speed of formation of the gap in the Bose glass model, unlike our findings in the Coulomb glass model where energies from a flat distribution affect the suppression of $g(\mu_c)$.

Gap Exponent

To further investigate the effects of random on-site energies on the density of states in the Bose glass model, we checked for the power law fit and the gap exponent in this case. Similar to the Coulomb glass model in section 10.1.1, we observed that $g(\epsilon)$ follows a power law in the vicinity of the chemical potential μ_c.

However, the gap exponents computed in the Bose glass are greater than those in the Coulomb glass. One has to keep in mind that the suppressed motion within the Bose

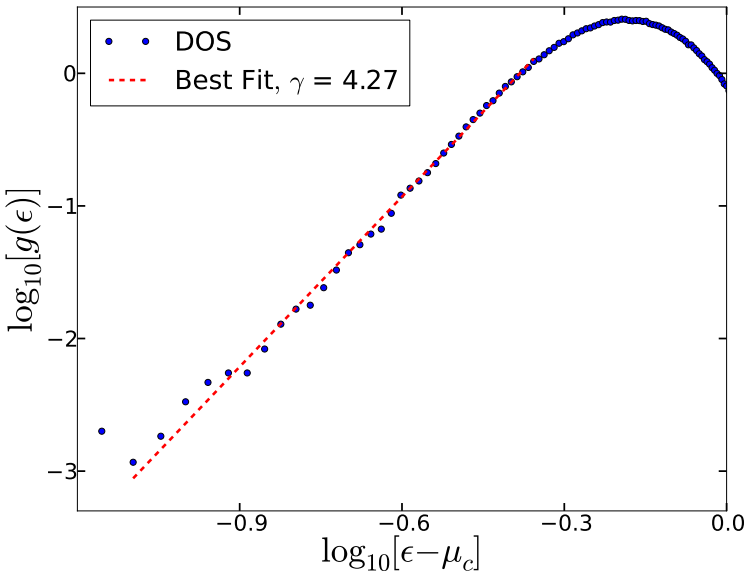

Figure 10.7: Logarithmic plot of the density of states in the two-dimensional Bose glass model at $t = 5 \cdot 10^4$ MCS in the absence of random on-site energies. The dashed line represents the best power law fit (data averaged over 6000 realizations).

glass model leads to a slower relaxation and thus a larger gap exponent. Calculating the gap exponent from the power law best fit allows us to study the influence of random on-site energies on the density of states aside from the speed of formation discussed above.

	(a) $\varphi_i = 0$	(b) Gaussian, $w = 1$	(c) Gaussian, $w = 0.2$	(d) Flat, $w = 0.2$
γ	4.27 ± 0.21	4.5 ± 0.21	4.47 ± 0.21	5.03 ± 0.22

Table 10.2: Measured Coulomb gap exponent γ for the two-dimensional Bose glass models (a) without random on-site energies, and in the presence of (b,c) Gaussian or (d) flat on-site energy distributions of different widths centered at zero. Exponents are computed from the best power law fit at $t = 5 \cdot 10^4$ MCS (data averaged over 6000 realizations).

Analogous to the Coulomb glass model studies, we proceeded to compute the Coulomb gap exponent from the power law best fit in the Bose glass system in the absence of any on-site energies and in the presence of random energies from a flat distribution of width $w = 0.2$ and a Gaussian distribution of widths $w = 0.2$ or $w = 1$. The summary of our findings is presented in table 10.2.

An important observation to make is that similar to the Coulomb glass model, on-site energies from a Gaussian distribution of different widths show a much weaker effect on the gap exponent than the flat distribution. The introduction of random on-site energies from the

utilized flat distribution increases the effective gap exponent rendering it closer to the infinite value that mean-field arguments predict in the Bose glass phase with localized magnetic flux lines and a suppressed flux creep.

10.2 Non-Equilibrium Relaxation Dynamics

In addition to our investigations of the effects of random on-site energies on the density of states; the Coulomb gap formation; and the effective gap exponent, we analyzed the corresponding effects on the non-equilibrium relaxation properties of the systems studied. Section 10.2.1 presents our findings for the Coulomb glass model in disordered semiconductors, and section 10.2.2 summarizes our results for the Bose glass model in type-II superconductors in the presence of extended linear defects.

10.2.1 Coulomb Glass Model

We start by studying the Coulomb glass model in two dimensions and investigating its non-equilibrium relaxation dynamics by measuring the two-time charge autocorrelation function $C(t, s)$ and its properties.

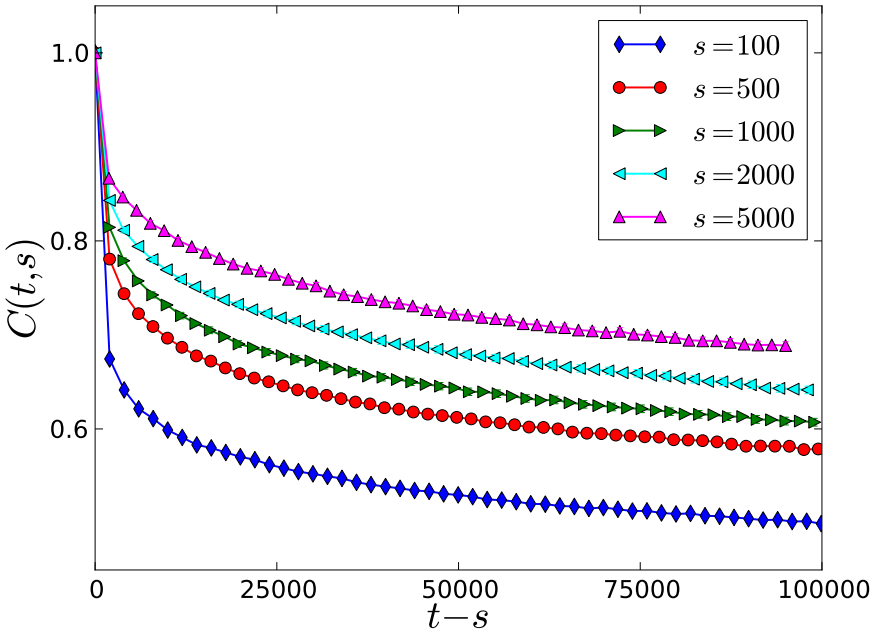

Figure 10.8: Relaxation of the two-time charge autocorrelation function in the two-dimensional Coulomb glass model in the absence of random on-site energies (data averaged over 3000 realizations).

In the absence of random on-site energies, the system shows slow dynamics and breaking of time translation invariance due to its still-sustained dependence on the waiting times, as seen in fig. 10.8. The slow relaxation of this system with Coulomb repulsive interactions is apparent in fig. 10.8 since the system has not reached a steady state even after 10^5 MCS. The system displays two different relaxation regimes, as shown in fig. 10.9.

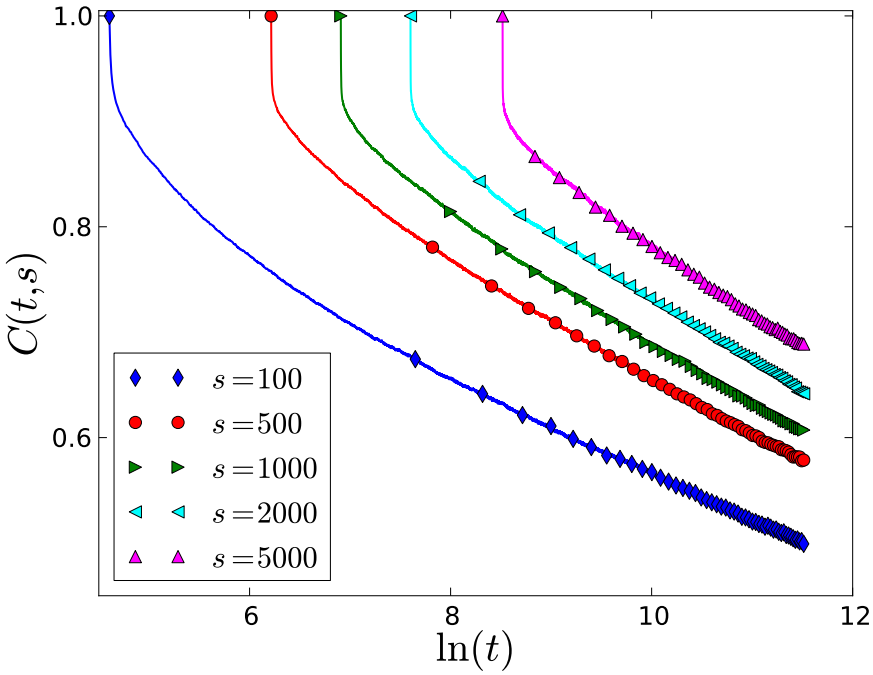

Figure 10.9: Relaxation of the two-time charge autocorrelation function in the two-dimensional Coulomb glass model in the absence of random on-site energies (data averaged over 3000 realizations).

The first regime is characterized by a fast relaxation produced by the vibrations of charge carriers around their initial positions and the carrier clusters group motion. On the other hand, the second regime displays a much slower relaxation that is dominated by the divisions of charge carrier clusters and the resulting relaxation of the system towards a steady state.

The breaking of time translation invariance that the system displays in fig. 10.8 implies that $C(t, s)$ depends on both the measurement time t and waiting time s. The slow dynamics and breaking of time translation invariance are two characteristics of *physical aging*, while the third property to be considered here is dynamical scaling.

As discussed earlier, we expect the charge autocorrelation function in the aging scaling regime to obey the general scaling form

$$C(t, s) = s^{-b} f_C(t/s)\,, \tag{10.1}$$

where b is an aging scaling exponent. When $t/s \to \infty$ in the case of simple aging, the scaling function f_C is a power law

$$f_C(t/s) \sim (t/s)^{-\lambda_C/z}\,, \tag{10.2}$$

where λ_C is an autocorrelation exponent, z is a dynamic exponent; and the ratio λ_C/z is an independent scaling exponent we investigate in our current study.

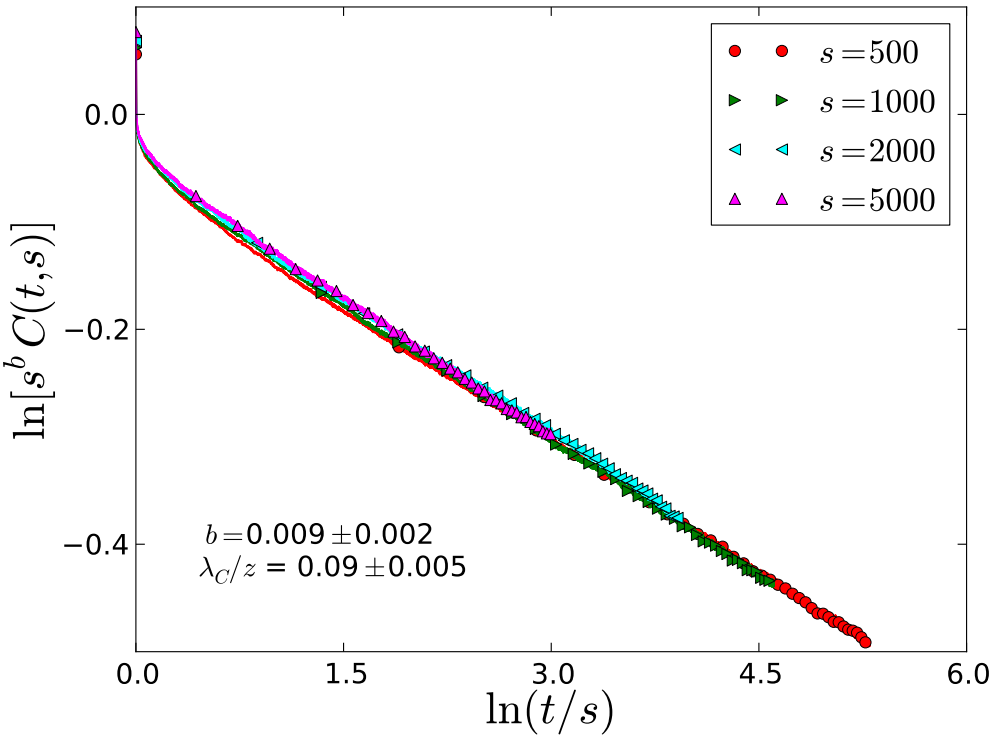

Figure 10.10: Relaxation of the two-time charge autocorrelation function in the two-dimensional Coulomb glass model in the absence of random on-site energies (data averaged over 3000 realizations).

Investigating the scaling exponents in this aging regime, we determined $b = 0.009$ and $\lambda_C/z = 0.09$ for the two-dimensional Coulomb glass model without on-site energies. The goal of this part is to compute these scaling exponents after the addition of on-site energies from different distributions and compare them to the above case. We focused on energies from flat and Gaussian distributions, and we present the measured scaling exponents in table 10.3.

From our results in table 10.3, we conclude that the addition of random on-site energies from a Gaussian distribution of different widths does not affect the aging scaling exponents. On the other hand, on-site energies from a flat distribution of width $w = 0.2$ highly influence both exponents, see fig. 10.11b. It is worth noting that the interaction-induced correlations slow down the relaxation of the systems studied, and the introduction of broad on-site energy distributions of widths on the same scale as the correlation-induced Coulomb gap's width drives the system to display an even slower relaxation dynamics, as confirmed by the higher λ_C/z value which implies a slower relaxation.

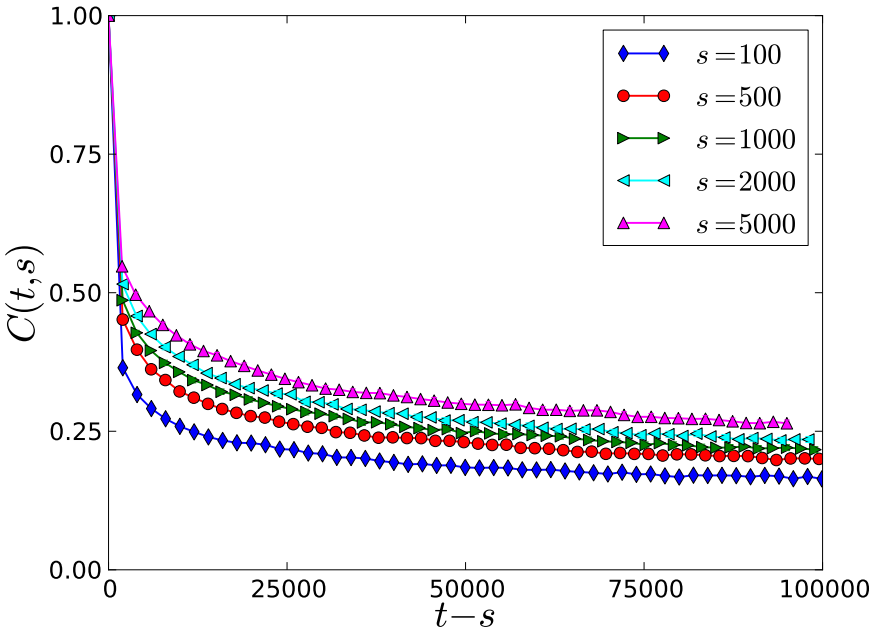

(a)

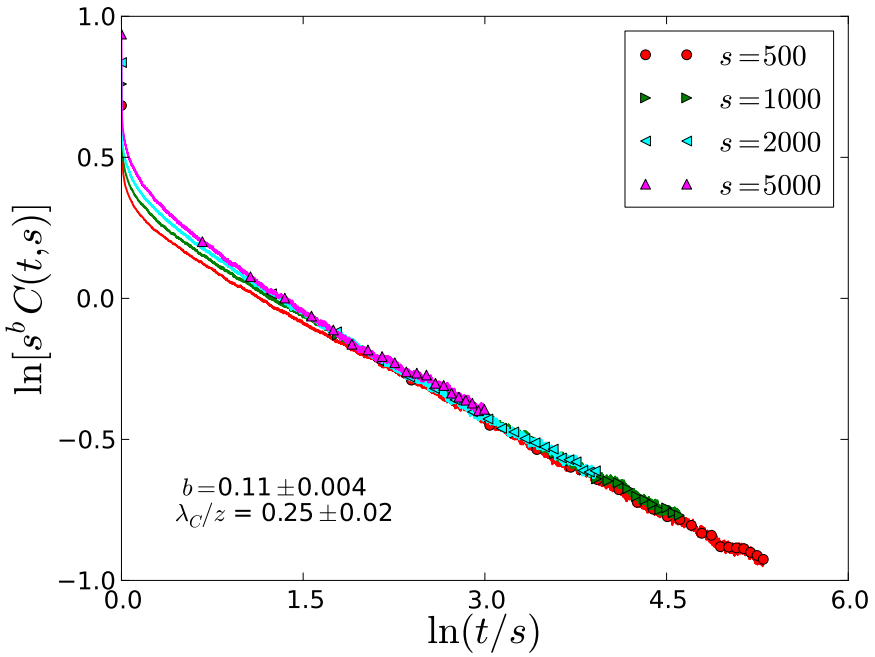

(b)

Figure 10.11: Relaxation of the two-time charge autocorrelation function in the two-dimensional Coulomb glass model with random on-site energies from a flat distribution (zero mean, width $w = 0.2$) (data averaged over 3000 realizations).

	(a) $\varphi_i = 0$	(b) Gaussian, $w = 1$	(c) Gaussian, $w = 0.2$	(d) Flat, $w = 0.2$
b	0.009 ± 0.002	0.006 ± 0.003	0.01 ± 0.002	0.11 ± 0.005
λ_C/z	0.09 ± 0.005	0.09 ± 0.005	0.09 ± 0.005	0.25 ± 0.02

Table 10.3: Measured scaling exponents b and λ_C/z for the two-dimensional Coulomb glass model (a) without random on-site energies, and in the presence of (b,c) Gaussian or (d) flat on-site energy distributions of different widths centered at zero (data averaged over 1000 realizations).

10.2.2 Bose Glass Model

A similar study of the non-equilibrium relaxation properties of the Bose glass model in two dimensions was performed, where we analyzed the effects of random on-site energies on the charge autocorrelation function and its scaling form and exponents.

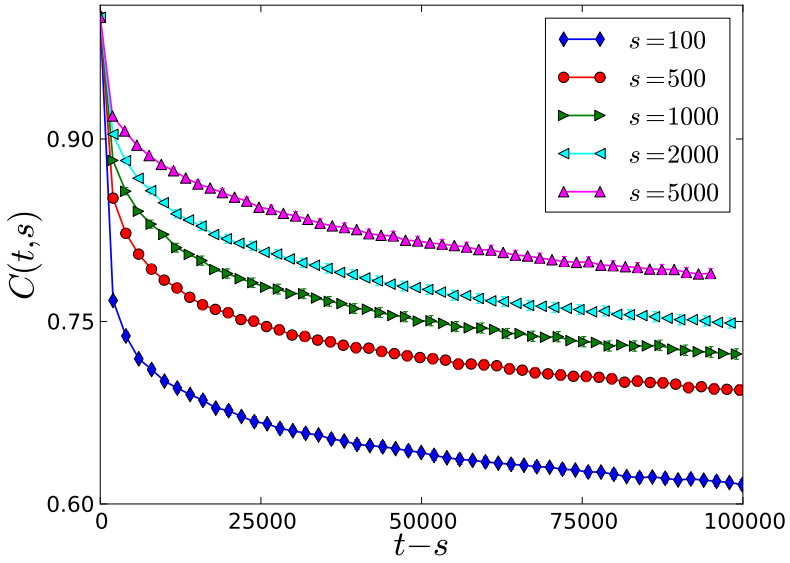

(a)

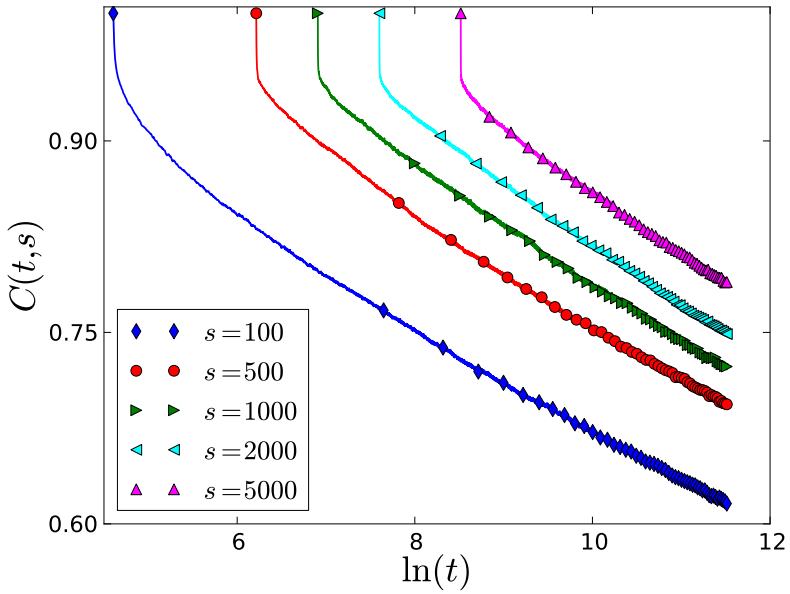

(b)

Figure 10.12: Relaxation of the two-time autocorrelation function in the two-dimensional Bose glass model in the absence of random on-site energies (data averaged over 3000 realizations).

Starting with the Bose glass model with zero on-site energies, slow dynamics is also a signature of such system, as seen in fig. 10.12a and fig. 10.12b, and the autocorrelation function $C(t, s)$ displays similar glassy dynamics to the Coulomb glass model in fig. 10.9.

Investigating the universality of scaling exponents, we study the simple aging scaling forms for the various on-site energy distributions.

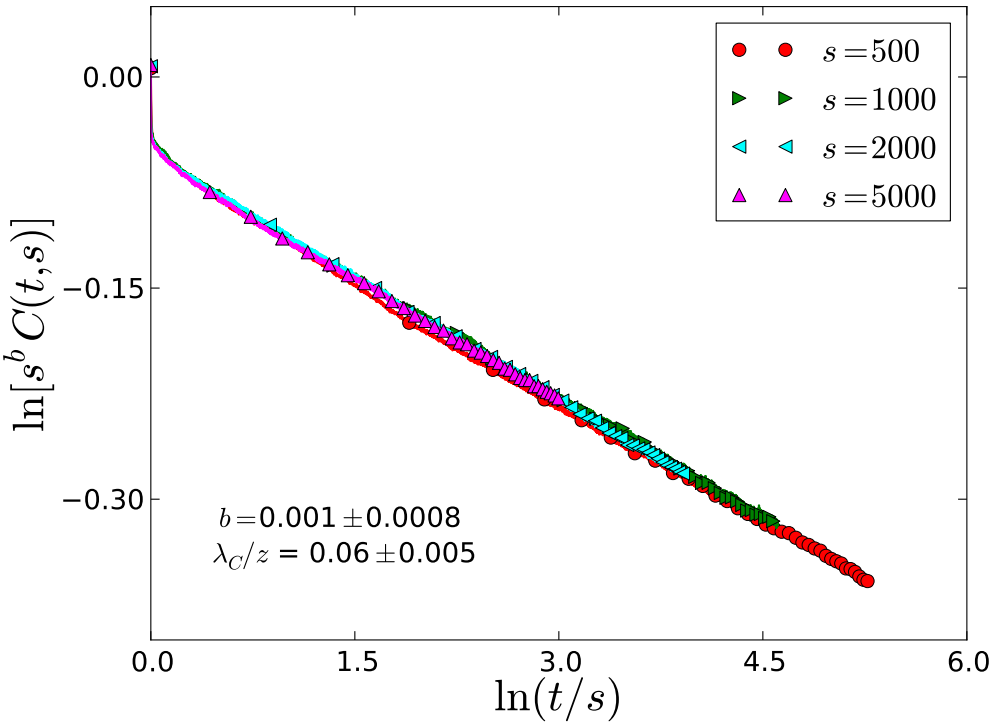

Figure 10.13: Relaxation of the two-time autocorrelation function in the two-dimensional Bose glass model in the absence of random on-site energies (data averaged over 3000 realizations).

Fig. 10.13 shows the scaling collapse with the aging scaling exponents that are computed for the two-dimensional Bose glass model with zero on-site energies. To study the effects of on-site energies on the system's non-equilibrium relaxation properties, we similarly investigate any discrepancies present between this case's scaling exponents and those in the cases with different energy distributions. The results are summarized in table 10.4.

Our results in table 10.4 confirm that adding random on-site energies from a Gaussian distribution of different widths has a minor effect on the scaling exponents b and λ_C/z, which implies that this addition has little effect on the relaxation dynamics of the Bose glass system with logarithmic interactions.

On the other hand, it is evident from fig. 10.14 that a flat on-site energy distribution of width $w = 0.2$ has a pronounced effect on the non-equilibrium relaxation properties of this

	(a) $\varphi_i = 0$	(b) Gaussian, $w = 1$	(c) Gaussian, $w = 0.2$	(d) Flat, $w = 0.2$
b	0.001 ± 0.0008	0.001 ± 0.0008	0.003 ± 0.002	0.035 ± 0.004
λ_C/z	0.06 ± 0.005	0.05 ± 0.005	0.06 ± 0.005	0.16 ± 0.02

Table 10.4: Measured scaling exponents b and λ_C/z for the two-dimensional Bose glass model (a) without random on-site energies, and in the presence of (b,c) Gaussian or (d) flat on-site energy distributions of different widths centered at zero (data averaged over 1000 realizations).

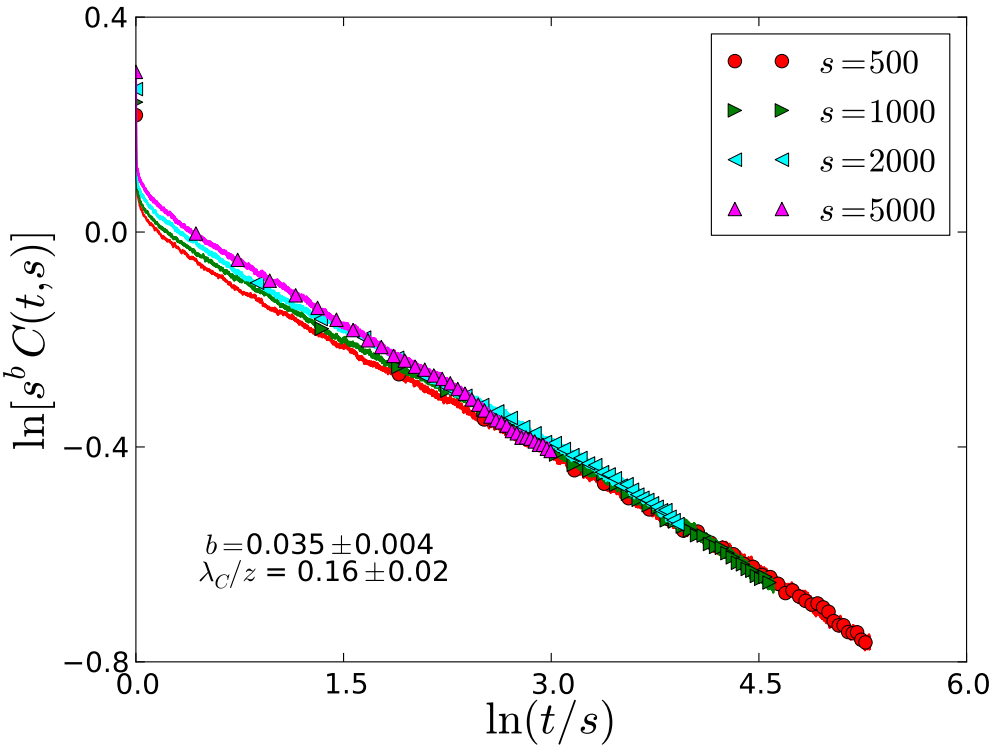

Figure 10.14: Relaxation of the two-time autocorrelation function in the two-dimensional Bose glass model with random on-site energies from a flat distribution (zero mean, width $w = 0.2$) (data averaged over 3000 realizations).

system. Both aging scaling exponents b and λ_C/z assumed considerably greater values as a response to the introduction of non-zero on-site energies from a flat distribution, which hence imposed a slower relaxation on the system, analogous to our results for the Coulomb glass model.

Chapter 11

Density Quench Effects

Earlier investigations focused on the Coulomb gap and non-equilibrium relaxation properties under random initial conditions [75, 76]. It is worthwhile to analyze the effect of abrupt changes in the density of charge carriers in the Coulomb glass model or analogously flux lines in type-II superconductors with linear defects on the Coulomb gap's properties and aging scaling exponents to probe the system's sensitivity to sudden changes in parameters and thus bridge our simulations with experimental work. We utilized Monte Carlo simulations to study the effects of density quenches on the Coulomb gap in section 11.1 and on the aging scaling behavior and exponents in section 11.2 in the absence of random on-site energies.

11.1 Coulomb Gap Properties

11.1.1 Coulomb Glass Model

In the Coulomb glass model in two dimensions, we investigate the effects of suddenly increasing the filling fraction from $K = 0.5$ to $K_{final} = 0.54$ (up-quench) or alternatively decreasing the filling fraction from $K = 0.5$ to $K_{final} = 0.46$ (down-quench) on the Coulomb gap and its evolution in time.

First, keeping the density of charge carriers fixed with the filling fraction $K = 0.5$ and letting the corresponding system relax in time for $t_{relax} = 5 \cdot 10^4$ until the Coulomb gap forms and is suppressed at the chemical potential μ_{c1} (this is when the simulation clock is reset to 0), we observe the DOS displayed in Fig. 11.1.

After confirming that the density of states displays a relaxed Coulomb gap, we perform the density quench. Discussing first the case of density up-quench and measuring the DOS, we have to keep in mind that the system is not at half-filling anymore but $K_{final} = 0.54$, which implies that we can expect a shift in the DOS as compared to the case with a fixed density.

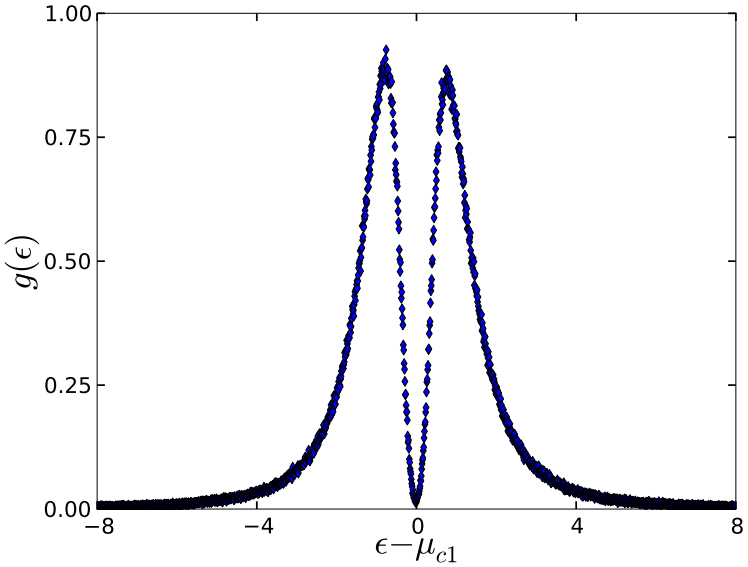

Figure 11.1: Density of states in the two-dimensional Coulomb glass model before the density quench occurs, after relaxing the system for $t_{relax} = 5 \cdot 10^4$ MCS. The equilibrated system's chemical potential is μ_{c1} (data averaged over 6000 realizations).

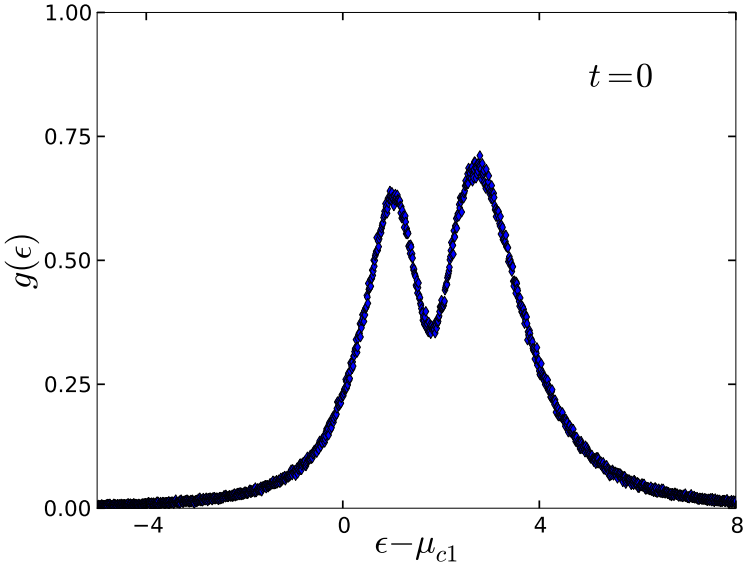

Figure 11.2: Density of states in the two-dimensional Coulomb glass model at $t = 0$ at the moment of suddenly increasing the filling fraction from $K = 0.5$ to $K_{final} = 0.54$. μ_{c1} is the the relaxed system's chemical potential before the quench (data averaged over 6000 realizations).

To test this expectation, we follow the DOS evolution in time.

At the moment of the charge carrier density up-quench, fig. 11.2 shows that the peak on the left denoting the lower-energy states reduces while the opposite peak increases. This occurs since new charge carriers are abruptly introduced to the system which in turn increases the typical Coulomb repulsion, and thus an enhanced peak on the higher-energy states initially emerges.

As the system relaxes away from this initial arrangement and into equilibrium, the new charge carriers start exploring the surrounding for pinning at the present defect sites, and the shape of the DOS starts changing within a few MCS to display a flip in the asymmetry displayed by the initial configuration in fig. 11.2, as can be observed in fig. 11.3.

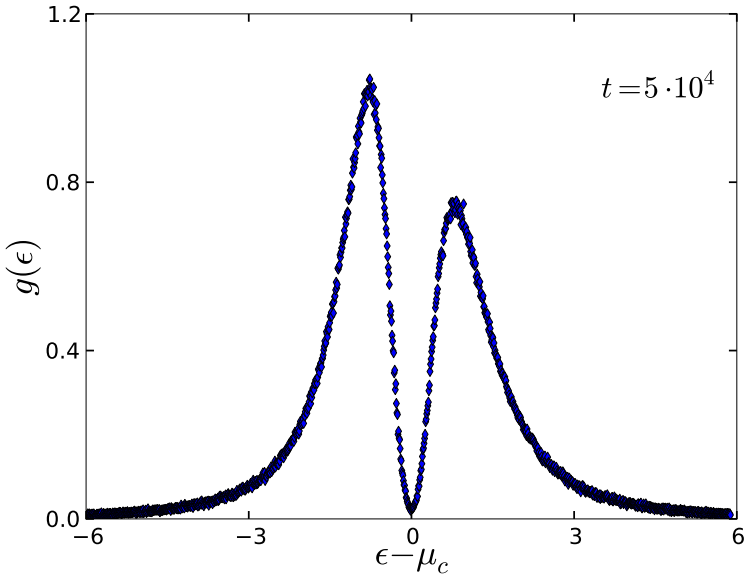

Figure 11.3: Density of states in the two-dimensional Coulomb glass model at $t = 5 \cdot 10^4$ MCS after a sudden increase in the filling fraction from $K = 0.5$ to $K_{final} = 0.54$. The equilibrated system's chemical potential after the quench is μ_c (data averaged over 6000 realizations).

Since $K_{final} \neq 0.5$ after the density quench, one expects the disappearance of the symmetry that characterizes the half-filling system. In the case of an abrupt increase in K away from half-filling, $\mu_c \neq \mu_{c1}$ is the new system's chemical potential after it equilibrates. More charge carriers are present to occupy the fixed number of defect sites, and therefore the peak on the occupied sites raises and the asymmetry is reversed from the initial configuration, as one concludes from comparing fig. 11.2 and fig. 11.3.

The case of density down-quench is similarly performed, where the filling fraction is abruptly lowered from $K = 0.5$ to $K_{final} = 0.46$. At the moment of the quench at $t = 0$, the peak at the lower energies is enhanced, which is expected due to the reduction in the number of

	(a) No density quench	(b) Density up-quench	(c) Density down-quench
γ	1.58 ± 0.018	1.56 ± 0.012	1.65 ± 0.007

Table 11.1: Measured Coulomb gap exponent γ for the two-dimensional Coulomb glass model when the filling fraction is (a) kept fixed at $K = 0.5$, (b) suddenly raised from $K = 0.5$ to $K_{final} = 0.54$, and (c) abruptly lowered from $K = 0.5$ to $K_{final} = 0.46$ at $t = 5 \cdot 10^4$ MCS (data averaged over 6000 realizations).

charge carriers which implies a decrease in the typical Coulomb repulsion. A similar but reversed asymmetry to that in fig. 11.3 appears at $t = 5 \cdot 10^4$ MCS after the quench. As the system relaxes, a smaller number of charge carriers occupies the present pinning defect sites, and hence the asymmetry is kept but reverses to show an increased peak at the unoccupied states.

Another property that can be utilized to investigate the effects of instantaneous density changes is the power law fit for the density of states in the vicinity of the chemical potential. We compute the effective gap exponent at the same time for the cases when the filling fraction is kept fixed at half or suddenly raised/lowered away from half-filling.

From table 11.1, one obtains the effective gap exponents for the three systems with different final filling fractions. It is worth noting that since the Coulomb gap exponent is an equilibrium property, one expects to obtain similar results when (a) starting from random initial conditions with filling fraction K_1 or (b) abruptly changing the filling fraction from K to K_1 and thereafter letting the system relax towards equilibrium.

11.1.2 Bose Glass Model

Having established that the density of states configurations and the effective gap exponents are affected by sudden changes in the charge carrier densities in the Coulomb glass model, we aim to carry out the same investigation for the Bose glass model with logarithmic interactions. This study is of high importance because it analyzes the effects of abrupt changes in vortex line density on the spatial rearrangements of magnetic vortex lines in type-II superconductors, while the first part of this dissertation focused on the flux lines height fluctuations.

Similar to the study above, we start with the Bose glass model with a fixed filling fraction $K = 0.5$, and we obtain the density of states in fig. 10.5 (section 10.1.2 in chapter 10), where a Coulomb gap appears and the DOS is broad and totally suppressed at the chemical potential μ_{c2}, which implies that the system here is relaxed beyond microscopic time scales.

In the case of suddenly increasing the system's filling fraction from $K = 0.5$ to $K_{final} = 0.54$, one notices the same behavior in the density of states in the Bose glass model, where the

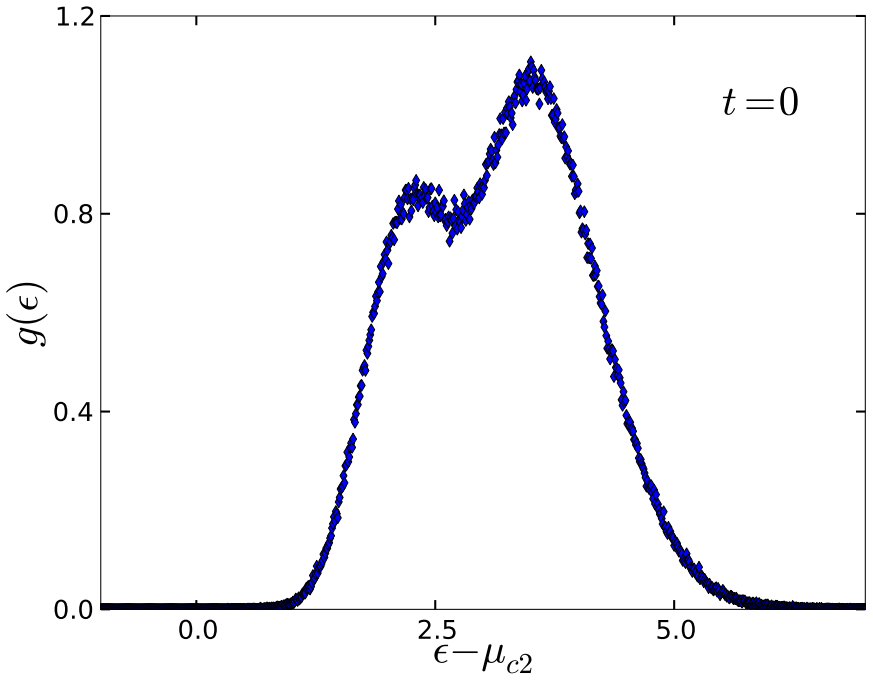

(a)

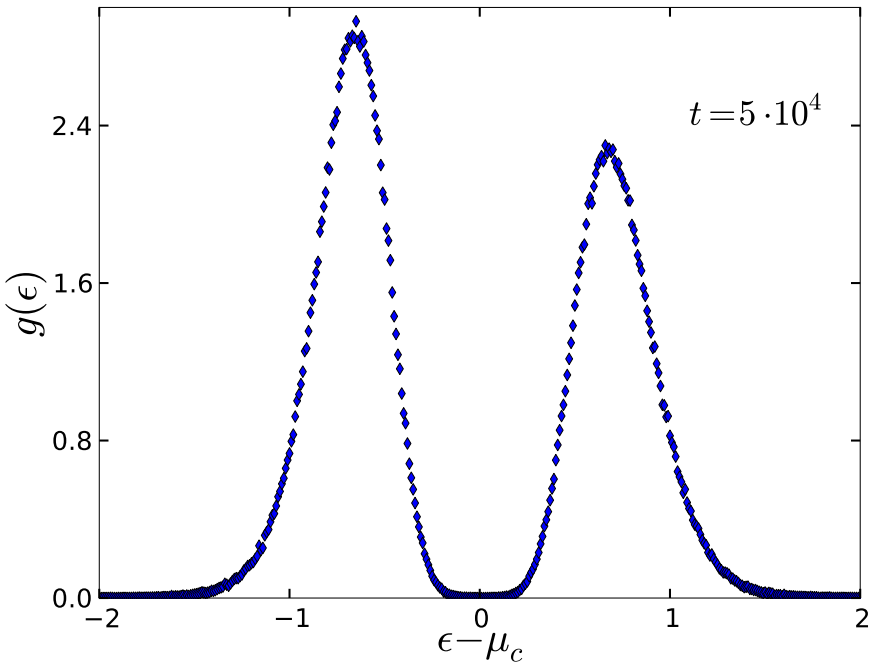

(b)

Figure 11.4: Density of states in the two-dimensional Bose glass model at (a) $t = 0$ and (b) $t = 5 \cdot 10^4$ MCS after suddenly increasing the filling fraction from $K = 0.5$ to $K_{final} = 0.54$. μ_{c2} is the the relaxed system's chemical potential before the quench, while μ_c is the chemical potential of the equilibrated system after the quench (data averaged over 6000 realizations).

system starts with an enhanced peak at the higher-energy states at $t = 0$, see fig. 11.4a. Hence, the symmetry that is witnessed with a fixed number of magnetic flux lines at half-filling is broken due to the initial introduction of new magnetic flux lines into the system with a constant number of pinning centers. As the system relaxes to $t = 5 \cdot 10^4$ MCS, the newly-added flux lines have explored the surrounding landscape and become pinned to the defect sites, and hence a peak on occupied sites is now enhanced as portrayed in fig. 11.4b.

When we considered the consequences of abruptly reducing the number of flux lines due to changing the filling fraction from $K = 0.5$ to $K_{final} = 0.46$, we observed the same reversed asymmetry that is witnessed in the down-quench case in the Coulomb glass system, which is discussed in section 11.1.1.

The last investigation we perform in this part is the effect of sudden changes in the number of flux lines on the effective gap exponent in the Bose glass model. The results are summarized in table 11.2.

	(a) No density quench	(b) Density up-quench	(c) Density down-quench
γ	4.4 ± 0.213	4.47 ± 0.232	4.42 ± 0.228

Table 11.2: Measured Coulomb gap exponent γ for the two-dimensional Bose glass model when the filling fraction is (a) kept fixed at $K = 0.5$, (b) suddenly raised from $K = 0.5$ to $K_{final} = 0.54$, and (c) abruptly lowered from $K = 0.5$ to $K_{final} = 0.46$ at $t = 5 \cdot 10^4$ MCS (data averaged over 6000 realizations).

The effective gap exponents for the different final filling fractions in table 11.2 are almost equal, which implies that this equilibrium property is similar in systems with the studied filling fractions $K = 0.5$, 0.54, and 0.46 in the Bose glass model.

11.2 Non-Equilibrium Relaxation Dynamics

In addition to studying the effects of charge carrier/flux line density quenches on the density of states and the soft Coulomb gap, we analyzed the effects of sudden addition/removal of carriers on the non-equilibrium relaxation properties and the aging scaling exponents: section 11.2.1 presents the results of this study in the Coulomb glass model and section 11.2.2 summarizes our findings for the Bose glass model, in the absence of random on-site energies.

11.2.1 Coulomb Glass Model

In the two-dimensional Coulomb glass model, we relax the system for a long time $r = 5 \cdot 10^4$ MCS to then quench the density of charge carriers and measure the resulting two-time charge autocorrelation function for different waiting times.

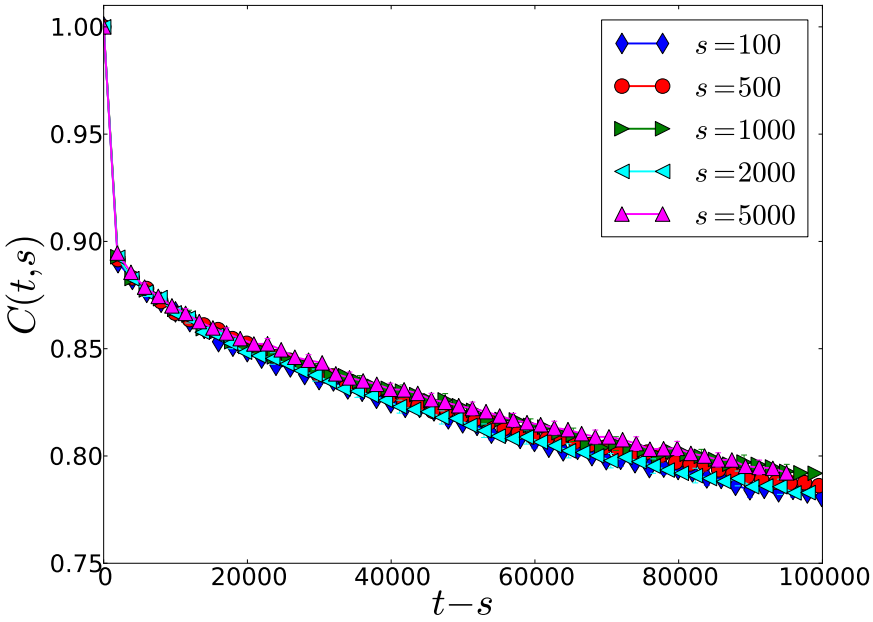

Figure 11.5: Relaxation of the two-time charge autocorrelation function in the two-dimensional Coulomb glass model with a fixed charge carrier density $K = 0.5$ (data averaged over 2000 realizations).

In the case where the density is kept fixed at $K = 0.5$, the dynamics in fig. 11.5 becomes less influenced by the choice of waiting times due to the long initial relaxation time that the system underwent. This is asserted by fig. 11.6 due to the approximate collapse of the various curves corresponding to different waiting times.

The charge autocorrelation function of this relaxed system with a fixed K does not acquire the dynamical scaling property, regardless of the choice of scaling exponents, possibly due

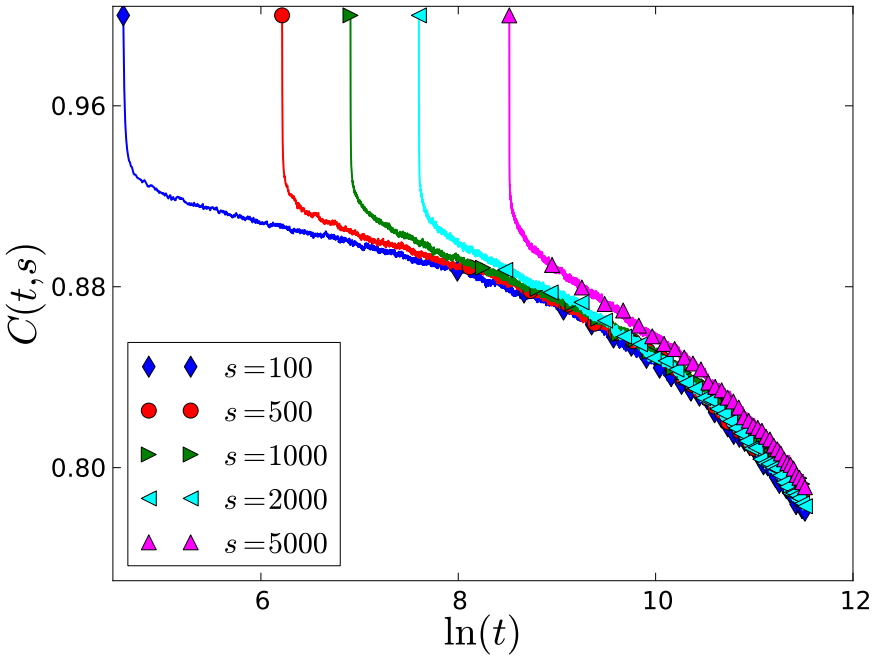

Figure 11.6: Relaxation of the two-time charge autocorrelation function in the two-dimensional Coulomb glass model with a fixed charge carrier density $K = 0.5$. The $\alpha - \beta$ relaxation displayed is a property of structural glasses (data averaged over 2000 realizations).

to the finite-size effects that emerge at the time scales considered. When the charge carrier density suddenly changes, we observe different features to the case with a fixed filling fraction K.

For both cases when (a) the charge carrier density abruptly increases from $K = 0.5$ to $K_{final} = 0.54$ and (b) the density abruptly decreases from $K = 0.5$ to $K_{final} = 0.46$, the dynamics is again highly dependent on the waiting times chosen as can be seen in fig. 11.7a and fig. 11.7b, respectively. Furthermore, it is evident that the cases of density up-quench and down-quench are similar in their relaxation dynamics.

Dynamical scaling is not present in the relaxed system with a fixed carrier density, while a similar system with random initial conditions displays dynamical scaling with the scaling exponents $b = 0.009$ and $\lambda_C/z = 0.09$. Investigating the dynamical scaling property after the influence of sudden changes in the density of charge carriers reveals that aging scaling is again a property of the system. Due to the similar relaxational dynamics in the cases of the density up-quench and down-quench above, we confirm that the dynamical aging scaling exponents b and λ_C/z are equal in both cases. This dynamical scaling behavior is displayed in fig. 11.9, where we compute $b = 0.013$ and $\lambda_C/z = 0.08$ for both cases.

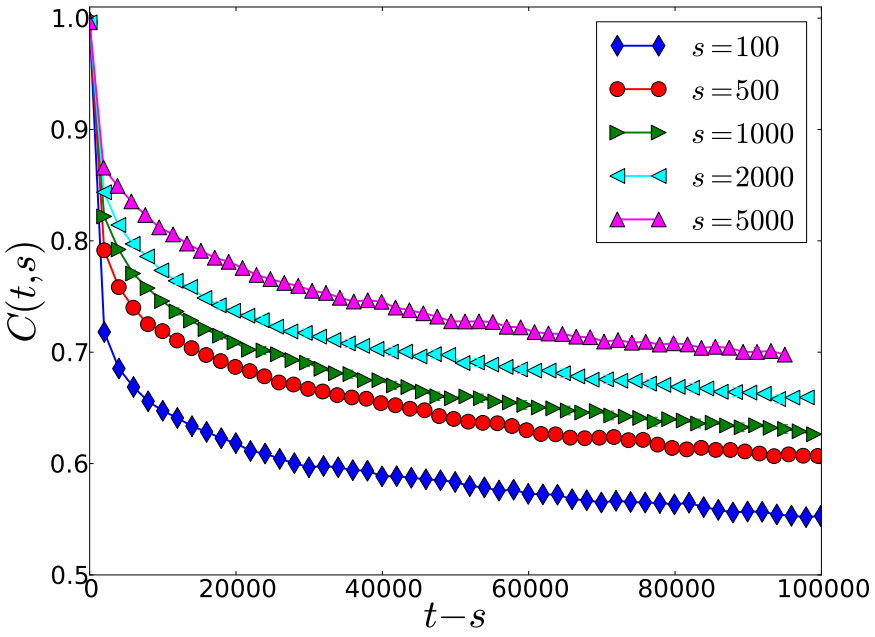

(a)

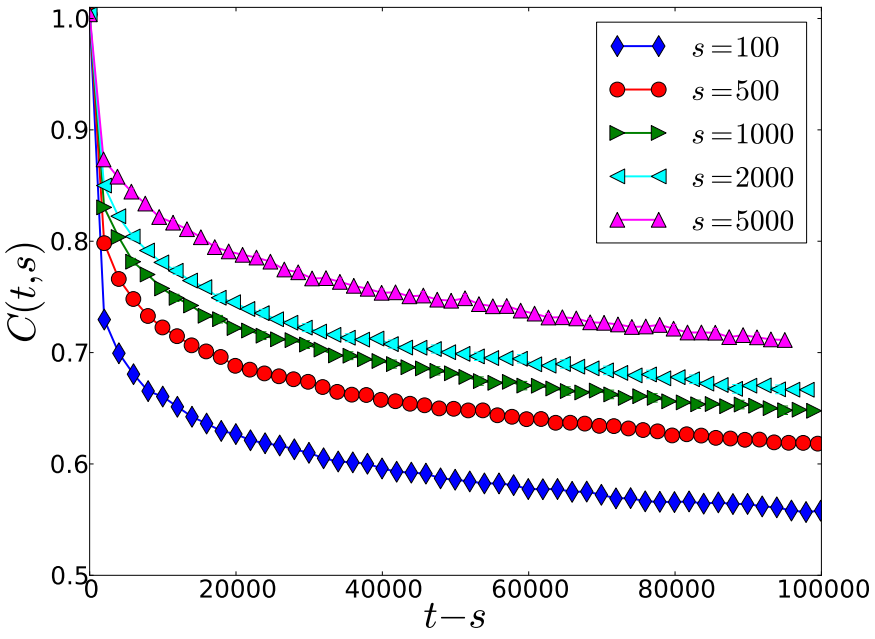

(b)

Figure 11.7: Relaxation of the two-time charge autocorrelation function in the two-dimensional Coulomb glass model after the filling fraction is suddenly (a) increased from $K = 0.5$ to $K_{final} = 0.54$ or (b) decreased from $K = 0.5$ to $K_{final} = 0.46$ (data averaged over 1000 realizations).

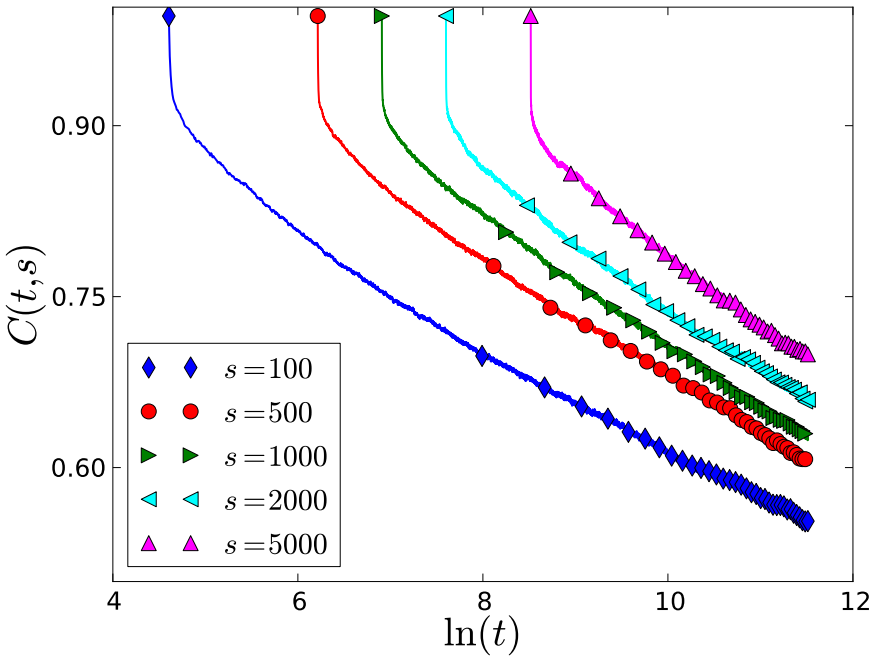

Figure 11.8: Relaxation of the two-time charge autocorrelation function in the two-dimensional Coulomb glass model after a sudden increase in the filling fraction from $K = 0.5$ to $K_{final} = 0.54$. The case when the filling fraction instantaneously decreases from $K = 0.5$ to $K_{final} = 0.46$ displays similar dynamics (data averaged over 1000 realizations).

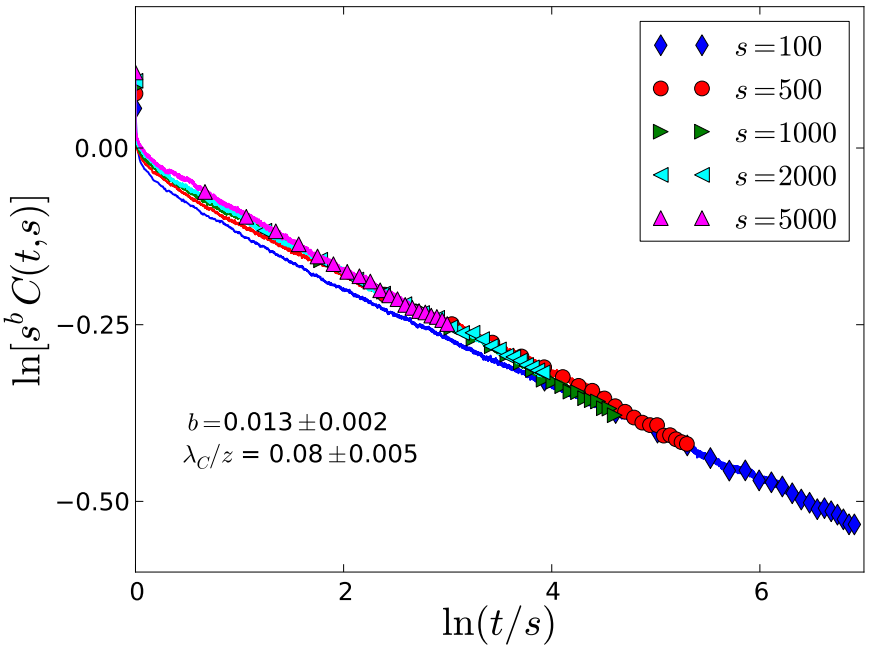

(a)

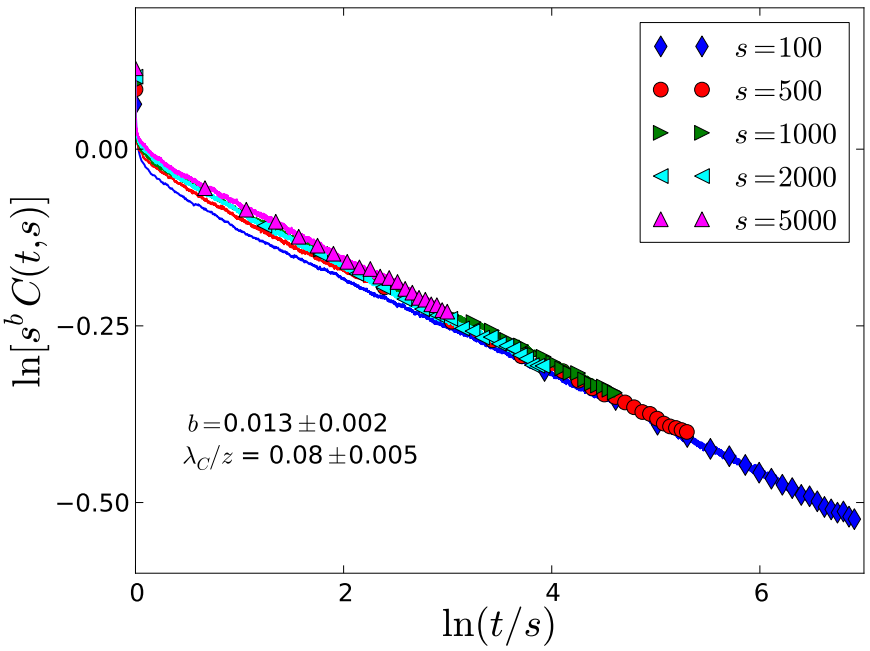

(b)

Figure 11.9: Relaxation of the two-time charge autocorrelation function in the two-dimensional Coulomb glass model after the filling fraction is suddenly (a) increased from $K = 0.5$ to $K_{final} = 0.54$ or (b) decreased from $K = 0.5$ to $K_{final} = 0.46$ (data averaged over 1000 realizations).

11.2.2 Bose Glass Model

The relaxational dynamics of the Bose glass model in two dimensions was also analyzed with a similar goal of studying the effects of sudden changes in the density of magnetic flux lines.

When the density of flux lines is kept fixed at $K = 0.5$ and the system is relaxed for a sufficiently long initial time $r = 5 \cdot 10^4$ MCS, the autocorrelation function displays behavior similar to that in fig. 11.5 whereas the relaxation has a weaker dependence on the waiting times, see fig. 11.10.

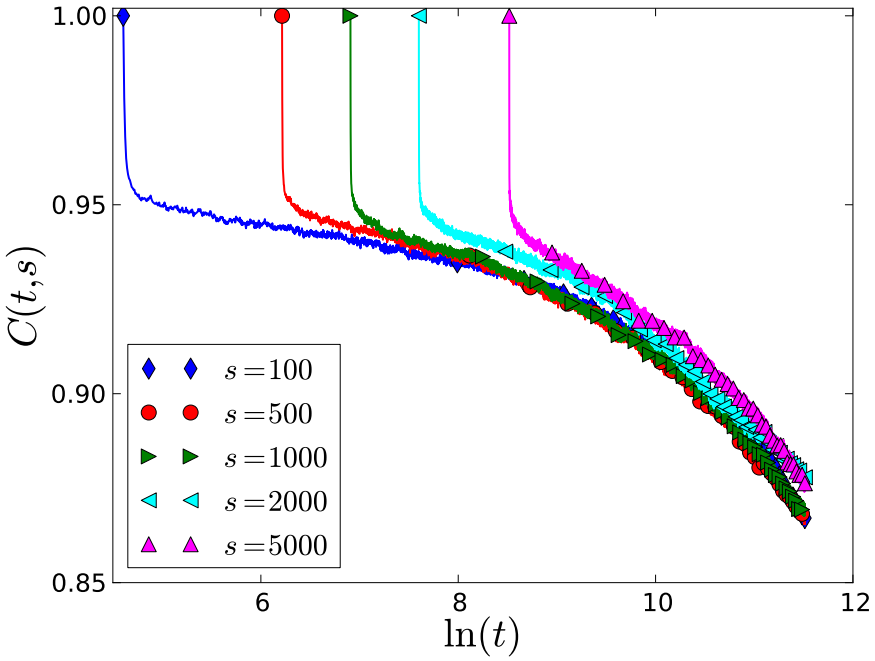

Figure 11.10: Relaxation of the two-time autocorrelation function in the two-dimensional Bose glass model with a fixed flux line density $K = 0.5$ (data averaged over 2000 realizations).

On the other hand, when the flux line density is suddenly increased from $K = 0.5$ to $K_{final} = 0.54$ or decreased from $K = 0.5$ to $K_{final} = 0.46$, we confirm that the system is again dependent on the waiting times s. Moreover, both systems similarly display an initial fast relaxation regime and a slower later regime, see fig. 11.11.

Dynamical scaling is not present in the relaxed system with a fixed flux line density, while a similar system with random initial conditions displays dynamical scaling with the scaling exponents $b = 0.001$ and $\lambda_C/z = 0.06$. In addition to the similarity displayed through the glassy dynamics in situations with abrupt increases or decreases in the magnetic flux line density, the scaling exponents are equal in both cases: $b = 0.007$ and $\lambda_C/z = 0.06$, see fig. 11.12.

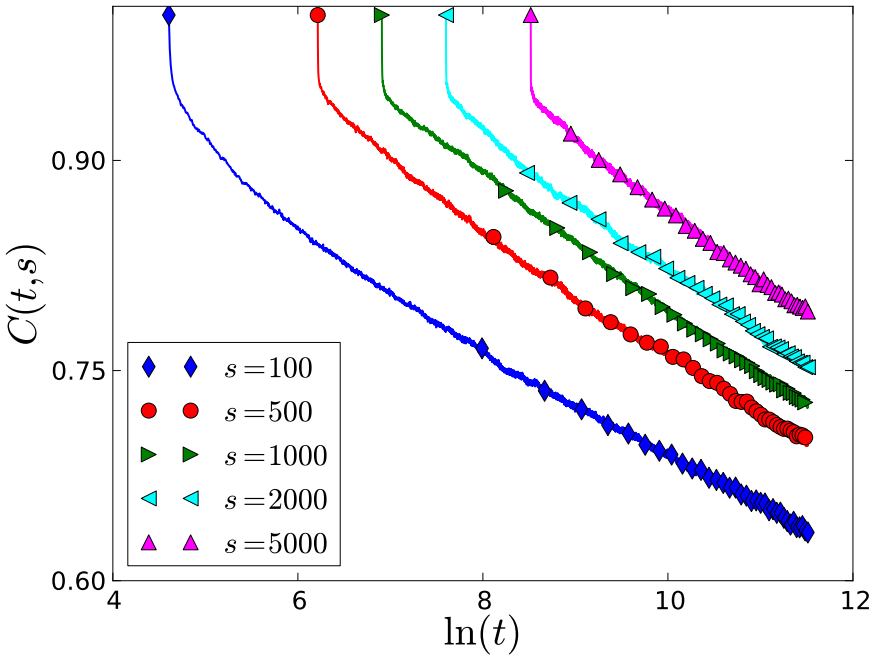

Figure 11.11: Relaxation of the two-time autocorrelation function in the two-dimensional Bose glass model after a sudden decrease in the filling fraction from $K = 0.5$ to $K_{final} = 0.46$. The case when the filling fraction instantaneously increases from $K = 0.5$ to $K_{final} = 0.54$ displays similar dynamics (data averaged over 1000 realizations).

The equal aging scaling exponents b and λ_C/z in the Bose glass systems when the magnetic flux line density is abruptly increased or decreased implies that this system undergoes similar relaxational dynamics when new flux lines are added to the sample or after some flux lines are removed from the sample due to particle-hole symmetry. This observation was also made in the Coulomb glass model with sudden changes in the charge carrier density.

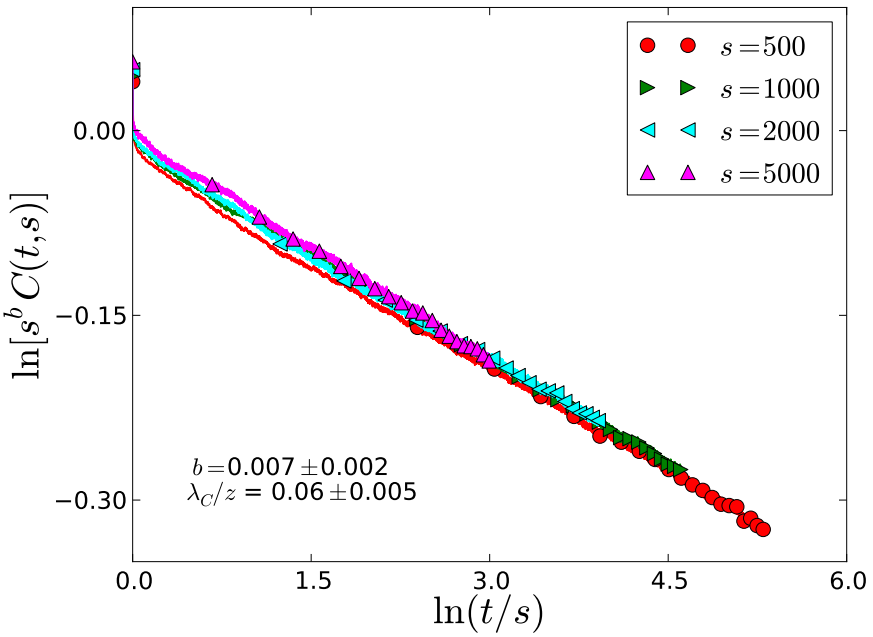

(a)

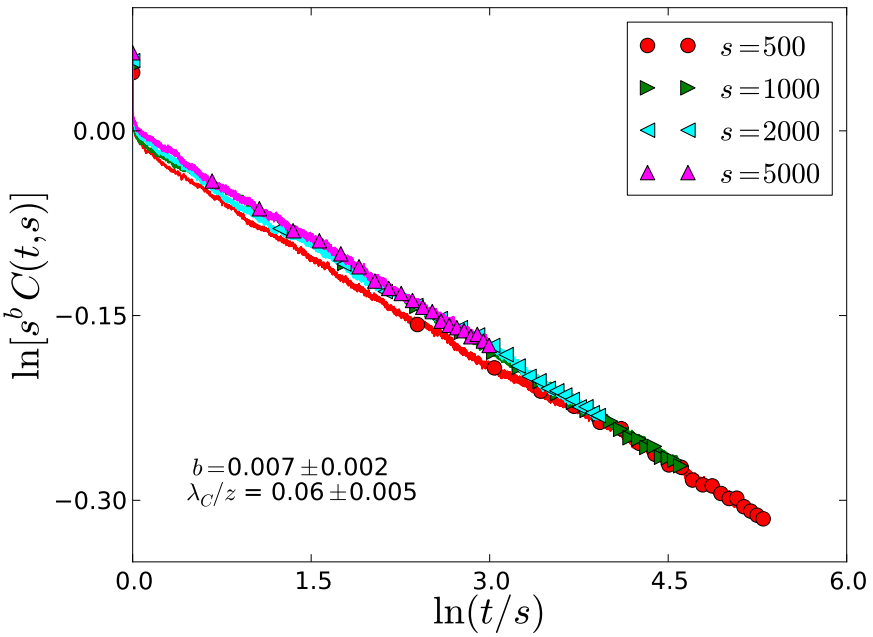

(b)

Figure 11.12: Relaxation of the two-time autocorrelation function in the two-dimensional Bose glass model after the filling fraction is suddenly (a) increased from $K = 0.5$ to $K_{final} = 0.54$ or (b) decreased from $K = 0.5$ to $K_{final} = 0.46$ (data averaged over 1000 realizations).

Chapter 12

Conclusions

We employed the Coulomb glass model in disordered semiconductors and adapted it to the Bose glass model in type-II superconductors in the presence of extended linear defects to investigate the density of states and the non-equilibrium relaxation properties in the two-dimensional Coulomb and Bose glass systems via Monte Carlo simulations.

Earlier investigations focused on these systems with zero on-site energies, thus one goal of this study is to analyze the effects of adding random on-site energies from different distributions into the Coulomb and Bose glass systems with a fixed charge carrier/flux line density. We concluded that adding on-site energies from a Gaussian distribution of zero mean and of various widths does not noticeably affect the speed of formation of the Coulomb gap or the effective gap exponent in both models. On the other hand, a flat distribution of a similar width to the one utilized for the Gaussian distribution causes the suppression of the density of states at the chemical potential to become slower in the Coulomb glass model, while not affecting this feature in the Bose glass model. In addition to this, adding random on-site energies from this flat distribution causes the gap exponent's effective value to become closer to the mean-field predictions in both models. Broad on-site energy distributions of widths on the same scale as the correlation-induced Coulomb gap's width affect the density of states around the chemical potential in these two models.

The non-equilibrium relaxation dynamics shows the effects of non-zero random on-site energies as well: The Gaussian distribution on-site energies do not change the aging scaling exponents, while the flat distribution energies have a pronounced effect on these exponents in both systems. Including random on-site energies from a flat distribution into the Coulomb and Bose glass models causes their relaxation to become slower. This change in the aging scaling exponents implies that these exponents are not universal and depend on the system parameters.

Another goal of this study is to analyze the effects of abrupt changes in the density of charge carriers in the Coulomb glass model or magnetic flux lines in the Bose glass model to gauge

the systems' response to sudden perturbations and thus bridge our results with experimental setups. In the cases of density up-quench and down-quench in both models: the system first responds to the quench by showing an asymmetry in the density of states around the chemical potential of the equilibrated system before the quench since the filling fraction is not half anymore. When the new system reaches equilibrium, the larger peak shifts to the opposite side of the system's newly assumed chemical potential due to the initiated relaxation of the newly-added carriers or the system after the effect of removing some carriers. It is also worth noting that since the Coulomb gap exponent is an equilibrium property, one obtains the same exponent in a system with a specific filling fraction regardless of the utilized initial conditions.

Similar to the investigation we performed in the first part of this dissertation, we analyzed the effects of density quenches on the non-equilibrium relaxation dynamics and the aging properties in the Coulomb and Bose glass models. The system with a fixed density relaxes for a long time until time translation invariance is displayed by the charge autocorrelation function. Dynamical scaling is not a property of the Coulomb and Bose glass models when the density is fixed. On the other hand, when the density is suddenly raised or lowered, the system displays dynamical scaling and the aging scaling exponents are equal in the cases of density up-quench and down-quench in both models. The equal aging scaling exponents when the density of charge carriers or flux lines abruptly changes confirms that the corresponding systems undergo similar relaxational dynamics as a response to the added carriers or the system after the removal of some carriers due to particle-hole symmetry. The different aging scaling exponents in the Coulomb and Bose glass models with random initial conditions and after sudden changes in the carrier density assert that these exponents depend on the system's initial conditions, unlike the Coulomb gap exponent.

In future work, we plan to extend our study to further analyze the effects of various random on-site energy distributions on the Coulomb gap properties and the aging scaling forms. We furthermore plan to investigate the effects of sudden changes in the charge carrier/flux lines density in the presence of non-zero on-site energies on the density of states and the non-equilibrium relaxation dynamics, including identifying the characteristic length scales and their relaxation in time in both systems.

Bibliography

[1] H. K. Onnes. *Leiden Comm.* **120b, 122b, 124c** (1911) (Cited on page 4.)

[2] W. Meissner and R. Ochsenfeld. *Naturwissenschaften* **21** 787 (1933) (Cited on page 4.)

[3] M. Tinkham. *Introduction to superconductivity.* New York, NY, Mcgraw-Hill Publishing Co (1996) (Cited on pages 4 and 17.)

[4] J. N. Rjabinin, L. W. Schubnikow. *Physikalische Zeitschrift der Sowjetunion* **7** 1 (1935) (Cited on page 4.)

[5] J. N. Rjabinin, L. W. Schubnikow. *Nature* **135** 3415 (1935) (Cited on page 4.)

[6] G. Blatter, V. B. Geshkenbein, A. I. Larkin, and V. M. Vinokur. *Reviews of Modern Physics* **66** 1125 (1994) (Cited on page 6.)

[7] W. K. Kwok, J. Fendrich, S. Fleshler, U. Welp, J. Downey, G. W. Crabtree, and J. Giapintzakis. *Physica B* **197** 579 (1994) (Cited on page 6.)

[8] P. Yang, C. M. Lieber. *Science* **273** 1836 (1996) (Cited on page 6.)

[9] M. P. A. Fisher. *Physical Review Letters* **62** 1415 (1989) (Cited on pages 6 and 20.)

[10] M. V. Feigel'man, V. B. Geshkenbein, A. I. Larkin, and V. M. Vinokur. *Physical Review Letters* **63** 2303 (1989) (Cited on pages 6 and 20.)

[11] T. Nattermann. *Physical Review Letters* **64** 2454 (1990) (Cited on pages 6 and 20.)

[12] D. S. Fisher, M. P. A. Fisher, and D. A. Huse. *Physical Review B* **43** 130 (1991) (Cited on pages 6 and 20.)

[13] W. K. Kwok, S. Fleshler, U. Welp, V. M. Vinokur, J. Downey, G. W. Crabtree, and M. M. Miller. *Physical Review Letters* **69** 3370 (1992) (Cited on pages 6, 20, 21, and 59.)

[14] T. Giamarchi and P. Le Doussal. *Physical Review Letters* **72** 1530 (1994) (Cited on pages 6 and 20.)

[15] T. Giamarchi and P. Le Doussal. *Physical Review B* **52** 1242 (1995) (Cited on pages 6 and 20.)

[16] J. Kierfeld, T. Nattermann, and T. Hwa. *Physical Review B* **55** 626 (1997) (Cited on pages 6 and 20.)

[17] D.S. Fisher. *Physical Review Letters* **78** 1964 (1997) (Cited on pages 6 and 20.)

[18] T. Giamarchi and P. Le Doussal. *Physical Review B* **55** 6577 (1997) (Cited on pages 6 and 20.)

[19] For a review, see: T. Nattermann and S. Scheidl. *Advances in Physics* **49** 607 (2000) (Cited on pages 6 and 20.)

[20] D. R. Nelson and V. M. Vinokur. *Physical Review Letters* **68** 2398 (1992) (Cited on pages 6, 21, 59, and 65.)

[21] I. F. Lyuksyutov. *Europhysics Letters* **200** 273 (1992) (Cited on pages 6, 21, 59, and 65.)

[22] M. P. A. Fisher, P. B. Weichman, G. Grinstein, and D. S. Fisher. *Physical Review B* **40** 546 (1989) (Cited on pages 6, 21, and 59.)

[23] D. R. Nelson and V. M. Vinokur. *Physical Review B* **48** 13060 (1993) (Cited on pages 6, 21, 24, 59, and 65.)

[24] L. Civale, A. D. Marwick, T. K. Worthington, M. A. Kirk, J. R. Thompson, L. Krusin-Elbaum, Y. Sun, J. R. Clem, and F. Holtzberg. *Physical Review Letters* **67** 648 (1991) (Cited on pages 6, 21, and 59.)

[25] D. Vasyukov, Y. Anahory, L. Embon, D. Halbertal, J. Cuppens, L. Neeman, A. Finkler, Y. Segev, Y. Myasoedov, M. L. Rappaport, M. E. Huber, and E. Zeldov. *Nature Nanotechnology* **8** 639 (2013) (Cited on page 7.)

[26] O. M. Auslaender, L. Luan, E. W. J. Straver, J. E. Hoffman, N. C. Koshnick, E. Zeldov, D. A. Bonn, R. Liang, W. N. Hardy, and K. A. Moler. *Nature Physics* **5** 35 (2009) (Cited on page 7.)

[27] Y. Abulafia, A. Shaulov, Y. Wolfus, R. Prozorov, L. Burlachkov, D. Majer, E. Zeldov, V. M. Vinokur, and Y. Yeshurun. *Journal of Low Temperature Physics* **107** 455 (1997) (Cited on page 7.)

[28] M. R. Eskildsen, E. M. Forgan, and H. Kawano-Furukawa. *Reports on Progress in Physics* **74** 124504 (2011) (Cited on page 7.)

[29] L. C. E. Struik. *Physical Aging in Amorphous Polymers and Other Materials*. Amsterdam, Elsevier (1978) (Cited on pages 7 and 21.)

[30] M. Henkel, M. Pleimling, and E. Sanctuary, eds. *Ageing and the Glass Transition*. Vol. 716. Lecture Notes in Physics. Berlin, Springer (2007) (Cited on page 7.)

[31] M. Henkel and M. Pleimling. *Non-Equilibrium Phase Transitions, Vol. 2: Ageing and Dynamical Scaling Far from Equilibrium*. Berlin, Springer (2010) (Cited on pages 7, 21, 22, and 37.)

[32] X. Du, G. Li, E. Y. Andrei, M. Greenblatt, and P. Shuk. *Nature Physics* **3** 111 (2007) (Cited on pages 7 and 59.)

[33] E. L. Papadopoulou, P. Nordblad, P. Svedlindh, R. Schöneberger, and R. Gross. *Physical Review Letters* **82** 173 (1999) (Cited on page 8.)

[34] S. Bustingorry, L. F. Cugliandolo, and D. Domínguez. *Physical Review Letters* **96** 027001 (2006) (Cited on page 8.)

[35] S. Bustingorry, L. F. Cugliandolo, and D. Domínguez. *Physical Review B* **75** 024506 (2007) (Cited on page 8.)

[36] M. Pleimling and U. C. Täuber. *Physical Review B* **84** 174509 (2011) (Cited on pages 8, 27, 29, 38, 47, and 54.)

[37] U. Dobramysl, H. Assi, M. Pleimling, U. C. Täuber. *The European Physical Journal B* **86** 228 - 1-15 (2013) (Cited on pages 8, 27, 29, 38, 40, 54, and 55.)

[38] J. Bardeen, L. N. Cooper, and J. R. Schrieffer. "Microscopic Theory of Superconductivity". *Physical Review* **106** 162-164 (1957) (Cited on page 10.)

[39] J. Bardeen, L. N. Cooper, and J. R. Schrieffer. "Theory of Superconductivity". *Physical Review* **108** 1175-1204 (1957) (Cited on page 10.)

[40] L. P. Gor'kov. "Microscopic derivation of the Ginzburg-Landau Equations in the Theory of Superconductivity". *Soviet Physics JETP* **9** 1364 (1959) (Cited on page 10.)

[41] V. L. Ginzburg and L. D. Landau. "On Superconductivity Theory". *Zhurnal Eksperimental'noi i Teoreticheskoi* **20** 1064 (1950) (Cited on page 10.)

[42] L. D. Landau. *Zhurnal Eksperimental'noi i Teoreticheskoi Fiziki* **7** 19-32 (1937) (Cited on page 10.)

[43] F. Landau. *Superfluids* Vol. I. Wiley, New York (1950) (Cited on page 16.)

[44] A. A. Abrikosov. "On the Magnetic Properties of Superconductors of the Second Group". *Soviet Physics JETP* **5** (1957) (Cited on page 16.)

[45] W. H. Kleiner, L. M. Roth, and S. H. Autler. *Physical Review* **133** A1226 (1957) (Cited on page 17.)

[46] U. Essmann and H. Träuble. *Physical Letters* **24A** 526 (1967) (Cited on page 17.)

[47] A. Seeger. *Comments Solid State Physics* **3** 97 (1970) (Cited on page 17.)

[48] U. Essmann. *Physical Letters* **41A** 477 (1972) (Cited on page 17.)

[49] G. Blatter and V. B. Geshkenbein. "Vortex Matter". *The Physics of Superconductors, Vol. 1: Conventional and High-T_C Superconductors*. Ed. by K. H. Bennemann and J. B. Ketterson. Berlin, Springer (2003) (Cited on page 20.)

[50] A. I. Larkin and Y. V. Ovchinnikov. *Journal of Low-Temperature Physics* **34** 409 (1979) (Cited on page 20.)

[51] D. R. Nelson. *Physical Review Letters* **60** 1973 (1988) (Cited on pages 20 and 21.)

[52] E. H. Brandt. *Physical Review Letters* **63** 1106 (1989) (Cited on page 20.)

[53] D. R. Nelson and H. S. Seung. *Physical Review B* **39** 9153 (1989) (Cited on page 21.)

[54] D. R. Nelson. *Journal of Statistical Physics* **57** 511 (1989) (Cited on page 21.)

[55] U. C. Täuber and D. R. Nelson. *Physical Reports* **289** 157 (1997); e: **296** 337 (1998) (Cited on page 21.)

[56] J. Das, T. J. Bullard, and U. C. Täuber. *Physica A* **318** 48 (2003) (Cited on pages 24 and 25.)

[57] T. J. Bullard, J. Das, G. L. Daquila, and U. C. Täuber. *European Physical Journal B* **65** 469 (2008) (Cited on page 25.)

[58] A. Brass and H. J. Jensen. *Physical Review B* **39** 9587 (1989) (Cited on page 26.)

[59] J. Bardeen and M. Stephen. *Physical Review* **140** A1197-A1207 (1965) (Cited on page 26.)

[60] M. M. Abdelhadi and K. A. Ziq. *Superconductor Science and Technology* **7** 99 (1994) (Cited on page 27.)

[61] H. Assi, H. Chaturvedi, U. Dobramysl, M. Pleimling, U. C. Täuber, *to appear in Molecular Simulation* (2015) [arXiv:1509.02227] (Cited on pages 31, 48, and 56.)

[62] A. Röthlein, F. Baumann, and M. Pleimling. *Physical Review E* **74** 061604 (2006) (Cited on pages 37 and 38.)

[63] W. Götze and L. Sjogren. *Reports on Progress in Physics* **55** 241 (1992) (Cited on page 47.)

[64] H. Assi, H. Chaturvedi, U. Dobramysl, M. Pleimling, U. C. Täuber. *Physical Review E* 92, 052124 (2015) (Cited on page 54.)

[65] A. L. Efros and B. I. Shklovskii. *Journal of Physics C: Solid State Physics* **8**(4) L49 (1975) (Cited on pages 58, 59, 61, 64, 67, and 75.)

[66] B. I. Shklovskii and A. L. Efros. *Electronic Properties of Doped Semiconductors*, Springer, New York (1984) (Cited on pages 58, 61, 62, 63, 64, and 75.)

[67] A. L. Efros and M. Pollak. *Electron-Electron Interactions in Disordered Systems*, North Holland, Amsterdam (1985) (Cited on pages 58, 61, 64, and 75.)

[68] J. H. Davies, P. A. Lee, and T. M. Rice. *Physical Review Letters* **49** 758 (1982) (Cited on pages 59, 62, 64, 65, and 75.)

[69] A. Möbius, M. Richter, and B. Drittler. *Physical Review B* **45**(20) 11568 (1992) (Cited on pages 59, 64, and 75.)

[70] J. Jaroszynski and D. Popović. *Physical Review Letters* **99**(4) 046405 Jul. (2007) (Cited on page 59.)

[71] J. Jaroszynski and D. Popović. *Physical Review Letters* **99**(21) 216401 Nov. (2007) (Cited on page 59.)

[72] D. R. Grempel. *Europhysics Letters* **66**(6) 854 (2004) (Cited on pages 59 and 70.)

[73] U. C. Täuber and D. R. Nelson. *Physical Review B* **52** 16106 (1995) (Cited on pages 59, 60, 64, 65, and 67.)

[74] U. C. Täuber, H. Dai, D. R. Nelson, and C. M. Lieber. *Physical Review Letters* **74** 5132 (1995) (Cited on pages 59, 60, and 65.)

[75] M. T. Shimer, U. C. Täuber, and M. Pleimling. *Europhysics Letters* **91** 67005 (2010) (Cited on pages 60, 70, 74, and 89.)

[76] M. T. Shimer, U. C. Täuber, and M. Pleimling. *Physical Review E* **90** 032111 (2014) (Cited on pages 60, 70, 74, and 89.)

[77] M. Grünewald, B. Pohlmann, L. Schweitzer, and D. Würtz. *Journal of Physics C: Solid State Physics* **15**(32) L1153 (1982) (Cited on pages 64 and 75.)

[78] W. Xue and P. A. Lee. *Physical Review B 38*(13) 9093 (1988) (Cited on pages 64 and 75.)

[79] E. R. Grannan and C. C. Yu. *Physical Review Letters* **71**(20) 3335 (1993) (Cited on pages 64 and 75.)

[80] D. Menashe, O. Biham, B. D. Laikhtman, and A. L. Efros. *Europhysics Letters* **52**(1) 94 (2000) (Cited on pages 64 and 75.)

[81] D. Menashe, O. Biham, B. D. Laikhtman, and A. L. Efros. *Physical Review B* **64**(11) 115209 (2001) (Cited on pages 64 and 75.)

[82] B. Surer, H. G. Katzgraber, G. T. Zimanyi, B. A. Allgood, and G. Blatter. *Physical Review Letters 102*(6) 067205 (2009) (Cited on pages 64 and 75.)

[83] A. L. Efros, B. Skinner, and B. I. Shklovskii. *Physical Review B* **84** 064204 (2011) (Cited on page 65.)

[84] A. B. Kolton, D. R. Grempel, and D. Domínguez. *Physical Review B* **71**(2) 024206 (2005) (Cited on page 70.)